POLITECNICO DI MILANO

Scuola di Ingegneria dell'Informazione

Corso di Laurea Magistrale in Ingegneria Fisica

Electrochemical layer by layer growth of chalcogenide thin films on Ag(111)

Relatore: Prof. Giacomo Claudio GHIRINGHELLI
Correlatore: Dott. Francesco CARLÀ

Tesi di Laurea di:
Fabio ZAMPIERI
Matricola: 802429

Anno Accademico 2013-2014

“L’uomo deve perseverare nell’idea che
l’incomprensibile sia comprensibile;
altrimenti rinuncerebbe a cercare.”

J. W. Goethe

Ai miei genitori

Acknowledgments

I firstly want to thank my university supervisor, Prof. Giacomo Ghiringhelli, that gave me the opportunity to work at ESRF and to live a very important experience for both my personal and my working life. A heartfelt thanks then goes to my ESRF supervisor, Francesco Carlà, that followed me during these six months, supporting me during experiments and the drafting of this thesis, teaching me all the methods and the procedures and helping me for every problem and doubt. I also am grateful to Roberto Felici and Helena Isern for their willingness and to help me whenever they had the possibility. I then thank all the ID03 beamline people that made very pleasant my experience at ESRF.

I really express my deepest gratitude to my mother Daniela and my father Michele that since I started the university have made huge sacrifices to allow me to study, always supporting me as they have done for my entire life, making me the person I have become. I also want to thank my grandparents Gianna, Luciano, Ada and Adriano whose teachings and wisdom has been and still are very important and Cristina and Gregorio for being there for me.

A special thanks goes to Giulia who shared with me all the good and bad moments, all my successes and all my failures, always supporting me with her words, her presence and with her love.

I want then to thank all my friends: Thomas who knows me since I can remember and whom I can always count on; Lorenzo whose friendship is very important and who shared with me the very first years of university life; Stefano and Lorenzo whose friendship, born during the bachelor degree, made pleasant these university years and will last despite the different ways we have chosen; Silvio and Stefano whose fellowship help me during my new adventure in Milan; Andrea and Lorenzo who shared with me the entire adventure in Grenoble and Stefano who daily shared with me this working experience and in whom I have found very good friends.

Contents

Acknowledgments **i**

Abstract **v**

Estratto in italiano **vi**

List of Figures **vii**

1 Introduction **1**

1.1 Chalcogenide multilayers as anodes for lithium-ion batteries 1

1.2 Electrodeposition 2

1.2.1 Electrochemical cell 2

1.2.2 Electrodeposition methods 4

1.2.3 Under Potential Deposition 5

1.2.4 ECALE electrodeposition 7

2 Experimental **9**

2.1 Ag(111) Substrates 9

2.1.1 Surface Chemical Preparation 9

2.1.2 UHV preparation 10

2.1.3 Electrochemical preparation 10

2.2 Cyclic voltammetry 11

2.3 Electrodeposition apparatus 13

2.4 Chemicals 16

2.5 Structural characterization 17

2.5.1 Diffraction 17

2.5.1.1 Crystal structure 17

2.5.1.2 X-Ray Diffraction 18

2.5.1.3 Surface X-Ray Diffraction 21
2.5.2 Reflectivity measurements 22
2.5.3 Beamline Instrumentation 24

3 Results **27**
3.1 Electrodeposition of chalcogenides on Ag(111) 27
3.1.1 Antimony electrodeposition 30
3.1.2 Zinc electrodeposition 30
3.1.3 Multilayer deposition 31
3.2 Deposition of Sb_2S_3 32
3.2.1 Ammonia buffer 32
3.2.2 NaOH 36
3.2.3 Acetic buffer 39
3.2.3.1 Multilayer 50
3.3 Deposition of other antimony chalcogenides 52
3.3.1 Deposition of Sb_2Te_3 52
3.3.2 Deposition of Sb_2Se_3 52
3.4 Deposition of $ZnSe$ 55
3.4.1 Electrochemical characterization 55
3.4.2 Reflectivity experiments 59
3.4.3 In-plane structure 61
3.4.4 Microscopy Imaging 67

4 Conclusions **72**

Bibliography **75**

Abstract

This thesis project was conducted at the European Synchrotron Radiation Facility (ESRF) in Grenoble, in Surface Diffraction Beamline ID03.

The aim of the project was the deposition and the characterization of chalcogenide thin films on the surface (111) of a silver single crystal substrate. Chalcogenides are promising candidates for the fabrication of anodes for lithium-ion batteries. In fact chalcogenide based anodes show improved performances, both increasing the lifetime and the capacity of the batteries.

In the experimental it is described the instrumentation used in the experimental work (the electrochemical system and the x-rays diffractometer) and an introduction to the methods used for the synthesis and the characterization of the samples (electrochemical atomic layer epitaxy, Bragg diffraction and reflectivity measurements).

A brief overview on the state of the art of the deposition of antimony and zinc chalcogenides is reported as introduction to the result section. In this section methods and deposition parameters of each chalcogenide (Sb_2S_3, Sb_2Te_3, Sb_2Se_3 and $ZnSe$) are described as well as the outcomes of the electrochemical characterization. The results of an extensive structural investigation conducted on $ZnSe$ thin films are also reported.

Estratto in italiano

Questo progetto di tesi è stato svolto presso i laboratori dell'European Synchrotron Radiation Facility (ESRF) di Grenoble, nello specifico presso la beamline ID03, specializzata in diffrazione da superfici.

Lo scopo del progetto era la deposizione e la caratterizzazione di film sottili di calcogenuri depositati sulla superficie (111) di argento monocristallino. I calcogenuri sembrano essere ottimi candidati per la fabbricazione di anodi per batterie al litio. Anodi preparati con questi materiali infatti presentano migliori prestazioni in termini di vita e capacità delle batterie, limitando la cause di irreversibilità durante la reazione di litiazione/delitiazione.

Nella sezione sperimentale viene descritta la strumentazione utilizzata per la deposizione dei film (elettrodi, cella elettrochimica e sistema di interscambio delle soluzioni), quella necessaria alla preparazione del substrato e il diffrattometro per raggi x utilizzato per la caratterizzazione del campione. Sono state infine illustrate le tecniche mediante le quali sono stati condotti gli esperimenti: deposizione elettrochimica e specificamente electrochemical atomic layer epitaxy (ECALE), diffrazione di Bragg e misure di riflettività del campione.

La sezione dei risultati viene introdotta da una panoramica sullo stato dell'arte della deposizione di calcogenuri di antimonio e zinco. In questa sezione vengono descritti i metodi e i parametri di deposizione per ogni calcogenuro studiato (Sb_2S_3, Sb_2Te_3, Sb_2Se_3 e $ZnSe$) ed i risultati della caratterizzazione elettrochimica. Vengono inoltre descritti i risultati di una analisi più approfondita su campioni di $ZnSe$ atta a indagare la struttura nel piano e fuori dal piano del film mediante esperimenti di riflettività e di diffrazione di Bragg.

List of Figures

1.1 Electrolytic cell. 3

2.1 Cyclic voltammetry of Ag(111) in ammonia buffer. Scan rate: 50 mV s^{-1}. 11
2.2 Diagram of a three-electrode cell. 1 is the working electrode, 2 is the counter electrode, 3 is the reference electrode. 12
2.3 Cyclic voltammetry example. 13
2.4 Flow cell. 14
2.5 Electrochemistry rack. 16
2.6 Von Laue formulation. 19
2.7 Ewald sphere. 20
2.8 Ewald sphere for surface diffraction. 21
2.9 Ewald sphere for thin film diffraction. 22
2.10 Figure 1 of Schreiber's review[8] on reflectivity: specular reflectivity of x-rays on a thin film surface. 23
2.11 Experimental hutch 1. 25
2.12 Diffractometer and hexapode scheme in experimental hutch 1. 26

3.1 Sulfur oxidative underpotential deposition reported by Aloisi[11]. The curve b is a cyclic voltammetry of Ag(111) with 1 mM Na_2S in 0.1 M NaOH. 28
3.2 Figure 2 in Pezzatini's paper[23] on selenium reductive stripping. The curves a, b, c are consecutive cyclic voltammetries of Ag(111) with 0.5 mM Na_2SeO_3 in ammonia buffer. 29
3.3 Cyclic voltammetry of Ag(111) in 0.5 mM Na_2S buffered with ammonia buffer. Scan rate: 50 mV s^{-1}. 33

3.4 Cyclic voltammetry of Ag(111) in 0.5 mM Na_2S buffered with ammonia buffer. Scan rate: 50 mV s^{-1}. 33

3.5 Cyclic voltammetry of Ag(111) in 0.05 mM Sb_2O_3 buffered with ammonia buffer. Scan rate: 50 mV s^{-1}. 34

3.6 Stripping voltammetries of S/Ag(111) in 0.05 mM Sb_2O_3 buffered with ammonia buffer. They were obtained depositing Sb on S/Ag(111) at -0.65, -0.63 and -0.58 V and then scanning the potential. For each test two voltammetries were performed using different deposition times (60 and 120 seconds). For the -0.65 V deposition potential, both voltammetries were performed again after depositing Sb in a fresh solution. Scan rate: 50 mV s^{-1}. 35

3.7 Stripping voltammetries of Sb/Ag(111) in NaOH solution after the deposition of Sb at -0.95 V for different periods of time. Scan rate: 50 mV s^{-1}. 37

3.8 Cyclic voltammetries of Ag(111) in 0.5 mM Na_2S buffered with ammonia buffer (green) and in NaOH solution (red). Scan rate: 50 mV s^{-1}. 37

3.9 Stripping voltammetries of Sb/S/Ag(111) in NaOH solution after the deposition of Sb at -0.82 V for different periods of time. Scan rate: 50 mV s^{-1}. 38

3.10 Cyclic voltammetries of Ag(111) in 0.5 mM $K_2Sb_2(C_4H_2O_6)_2$ buffered with acetic buffer. Used potential were -0.6, -0.65, -0.7 and -0.75 V. Scan rate: 50 mV s^{-1}. 40

3.11 Stripping voltammetries of Sb/Ag(111) in acetic buffer. They were obtained depositing Sb from 0.5 mM $K_2Sb_2(C_4H_2O_6)_2$ solution on Ag(111) at -0.4 V for 30, 60, 120 and 240 seconds and then scanning the potential. Scan rate: 50 mV s^{-1}. 41

3.12 Stripping voltammetries of Sb/Ag(111) in acetic buffer. They were obtained depositing Sb from 0.5 mM $K_2Sb_2(C_4H_2O_6)_2$ solution on Ag(111) at -0.4 V for 60 seconds, stripping bulk at different potentials for different time periods (30, 60, 120 and 240 seconds) and then scanning potential. Scan rate: 50 mV s^{-1}. 42

3.13 Cyclic voltammetry of S/Ag(111) in acetic buffer. It was obtained depositing S from Na_2S solution in ammonia buffer on Ag(111), flushing the acetic buffer and then scanning the potential. Scan rate: 50 mV s^{-1}. 43
3.14 Stripping voltammetries' results of the exchange buffer test. Scan rate: 50 mV s^{-1}. 44
3.15 Stripping voltammetry of S/Sb/S/Ag(111) in ammonia buffer after the stripping of Sb. It was obtained depositing the second S layer at -0.68 V on Sb/S/Ag(111), oxidatively stripping Sb and then scanning the potential. Scan rate: 50 mV s^{-1}. 45
3.16 Stripping voltammetries of S/Sb/S/Ag(111) in ammonia buffer after the stripping of Sb. They were obtained depositing the second S layer at different potentials on Sb/S/Ag(111), oxidatively stripping Sb and then scanning the potential. Scan rate: 50 mV s^{-1}. 46
3.17 Stripping voltammetries of $[Sb/S]_2$/Ag(111) in ammonia buffer (S) and in acetic buffer (Sb). Sb voltammetries were performed first while S voltammetries were performed only after the complete stripping of Sb. Scan rate: 50 mV s^{-1}. 47
3.18 Stripping voltammetries of $[Sb/S]_2$/Ag(111) in ammonia buffer (S) and in acetic buffer (Sb). Sb voltammetries were performed first and S voltammetries were performed only after the complete stripping of Sb. The voltammetries were performed after Sb depositions for different times: 30 (red), 60 (green) and 120 seconds (blue). Scan rate: 50 mV s^{-1}. 48
3.19 Stripping voltammetry of Sb/S/Ag(111) in acetic buffer. It was obtained depositing Sb on S/Ag(111) at -0.32 V and then scanning the potential. Scan rate: 50 mV s^{-1}. 49
3.20 Stripping voltammetries of $S/[Sb/S]_2$/Ag(111) in ammonia buffer (S) and in acetic buffer (Sb). Sb voltammetries were performed first and S voltammetries were performed only after the complete stripping of Sb. The red series is the green one in Figure 3.17. Scan rate: 50 mV s^{-1}. 50

3.21 Stripping voltammetries of $[Sb/S]$ multilayers on Ag(111) in ammonia buffer (S) and in acetic buffer (Sb). Sb voltammetries were performed first and S voltammetries were performed only after the complete stripping of Sb. The blue series is the green one in Figure 3.20; the green one was performed after the deposition of $S/[Sb/S]_3$; the red one was performed after the deposition of $S/[Sb/S]_5$. Scan rate: 50 mV s^{-1}. 51
3.22 Primitive cell of Sb_2S_3. © Copyright FIZ Karlsruhe 2015 51
3.23 Cyclic voltammetries of 1 mM $NaSeO_3$ on Ag(111) in acetic buffer. The depositing voltammetry (red) was performed in presence of Se^{4+}ions; the stripping voltammetry (blue) was performed in the supporting electrolyte alone. Scan rate: 50 mV s^{-1}. 53
3.24 Stripping voltammetries of Se/Ag(111) in acetic buffer. The red one was performed after reductively stripping Se bulk at -0.75 V, the green one after reductively stripping Se bulk at -0.8 V. Scan rate: 50 mV s^{-1}. 54
3.25 Cyclic voltammetries of 0.5 mM $K_2Sb_2(C_4H_2O_6)_2$ on Se/Ag(111) in acetic buffer. Scan rate: 50 mV s^{-1}. 55
3.26 Stripping voltammetry of 1 mM $NaSeO_3$ on Ag(111) in 0.1 M NaOH. The peak indicated by C is originated by the stripping of a Se UPD monolayer. Scan rate: 50 mV s^{-1}. 56
3.27 Cyclic voltammetries of $ZnSO_4$ on Se/Ag(111) in ammonia buffer. Scan rate: 50 mV s^{-1}. 57
3.28 Stripping voltammetries of Zn in acetic buffer after multilayer depositions. The red curve is relative to the stripping of a Se/Zn/Se film on Ag(111), was obtained by stripping a $ZnSe$ film grown by 10 ECALE cycles ($Se/[Zn/Se]_{10}$). Scan rate: 50 mV s^{-1}. 58
3.29 Stripping voltammetries of Se in ammonia buffer after multilayer depositions. The red curve is relative to the stripping of a Se/Zn/Se film on Ag(111), the green was obtained by stripping a $ZnSe$ film grown by 10 ECALE cycles ($Se/[Zn/Se]_{10}$). Scan rate: 50 mV s^{-1}. 58
3.30 X-ray specular reflectivity. 60
3.31 X-ray reflectivity. 61
3.32 Primitive cell of $ZnSe$ Wurtzite. 61

3.33 Intensity maps at l=0, l=1, l=2 (according to *ZnSe* lattice parameters). Wurtzite unit cells rotated by 30° are indicated in black and green, Ag surface unit cell is indicated in red. h and k axis are referred to the Ag surface unit cell. 62
3.34 ZnSe-wurtzite powder pattern for $\lambda = 0.517$Å. 63
3.35 Intensity maps at l=0, l=1, l=2 (according to *ZnSe* lattice parameters). Lattice unit cells rotated by 10° are indicated in black and green; other two additional lattices are indicated in red and pink. Ag surface unit cell is indicated in red. h and k axis are referred to the Ag surface unit cell. 65
3.36 Intensity maps at l=0, l=1, l=2 (according to *ZnSe* lattice parameters). Lattice unit cell is indicated in black, Ag surface unit cell is indicated in red. h and k axis are referred to the Ag surface unit cell. 66
3.37 AFM image, 3D representation and roughness of the surface along drawn lines. 67
3.38 AFM images and roughness of the surface along drawn lines. 68
3.39 SEM images at different magnifications. 70

Chapter 1

Introduction

1.1 Chalcogenide multilayers as anodes for lithium-ion batteries

Batteries are extremely important in our lives and as telephones, computers, tablets, cars improve their performances, also batteries have to follow the same evolution to allow the innovation to become actually true. These days, lithium-ion batteries are diffusely used but they have to be constantly improved to keep up with latest power supply requests.

The main reasons for decrease of batteries performances are the irreversibility of the chemical reactions between electrodes and lithium-ion and the loss of electrical contact between the conductive media and the current collector. These effects bring to a capacity loss over several charge/discharge cycles. This contact loss is mainly caused by cracking due to the large volume change during lithiation/delithiation processes[1].

The aim of the overall project, a part of which is represented by this thesis, is to study the growth process and the consequent structure of new anodic materials for lithium-ion batteries in order to improve performances and lifetime of this product. This has to be pursued looking for inexpensive techniques and reproducible methods in order to make possible for companies to turn the scientific research into a valuable, profit-making business.

Many groups pointed out some characteristics of chalcogenides to consider them as good candidate for this purpose.
Prikhodchenko et al.[1] reported on the use of Sb_2S_3 nanocrystals coated with graphene

as a very stable and highly efficient anode for Li-ion batteries. The advantage of such material lays in its high capacity due to the capability of S ans Sb of forming compounds with Li.
Yu et al.[2] reported on the use of chalcogenide nanoparticles in sodium-ion batteries. These materials are interesting for their electrical contact stability due to small size, for the high capacity due to the low weight of S atoms and for the high efficiency due to the reversibility of sulfide compounds.
Further studies of Yu et al.[3] were oriented to use chalcogenides in bulk form as battery's anode instead of nanoparticles because they are more expensive and more challenging to produce. Even if the bulk material seems to be poorly stable, this work underlines the fact that the right choice of binder and electrolyte makes possible to stabilize the material.

1.2 Electrodeposition

1.2.1 Electrochemical cell

An electrochemical cell consists of two electrodes dipping in an electrolyte (generally a liquid conductor). The electrodes can be in different electrolytes, therefore divided by a salt bridge, or in the same one sharing a single compartment. Cells can be classified on the basis of the behavior of the reaction: if the reaction is spontaneous, the cell produces electricity due to the formation of a potential at the electrodes and the cell it is called galvanic cell; if the reaction is non-spontaneous, it has to be forced by an external potential applied at the electrodes providing to the electrolyte the energy to start the reaction and the cell it is called electrolytic cell.

Reactions happening in electrochemical cells are redox ones as there is one species that loses electrons (reducing agent) and another one that gains electrons (oxidizing agent), so they can be split in two half-reaction, one involving oxidation and the other reduction.

$$\text{Reduction term: } Ox_1 + \nu e^- \rightarrow Red_1$$

$$\text{Oxidation term: } Red_2 \rightarrow Ox_2 + \nu e^-$$

$$\text{Overall reaction:} Ox_1 + Red_2 \rightarrow Red_1 + Ox_2$$

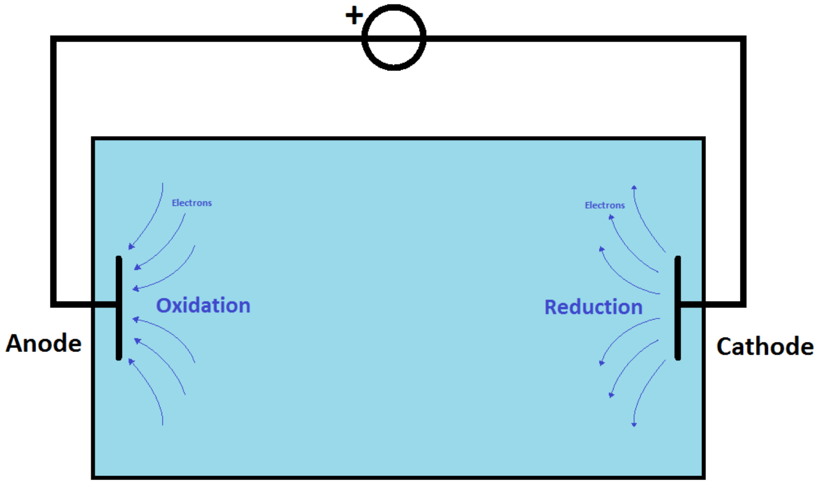

Figure 1.1: Electrolytic cell.

This concept is useful to visualize the separation in space of the overall reaction: as the reduction takes place on one electrode (cathode), the oxidation takes place on the other one (anode). As a consequence electrons released by the oxidation part can travel in the the external circuit and end to the opposite electrode allowing the reduction part of the reaction. As already stated above, in an electrolytic cell this process has to be forced, therefore the anode potential has to be kept, by an external force, relatively positive to the cathode one (Figure 1.1).

In a galvanic cell the spontaneous reaction lead to the formation of a potential between the two electrodes and the electromotive force can be derived as follows. Let's define the extent of reaction ξ indicating the amount of substance that, during a reaction, turns from substance A to substance B. By this quantity the reaction Gibbs energy is defined as:

$$\Delta G_r = \left(\frac{\partial \mathrm{G}}{\partial \xi}\right)_{p,T} \tag{1.1}$$

The maximum work that a reaction can do during its advance of dξ is then

$$dw_e = \Delta G_r d\xi$$

As during this dξ advance the transported charge between electrodes is $-\nu e N_a d\xi$, the work done by the system is

$$dw_e = -\nu e N_a d\xi E$$

Equating the two expressions, we obtain

$$\Delta G_r = -\nu F E$$

where $F = eN_a$ is the Faraday constant and then the potential difference is

$$E = -\frac{\Delta G_r}{\nu F} \tag{1.2}$$

We take into account the expression relating the reaction Gibbs energy to the composition of the reaction mixture $\Delta G_r = \Delta G^{\ominus} + RT\, ln\, Q$, where Q is the reaction coefficient and $\Delta G^{\ominus}$ represents the reaction Gibbs energy in the case in which each ion species behaves ideally: in fact the last term is due to the presence, around each ion, of more counter ions than similar ones creating an ionic atmosphere that modifies the system energy. Dividing by $-\nu F$, we obtain

$$E = E^{\ominus} - \frac{RT}{\nu F}\, ln\, Q \tag{1.3}$$

with $\Delta G^{\ominus} = -\nu F E^{\ominus}$. This is the Nernst equation for the zero-current cell potential.

In an electrolytic cell we have the opposite situation when the potential is not arising from the reaction but it is applied to allow the reaction to take place.

1.2.2 Electrodeposition methods

Electrodeposition is a technique that is well-suited to the preparation of nanostructures. In electrodeposition processes the amount of deposited material is related to the charge transferred during the process and can be controlled simply through the Faraday's law. Nevertheless a better control of the growth can be obtained exploiting chemical interactions between surface and adlayers which lead to the phenomenon known as Under Potential Deposition (UPD). Different strategies have to be employed to control the electrochemical growth, depending on the substrate chemical/electrochemical reactivity and the kind of deposited material. In this section an introduction to Overpotential and Underpotential deposition is reported, moreover general features of electrochemical epitaxy will be treated.

1.2.3 Under Potential Deposition

Within a pure metal/metal-ion electrolyte system of a specific metal the onset of deposition (or dissolution) is well defined by the respective Nernst equilibrium potential. However, for metal deposition on a foreign metal substrate, we have to consider the interaction of the substrate atoms S with the deposited adlayer Me_{ad}. When the interaction of S-Me_{ad} is stronger than the Me_{ad}-Me_{ad} interaction, the first adlayer (in some cases also a double layer) is already deposited at potentials preceding the Nernst one. This effect can be used as a single monolayer deposition technique and is called Underpotential Deposition (UPD) [29]. UPD provides a unique method for a controlled, often exactly one monolayer, metal deposition on a foreign substrate in a potential window before the onset of bulk deposition. Such phenomenon allows for the precise and reproducible control of the surface coverage and for the study of coverage-dependent properties including the structure of the metallic adlayer and its electronic properties.

In the case of phase formation on foreign substrates the overall reaction between the adlayer Me_{ad} and the element in solution (Me_{sol}) is given by:

$$\mathrm{Me}_{ad} \Leftrightarrow \mathrm{Me}_{sol}^{z+} + ze^{-} \tag{1.4}$$

The thermodynamic equilibrium is given by the Nernst equation:

$$E_{\mathrm{Me}_{ad}/\mathrm{Me}_{sol}^{z+}} = E^{o}_{\mathrm{Me}_{ad}/\mathrm{Me}_{sol}^{z+}} + \frac{RT}{zF} \ln \frac{a_{\mathrm{Me}_{sol}^{z+}}}{a_{\mathrm{Me}_{ad}}} \tag{1.5}$$

Then, the potential of stability of 3D bulk phases is given by $E = E_{\mathrm{Me}_{ad}/\mathrm{Me}_{sol}^{z+}}$. However, for small 3D cluster phases, the potential of stability can be more negative, $E < E_{\mathrm{Me}_{ad}/\mathrm{Me}_{sol}^{z+}}$. As a matter of fact, possible deviations of the atomic arrangement of the initial small clusters from the 3D-bulk crystal one, can determine additional energy terms that increase the total Gibbs energy of the system. On the contrary, for some 2D phases the potential of stability can even be more positive, $E > E_{Me/M_{e_{z+}}}$.

This latter case corresponds to the underpotential deposition that occurs in the presence of specific interactions between the depositing metal and the substrate. By convention the potential difference $E - E_{\mathrm{Me}_{ad}/\mathrm{Me}^{z+}_{sol}}$ is defined as ΔE relative to the UPD or OPD (Overpotential Deposition) process. Then, the Nernst equilibrium potential, $E_{Neq} = E = E_{\mathrm{Me}_{ad}/\mathrm{Me}^{z+}_{sol}}$, represents the limit of the stability range of both 2D and 3D Me phases. That means that, at E_{Neq}, 2D and 3D Me phases coexist and, as a consequence, the underpotential deposition and overpotential deposition of Me on S are connected with the formation of 2D and 3D Me phases, respectively. The process of Me OPD on S becomes identical with that of Me OPD on Me if the deposited Me film on S exceeds a certain thickness (usually from one to twenty monolayers) and behaves like a 3D Me bulk phase. Of course, the kinetics of the deposition process should also be taken into account. The most important parameters determining the mechanism of UPD and OPD of Me on a foreign substrate are the Me_{ad}-S binding energy ($\Psi_{Me_{ad}-S}$) and the crystallographic misfit between S and a 3D Me deposit. Limiting ourselves to the thermodynamic aspects (that is, considering the deposition process at nearly equilibrium conditions, so as to neglect kinetic effects), two different growth modes can be distinguished:

1. $\Psi_{Me_{ad}-S} < \Psi_{Me_{ad}-Me_{ad}}$
   The surface concentration of Me_{ad} at $E_{\mathrm{Me}_{ad}/\mathrm{Me}^{z+}_{sol}}$ is small, and OPD of a 3D Me bulk phase takes place on an unmodified substrate surface according to the Volmer-Weber or 3D islands growth mode independent of crystallographic Me-S misfit.

2. $\Psi_{Me_{ad}-S} > \Psi_{Me_{ad}-Me_{ad}}$
   Then, 2D Me_{ad}-S phases can be formed in the UPD range and the surface concentration of Me_{ad} at $E_{\mathrm{Me}_{ad}/\mathrm{Me}^{z+}_{sol}}$ can reach one or more Me_{ad} monolayers depending on $\Psi_{\mathrm{Me}_{ad}-S}$. Two different subcases can be distinguished:

   - if the crystallographic Me-S misfit is negligibly small, 2D Me UPD overlayers and 3D Me crystallites are epitaxially oriented following the Frank-van der Merwe mechanism.
   - in the presence of significant crystallographic Me-S misfit, the growth mechanism is the Stranski-Krastanov mode with unstrained 3D Me bulk phase on top of a strained 2D Me_{ad} phase.

1.2.4 ECALE electrodeposition

The electrochemical deposition of a compound can be obtained by the alternate electrodeposition of UPD layers of the elements forming the compound. In electrochemical ALE (EC-ALE)[9, 10] a solution containing a precursor for a first element reacts at a controlled potential with the substrate. The solution is then exchanged for one containing a precursor of the second element, from which an atomic layer of it is deposited at a controlled potential, completing the deposition of one monolayer of the compound. Thin films are grown by repeating this cycle as many times as desired. Schematically the ECALE cycle requires four steps:

- UPD of the first element
- Rinsing
- UPD of the second element
- Rinsing

In terms of speed and simplicity, ECALE is not competitive with co-deposition (direct deposition of a compound from a solution containing all the precursors); however, the degrees of freedom available in co-deposition are severely limited compared to ECALE. ECALE provides much increased control over deposit structure, morphology and composition, by having separately optimized solutions and potentials for each element. In addition, as ECALE is based on layer by layer growth, epitaxy can be facilitated and the thickness of the deposit is determined by the number of deposition cycles. The atomic layer control is a necessary prerequisite in the formation of nanostructured materials. Control of growth at the nanometer scale is a major frontier of Material Science. By forming nanocrystalline materials and by constructing superlattices, nanowires and nanoclusters, the electronic structure (bandgap) of a semiconductor can be engineered.

Chapter 2

Experimental

2.1 Ag(111) Substrates

Surface X-ray Diffraction experiments are very sensitive to surface quality of the substrates. For such kind of experiments extremely flat surfaces with a very low amount of defects are required: presence of roughness, facets, crystallographic defects and a lack of parallelism of the surface affect enormously the quality of the data collected and might make very difficult the data treatment and analysis. Electrochemical techniques are way less sensitive to structural defects of the substrate while on the other hand are extremely sensitive to chemical contamination. Moreover, electrochemical tests can be extremely fast and the availability of a large amount of freshly prepared samples to repeat electrodeposition experiment is mandatory to efficiently carry on any electrochemical characterization. For this reasons substrates used in laboratory for electrochemical tests and in x-ray experiments have been prepared according with two different procedures to fulfill the requirements of the different techniques. Samples used in electrochemical experiments were prepared by chemical etching of the surface, while deposition of thin films for crystallographic analysis was done on surfaces prepared using UHV techniques. The samples were cleaned further by electrochemical means once mounted in the electrochemical cell.

2.1.1 Surface Chemical Preparation

The electrodes were manually polished with emery paper (BuehlerMet SiC P1000, p2500, P4000) and successively finer grades of alumina powder down to 0.05 μm (Buehler Micropolish II). Before each measurements, the electrode was cleaned with water in ultrasonic bath for 5 minutes and then chemically polished with CrO_3 according to the procedure described in literature[30, 31, 32]. The procedure consists in dipping the electrode in concentrated $HClO_4$ (70%) and subsequently in a solution of 0.1 M CrO_3 in 0.1 M HCl. The electrode is then rinsed with water and left in concentrated NH_4OH (33%) for 10 minutes. To eliminate possible organic contaminants on the surface, the electrode is finally soaked in concentrated sulfuric acid for about 5 minutes and then rinsed thoroughly with ultrapure water. This etching method is very efficient in producing clean Ag(111) surfaces, nevertheless the chemical oxidation of the surface leads to the formation of facets which make impossible the application of this procedure for the production of samples suitable for SXRD experiments.

2.1.2 UHV preparation

Ag(111) polished electrode were supplied by Surface Preparation Laboratory (SPL). The surface was prepared in a UHV chamber with several sputtering-annealing cycles. The quality of the surface was checked with LEED after each sputtering annealing cycle. Samples were sputtered at room temperature with Ar ions at 1x10^{-5} mbar and 1.5 keV for 30 minutes. Then the substrate was then annealed at 550ºC for 5 minutes.

2.1.3 Electrochemical preparation

Once mounted in the cell the substrates were electrochemically cleaned. The standard electrochemical cleaning procedure permits the desorption of contaminants from the surface by the application of potentials in the hydrogen evolution region and close to the onset of the Ag oxidation. Before each experiment the following cleaning procedure was carried on in ammonia buffer:

- Potential set at -1.6 V (vs Ag/AgCl 3.5M KCl) for 60 seconds
- Solution exchange
- Potential set to -0.1 V (vs Ag/AgCl 3.5M KCl) for 60 seconds
- Solution exchange

In Figure 2.1 are reported cyclic voltammograms for Ag(111) in ammonia buffer before and after the electrochemical cleaning procedure. It is clear from the plot that the capacity of the system is decreasing after the treatment as well as the current involved in the hydrogen evolution region and the curve obtained is closer to the ones reported in literature for a clean Ag(111) surface.

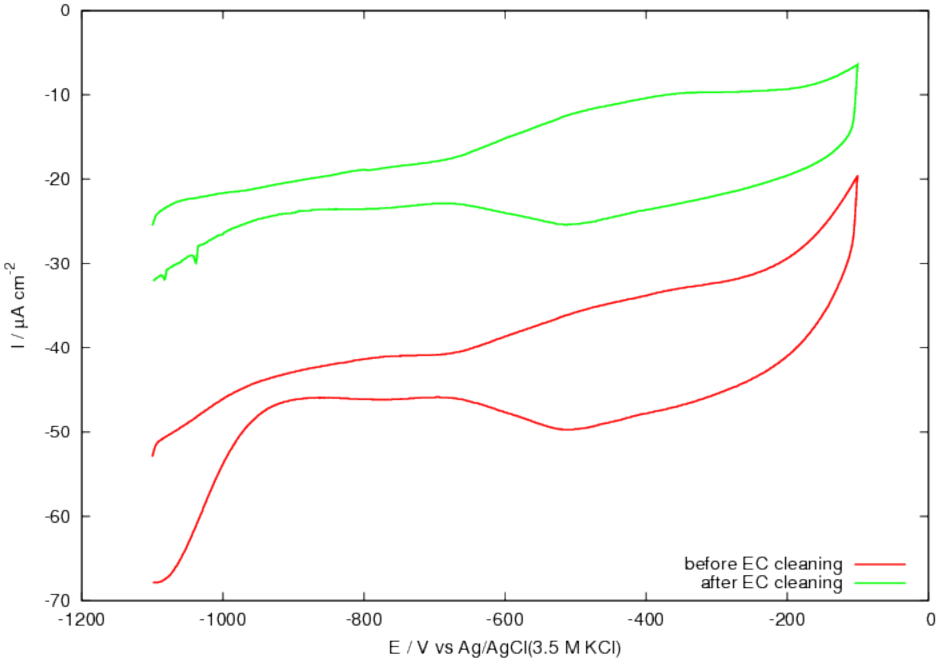

Figure 2.1: Cyclic voltammetry of Ag(111) in ammonia buffer. Scan rate: 50 mV s^{-1}.

2.2 Cyclic voltammetry

Cyclic voltammetry is an electrochemical method to study properties of redox species in solution. Cyclic voltammetry experiments employ an electrochemical cell with a three electrodes configuration: a working electrode, counter electrode and reference electrode. Reactions take place at the working electrode, the reference one is used to monitor the potential applied at the working electrode and the counter electrode allows electrons to flow through the cell without flowing in the reference electrode. In fact the reference electrode is necessary to measure the potential applied on the working electrode and its electrode potential remains stable as long as the electrode is non-polarized. The counter electrode can not be used for this purpose because the potential measured between the latter and the working electrode is influenced by the overpotential generated by the electrochemical reactions taking place at the counter electrode surface, making thus impossible to know which is the potential at the interface between the working electrode and the solution. As visible in Figure 2.2 a potential is set between working and counter electrode and is controlled by measuring the potential between working and reference electrode; an ammeter measures the current intensity flowing through the working electrode. A necessary condition is that the solution is conductive in order to allow the electron flow, for this purpose a supporting electrolyte (an electrochemically inert salt) is normally add to the solution.

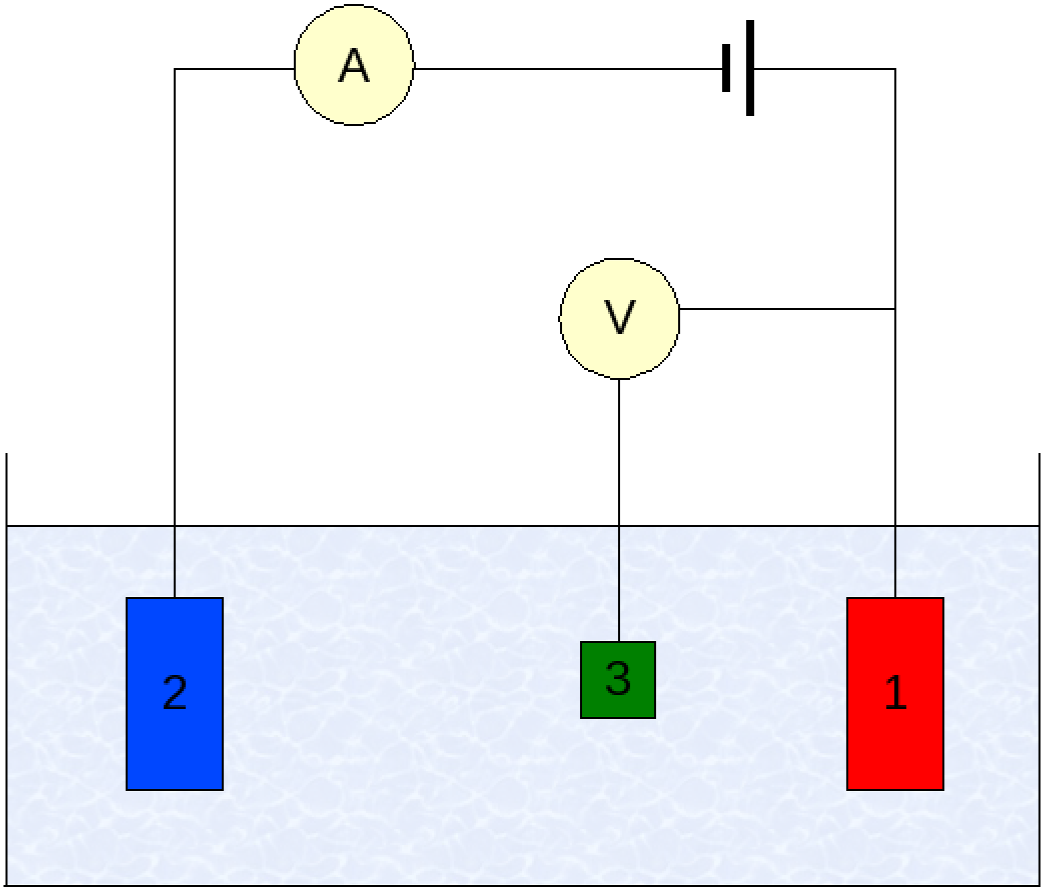

Figure 2.2: Diagram of a three-electrode cell. 1 is the working electrode, 2 is the counter electrode, 3 is the reference electrode.

During a cyclic voltammetry experiment, the applied potential is a triangular wave so that the potential is ramped linearly versus time from a starting potential to another potential value and then back. This scan can be repeated several times in order to investigate chemical, electrochemical and kinetical effects at the interface. While the potential is changing, the current intensity is measured in order to see the reduction and oxidation reactions taking place at the surface of the working electrode. In Figure 2.3 it can be seen an example of cyclic voltammetry: the important characteristics of this graph are the peak's potentials (E_p) and the peak's current intensities (i_p); the area under the peak represent the total charge deposited on the electrode or stripped from it. For this reason it gives the quantitative result of what is happening on the surface.

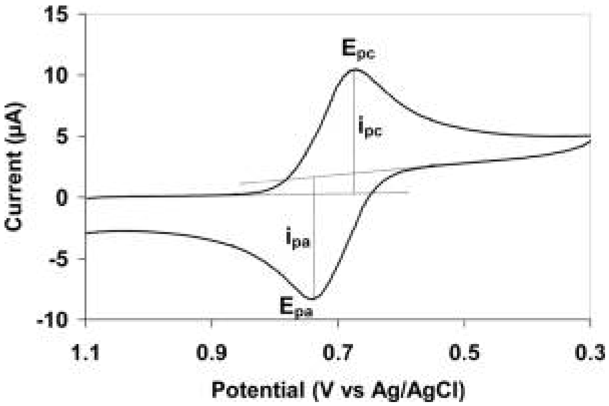

Figure 2.3: Cyclic voltammetry example.

2.3 Electrodeposition apparatus

For our electrodeposition experiments a flow-cell was used (Figure 2.4a). This cell is made of PEEK (polyether ether ketone) because of the mechanical properties of this material, its low density and its stability under the x-ray beam. This properties allow the cell to be used for in-situ electrochemical experiments during x-ray exposure as the photons can reach the sample and then the detector without damaging the cell itself: in order to reduce the background noise generated by the cell and increase the transmission, the walls around the sample are 0.1 mm thick. For practical reasons, during laboratory tests not requiring x-ray beams, cells with 1-mm-thick walls are used. The solution in the cell can be exchanged during the experiment without losing the control over the applied potential. Two Teflon tubes are mounted on the side walls, the inlet is pointing downward to make the solution go straight to the working electrode to allow a complete exchange of the solution, while the outlet is mounted on the top of the cell in order to make easier the removal of gas bubbles which might be formed during electrochemical reactions.

The diagram in Figure 2.4b shows the position of the electrodes in this cell. The working electrode is placed in the bottom part to avoid gas accumulation on the electrode surface; its particular shape is useful during the preparation and the cleaning of the substrate in ultra-high vacuum as it can be fixed on the sample-holder.

The counter electrode is a 5-cm long rod of glassy carbon mounted on the top of the cell and dipping in the solution. This configuration allows gas bubbles, formed during oxygen or hydrogen evolution reactions, to move upward without interrupting the electrical contact.

Finally the reference electrode is commercial Ag/AgCl in 3.5M KCl solution: it is a silver wire covered with AgCl in a rigid PEEK tube with a leakless ceramic frit at the bottom. All potentials of the performed tests are intended (vs Ag/AgCl (3.5M KCl)) if not further specified.

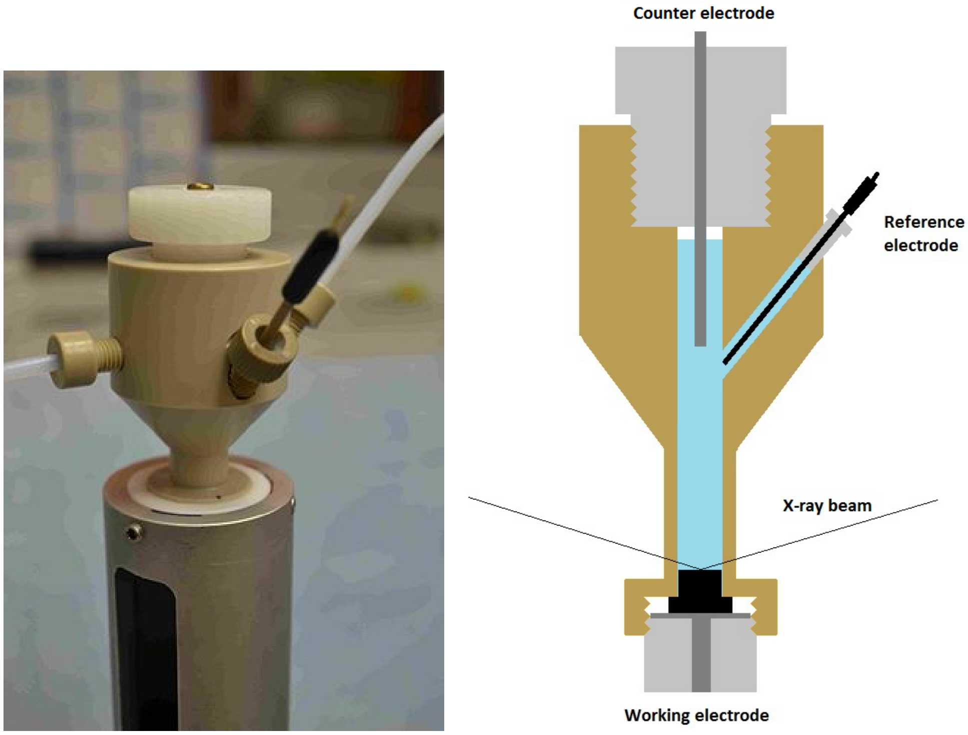

(a) Flow cell mounted on the diffractometer.

(b) Flow cell diagram.

Figure 2.4: Flow cell.

Electrodes are connected with a shielded cable to a potentiostat. During the experiment a Parstat 263 potentiostat (Princeton) was used, remotely controlled via a GPIB port by using SPEC based macros.

The solution in the cell can be exchanged thanks to the system shown in Figure 2.5: in the bottom shelf there are waste tanks in which the solutions from the cell outlet are collected, in the top shelf are housed the reservoirs for the solutions (Duran bottles of 0.5, 1 or 2 liters volume). The bottles are pressurized (0.3 bar) with Nitrogen or Argon and a gas recirculation circuit allows to bubble the inert gas in the solutions to remove the oxygen dissolved in the solvent. On the top of the rack it is visible the potentiostat used in these experiments.
The reservoirs are connected to a distribution system which consists of a series of valves controlled manually or through the SPEC interface which allows to control the flow of the solutions to the cell inlet. This method assure the fast and safe exchange of solutions in the cell.

The system has to be cleaned before each experiment to avoid any contaminant in the cell. In order to remove any trace of contaminants, the glass parts are cleaned in concentrated sulfuric acid and then rinsed with ultrapure water while the PTFE tubes and the valve system is cleaned by recirculating a solution of 10% H_2SO_4 and 10% H_2O_2 and then rinsing profusely with ultrapure water.

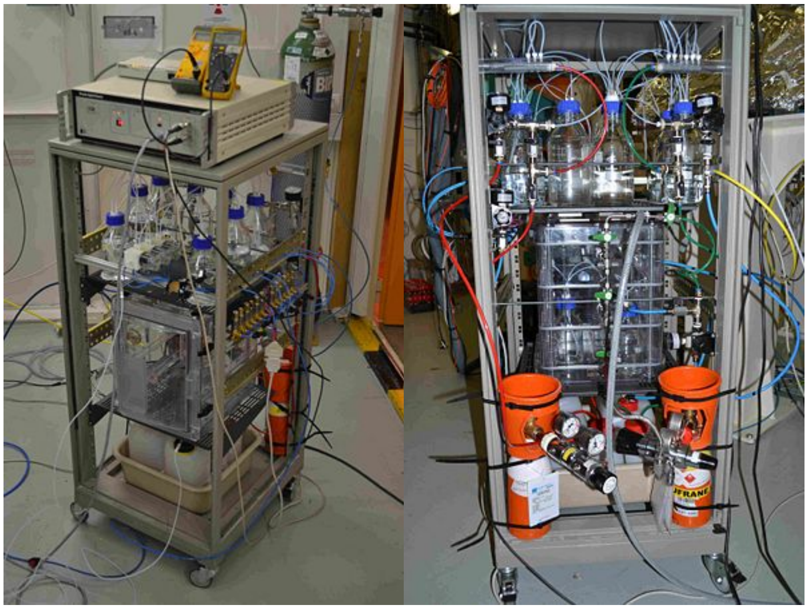

(a) Front. (b) Back.

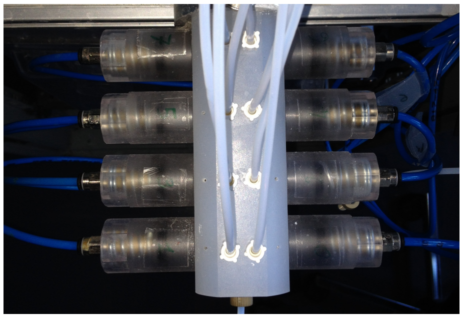

(c) Valves.

Figure 2.5: Electrochemistry rack.

2.4 Chemicals

All the solutions were prepared using 18.2 MΩ ultrapure water supplied by a Millipore's Milli-Q system.

Ammonia buffer pH 8.5 solution was prepared diluting 4.4 ml of $HClO_4$ (70%) (Aldrich, ACS grade) and 8 ml of NH_4OH (30%) (Aldrich, ACS grade) in 1 l of ultrapure water. For the sulfide deposition a 0.5 mM Na_2S (Aldrich, >98%) solution in ammonia buffer was used. Sb solution in ammonia buffer was prepared using 34 µM Sb_2O_3 (Fluka, puriss. p.a).

For the 0.1M NaOH solutions was used NaOH (ACS grade). Two solutions based on this buffer are prepared respectively using 1 mM Na_2S and 27 µM Sb_2O_3.

Acetic buffer was prepared diluting 11.6 ml of glacial acetic acid (Fluka) and 6 g of NaOH in 1 l of ultrapure water to obtain pH 5. Two solutions based on this buffer are prepared respectively using 0.5 mM $K_2Sb_2(C_4H_2O_6)_2 \cdot 3H_2O$ and 1 mM Na_2SeO_3.

2.5 Structural characterization

2.5.1 Diffraction

2.5.1.1 Crystal structure

A crystal is a set of atoms ordered both micro- and macroscopically: this order arises from the fact that these structures are periodic. The periodicity is the basis of the definition of the Bravais lattice: it is the mathematical set of points that are identified by a formula $\mathbf{R} = R_1\mathbf{a}_1 + R_2\mathbf{a}_2 + R_3\mathbf{a}_3$, where R_i are integers and $\mathbf{a}_i$ are independent vectors. So defined points can be also seen as a set of points for which is true that each of them sees the same configuration of nearest neighbors. A crystal is represented by the lattice joined with a base that is formed by the atoms linked to each lattice point: they can be one or more depending on the crystal we are representing. An important concept is the unit cell that is the volume of space identified by three primitive vectors and that have the property of covering the whole space without overlapping if moved on each point of the lattice.

For each real lattice exists the reciprocal lattice that is abstract but it is extremely useful to describe diffraction. As the real lattice is by definition periodic, it can be described, in the simpler 1D case, by a periodic function $f(x)$ expanded in Fourier series

$$f(x) = \sum_{n=-\infty}^{\infty} A_n e^{\frac{i2\pi nx}{a}}$$

where a is the period of the lattice; A_n are the coefficients of the expansion and represents the projections of the function on a complete orthonormal set of plane waves e^{ig_nx}:

$$A_n = \frac{1}{a}\int_0^a f(x)\, e^{-ig_nx}dx$$

with $g_n = n\frac{2\pi}{a}$ defined as a wave vector. These wave vectors are defining another lattice called reciprocal lattice that actually is a Bravais lattice itself.

In the 3D case the periodic function becomes

$$f(\mathbf{r}) = \sum_{\mathbf{g}} A_{\mathbf{g}} e^{i\mathbf{g}\cdot\mathbf{r}} \tag{2.1}$$

with $\mathbf{r} = r_1\mathbf{a}_1 + r_2\mathbf{a}_2 + r_3\mathbf{a}_3$ and $A_{\mathbf{g}} = \frac{1}{V_{cell}} \int_{cell} f(\mathbf{r})\, e^{-i\mathbf{g}\cdot\mathbf{r}} dV$. As the function has to respect the periodicity $f(\mathbf{r}) = f(\mathbf{r}+\mathbf{R})$ not all the $\mathbf{g} = n_1\mathbf{b}_1 + n_2\mathbf{b}_2 + n_3\mathbf{b}_3$ vectors are allowed but only the ones for which

$$e^{i\mathbf{g}\cdot\mathbf{R}} = 1 \tag{2.2}$$

In the general case of non-orthogonal $\mathbf{a}_i$ vectors, the consequent condition

$$\mathbf{g}\cdot\mathbf{R} = integer \cdot 2\pi$$

is fulfilled by

$$\mathbf{b}_1 = 2\pi\frac{\mathbf{a}_2\times\mathbf{a}_3}{\mathbf{a}_1\cdot(\mathbf{a}_2\times\mathbf{a}_3)}; \quad \mathbf{b}_2 = 2\pi\frac{\mathbf{a}_3\times\mathbf{a}_1}{\mathbf{a}_2\cdot(\mathbf{a}_3\times\mathbf{a}_1)}; \quad \mathbf{b}_3 = 2\pi\frac{\mathbf{a}_1\times\mathbf{a}_2}{\mathbf{a}_3\cdot(\mathbf{a}_1\times\mathbf{a}_2)} \tag{2.3}$$

as $\mathbf{b}_i\cdot\mathbf{a}_j = 2\pi\delta_{ij}$.

To identify a certain plane of the real lattice it is convenient to use the reciprocal lattice vector perpendicular to the plane itself. If the vector is the one with minimum modulus, its components n_i are called Miller indices and are written (hkl).

2.5.1.2 X-Ray Diffraction

Diffraction is the phenomenon happening when x-rays hit the lattice of a crystal. Taking into account a simple Bravais lattice with a one-atom base, diffraction can be explained by Von Laue formulation. Let's imagine, as in Figure 2.6, to have an incoming x-ray (with $\hat{\mathbf{n}}$ direction) and an outgoing x-ray (with $\hat{\mathbf{n}}'$ direction), scattered by two points of the lattice separated by a vector $\mathbf{d}$. We see that the longer path must differ from the other by an integer multiple of the wavelenght λ

$$\mathbf{d}\cdot(\hat{\mathbf{n}}' - \hat{\mathbf{n}}) = m\lambda$$

from which we obtain $\mathbf{d}\cdot(\mathbf{k}'-\mathbf{k}) = m\,2\pi$, simply multiplying by $2\pi/\lambda$. This is

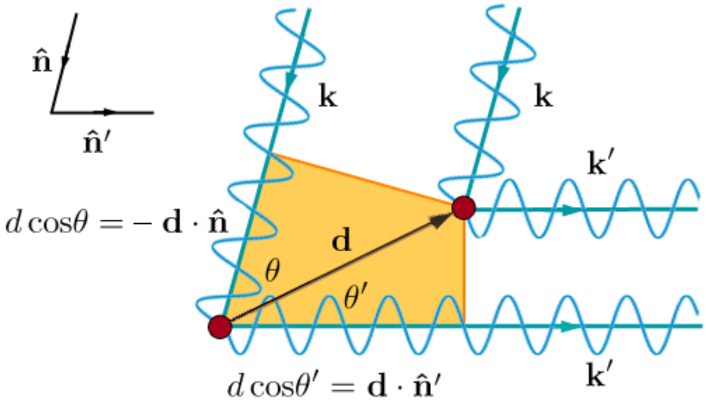
$\hat{\mathbf{n}}$
$\hat{\mathbf{n}}'$
$\mathbf{k}$
$\mathbf{k}$
$\mathbf{k}'$
$d\cos\theta = -\,\mathbf{d}\cdot\hat{\mathbf{n}}$
$\mathbf{d}$
θ
θ'
$d\cos\theta' = \mathbf{d}\cdot\hat{\mathbf{n}}'$
$\mathbf{k}'$

Figure 2.6: Von Laue formulation.

equivalent of

$$e^{i(\mathbf{k}'-\mathbf{k})\cdot\mathbf{R}} = 1$$

as it must be true for each lattice vector $\mathbf{R}$.

From the comparison with Eq. 2.2, we obtain

$$\mathbf{g} = \mathbf{k}' - \mathbf{k} \tag{2.4}$$

and therefore $\mathbf{k}' = \mathbf{k} - \mathbf{g}$. Taking the squared norm of these vectors

$$|\mathbf{k}'|^2 = |\mathbf{k} - \mathbf{g}|^2 = |\mathbf{k}|^2 + |\mathbf{g}|^2 - 2\,\mathbf{k}\cdot\mathbf{g}$$

we obtain, as $|\mathbf{k}'| = |\mathbf{k}|$,

$$\mathbf{k}\cdot\mathbf{g} = \frac{1}{2}\,|\mathbf{g}|^2 = \frac{1}{2}\,|\mathbf{g}|\,|\mathbf{g}|$$

and consequently

$$\mathbf{k}\cdot\hat{\mathbf{n}}_{\mathbf{g}} = \frac{|\mathbf{g}|}{2} \tag{2.5}$$

This means that, to have diffraction, the projection of the incident wavevector must be half of the norm of a reciprocal lattice vector.

From Eq. 2.4, three equations can be deduced, totally equivalent to Eq. 2.5.

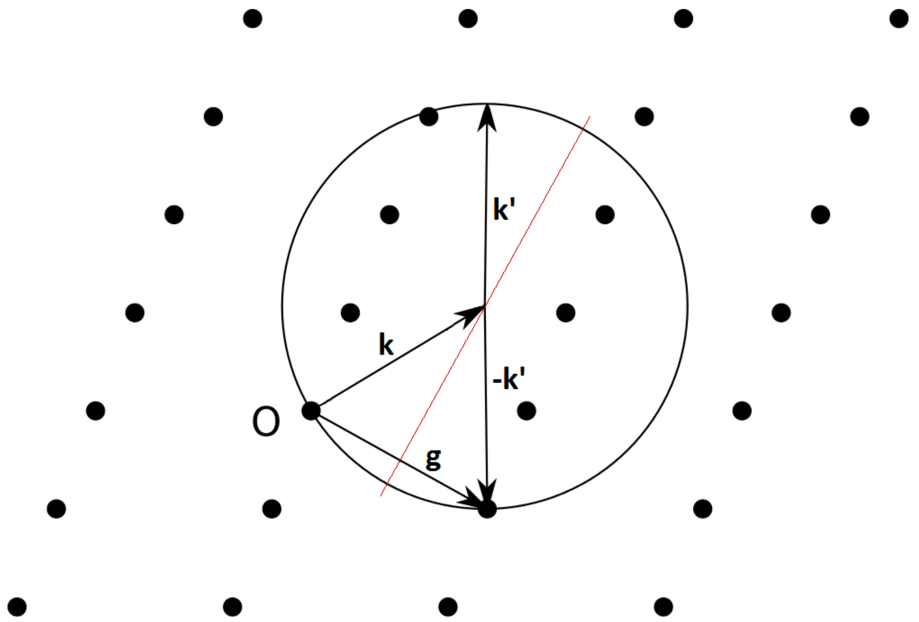

Figure 2.7: Ewald sphere.

Reminding that $\mathbf{g} = n_1\mathbf{b}_1 + n_2\mathbf{b}_2 + n_3\mathbf{b}_3$, Laue equations are

$$\begin{aligned}\mathbf{b}_1 \cdot (\mathbf{k}' - \mathbf{k}) &= 2\pi\, h \\ \mathbf{b}_2 \cdot (\mathbf{k}' - \mathbf{k}) &= 2\pi\, k \\ \mathbf{b}_3 \cdot (\mathbf{k}' - \mathbf{k}) &= 2\pi\, l\end{aligned} \tag{2.6}$$

A smart way to see this condition is representing it as the Ewald sphere (Figure 2.7): dots are points in the reciprocal lattice with origin O, $\mathbf{k}$ and $\mathbf{k}'$ are respectively the incident and the diffracted wavevectors, $\mathbf{g}$ is a reciprocal lattice vector. We graphically see that the difference between $\mathbf{k}$ and $\mathbf{k}'$ must equal $\mathbf{g}$ and this happens when the sphere touches one lattice point. To investigate the reciprocal space it is possible to enlarge the sphere changing the energy of the incident ray, to rotate the lattice rotating the crystal or to diffract a crystal powder so then a single crystal is already present statistically in all his rotations.

If the crystal has a base with more than one atom, not all theoretical points of the reciprocal lattice are visible because of the structure factor. It takes into account the whole structure that results to be equivalent to more identical shifted reciprocal lattices. Each of these lattices diffracts waves with the same diffraction condition but with different phases. If $\mathbf{d}_j$ is the distance between the lattice point $\mathbf{R}_i$ and one atom of the base, the phase shift is $\mathbf{d}_j \cdot \mathbf{g}$. The total phase shift is the sum over the

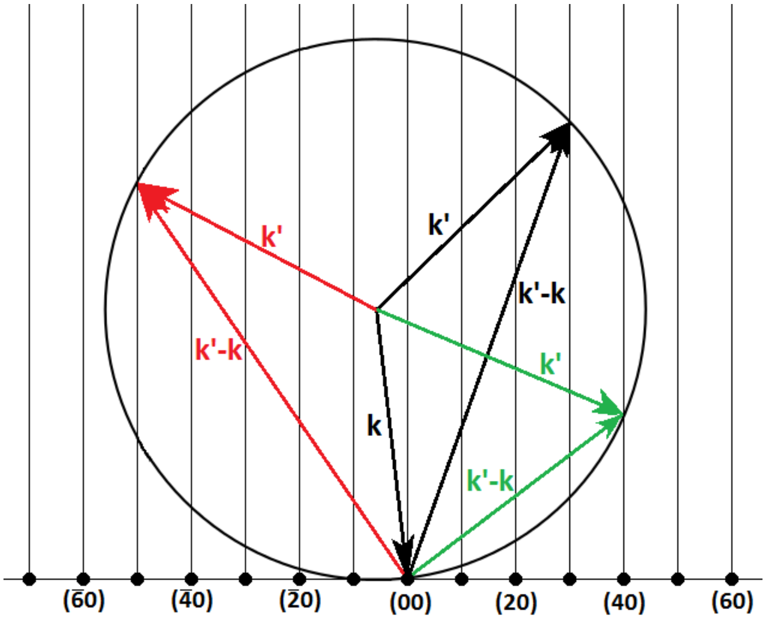

Figure 2.8: Ewald sphere for surface diffraction.

n base's atoms

$$S_{\mathbf{g}} = \sum_{j=0}^{n} e^{i\mathbf{g}\cdot\mathbf{d}_j}$$

This is the structure factor and it can lead to the suppression of some peaks of the Bravais lattice alone, as the Bragg peaks intensity is proportional to $|S_{\mathbf{g}}|^2$.

2.5.1.3 Surface X-Ray Diffraction

When diffraction is performed on a single atomic layer of a crystal, one of the three Laue equations (Eq. 2.6) is not valid anymore because it refers to the third dimension of the lattice: in fact Eq. 2.4 becomes

$$\mathbf{g}_{/\!/} = \mathbf{k}'_{/\!/} - \mathbf{k}_{/\!/} \tag{2.7}$$

The reciprocal lattice is not represented anymore by points but by lines, called rods, that originate by the 2D lattice extending without discretization to infinite (Figure 2.8). For this reason, each (with big enough norm) incident wavevector can satisfy Eq. 2.7 and, as visible in the figure, more than one Bragg peaks usually appear.

This is valid if we consider an ideal 2D lattice but if we have a thin film, then

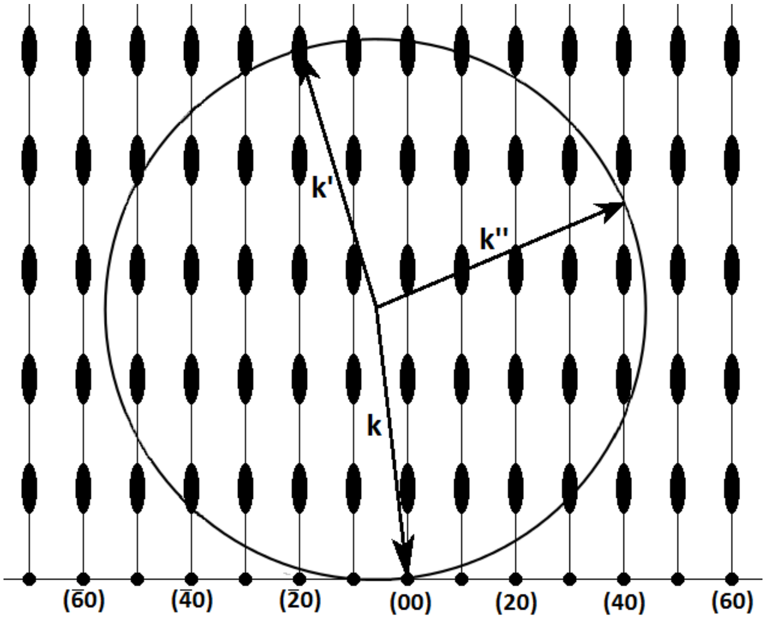

Figure 2.9: Ewald sphere for thin film diffraction.

the third Laue equation is not negligible anymore even if it is not a strong condition as for the bulk diffraction. We can see in Figure 2.9 that it is still present a rod structure as in the previous case but the intensity along rods is not constant but periodically modulated. The result is having the same Bragg peak of the ideal 2D lattice but some ($\mathbf{k}'$ in figure) have higher intensity than other ($\mathbf{k}''$ in figure). With the film thickness increasing, the intensity modulation becomes more strong until reaching the 3D lattice situation where thicker rod regions turn into points.

2.5.2 Reflectivity measurements

The refraction index for a film hit by x-rays is

$$n = 1 - \delta + i\beta$$

with $\delta = \frac{\lambda^2}{2\pi} r_e \rho_e$ and $\beta = \frac{\lambda}{4\pi}\mu_x$. r_e is the classical electron radius, ρ_e is the electron density of the material and μ_x is the absorption length. If $\delta > 0$, then $n < 1$ and we obtain the total external reflection for incident angles below the critical angle $\alpha_c = \sqrt{2\delta}$.

When we consider just the specular reflectivity ($\alpha_i = \alpha_f$) as represented in Figure 2.10, we have the momentum transfer $\mathbf{Q} = \mathbf{k}_f - \mathbf{k}_i$ perpendicular to the surface. The

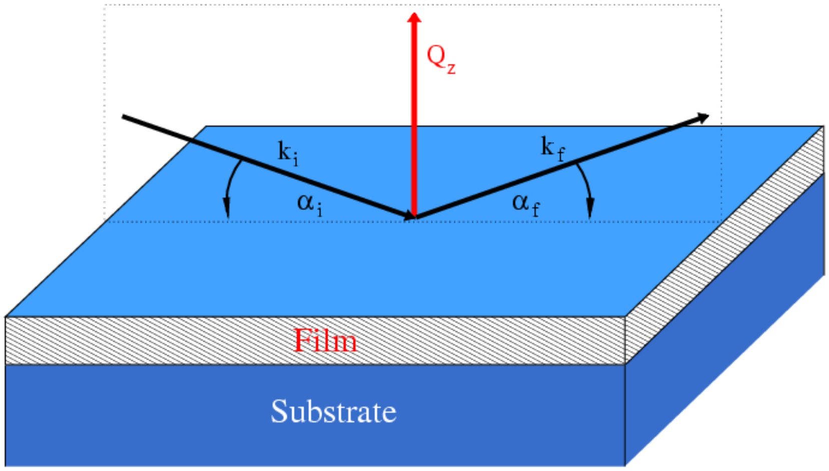

Figure 2.10: Figure 1 of Schreiber's review[8] on reflectivity: specular reflectivity of x-rays on a thin film surface.

component of this vector is then all along the z axis

$$\mathbf{Q}_z = \frac{4\pi}{\lambda} sin\,\alpha_i$$

For an ideal flat surface, the Fresnel reflection coefficient of the electrical field is

$$r = \frac{k_{i,z} - k_{f,z}}{k_{i,z} + k_{f,z}}$$

with $k_{i,z}$ and $k_{f,z}$ as z-component of respective vectors. Near the critical angle

$$k_{f,z} = k\sqrt{\alpha_c - \alpha_i}$$

resulting in an imaginary quantity when $\alpha_i < \alpha_c$, and therefore in a total reflection of the beam. When α_i becomes larger, the reflected intensity $R = |r|^2$ drops rapidly as ${}^1/_{\alpha_i^4}$.

A non-ideality element is the roughness σ of the surface that introduce a factor strongly decreasing the total intensity

$$r_{real} = r_{ideal} e^{-2k_{i,z}k_{f,z}\sigma^2}$$

When more than one interfaces are present (two in the case of a thin film), several waves, one for each interface, has to be taken into account constructively and destructively interfering. Following Parratt's formalism, the ratio between $\mathbf{R}_j$ and

$\mathbf{T}_j$ can be recursively written as

$$X_j = \frac{R_j}{T_j} = e^{-2ik_{i,z,j}z_j} \frac{r_{j,j+1} + X_{j+1}e^{2ik_{i,z,j}z_j}}{1 + r_{j,j+1}X_{j+1}e^{2ik_{i,z,j}z_j}}$$

where $r_{j,j+1} = \frac{k_{i,z,j}-k_{i,z,j+1}}{k_{i,z,j}+k_{i,z,j+1}}$. Set surrounding conditions are: normalized incident intensity $T_1 = 1$; no substrate reflection $R_{N+1} = 0$. This phenomenon gives rise to intensity oscillations in $\mathbf{Q}_z$ of the measured reflectivity that are called Kiessig fringes. The oscillation period is related to the film thickness via

$$d = \frac{2\pi}{\Delta \mathbf{Q}_z}$$

2.5.3 Beamline Instrumentation

ID03 is an undulator beamline dedicated to surfaces and interfaces structural characterizations. The beamline can be used for performing static surface crystallography studies or for studying processes at surfaces in real time.

The beamline has two experimental hutches where the actual experiments are performed. The first experimental hutch (EH1, Figure 2.11) hosts a z-axis vertical diffractometer on which users' chambers can be mounted. It is specially used to perform electrochemical experiments thanks to the system explained in Subsection 2.3 and using the specifically designed thin layer cell. The second (EH2) is equipped with a z-axis horizontal diffractometer, dedicated to Ultra-High-Vacuum studies. The sample can be cleaned (ion sputtering) and prepared (Knudsen and e-beam cells) in-situ; it can be heated up to 1300 K and cooled down to about 80 K.

EH1 diffractometer (Figure 2.12) is provided with an hexapode, keeping in the center of rotation the surface of the sample, that allow movements in x, y and z directions and tilting around x and y axis plus the tilting of the diffractometer itself along z. The Maxipix detector is fixed on the moving arm which has two rotational degree of freedom along gamma and delta that are rotations around respectively x and z axis.

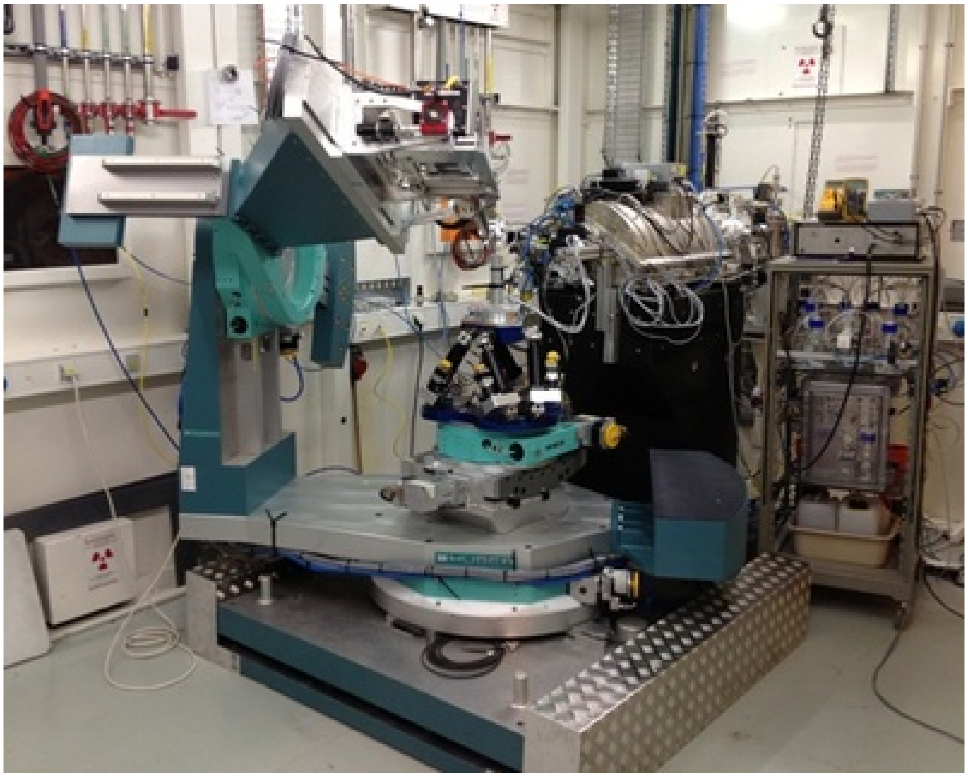

(a) EH1 with electrochemical system and TLE cell mounted on diffractometer.

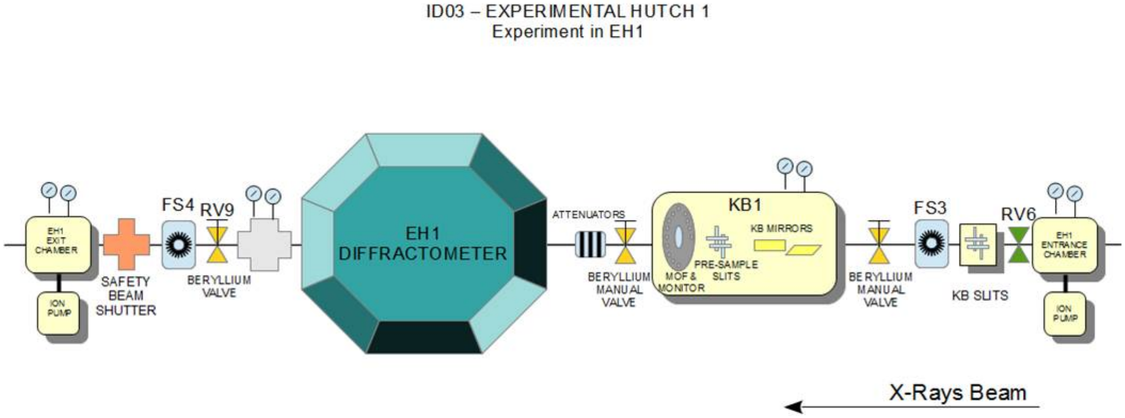
ID03 – EXPERIMENTAL HUTCH 1
Experiment in EH1
EH1 EXIT CHAMBER
ION PUMP
SAFETY BEAM SHUTTER
FS4
RV9
BERYLLIUM VALVE
EH1 DIFFRACTOMETER
ATTENUATORS
BERYLLIUM MANUAL VALVE
KB1
KB MIRRORS
PRE-SAMPLE SLITS
MOF & MONITOR
BERYLLIUM MANUAL VALVE
FS3
KB SLITS
RV6
EH1 ENTRANCE CHAMBER
ION PUMP
X-Rays Beam

(b) EH1's scheme.

Figure 2.11: Experimental hutch 1.

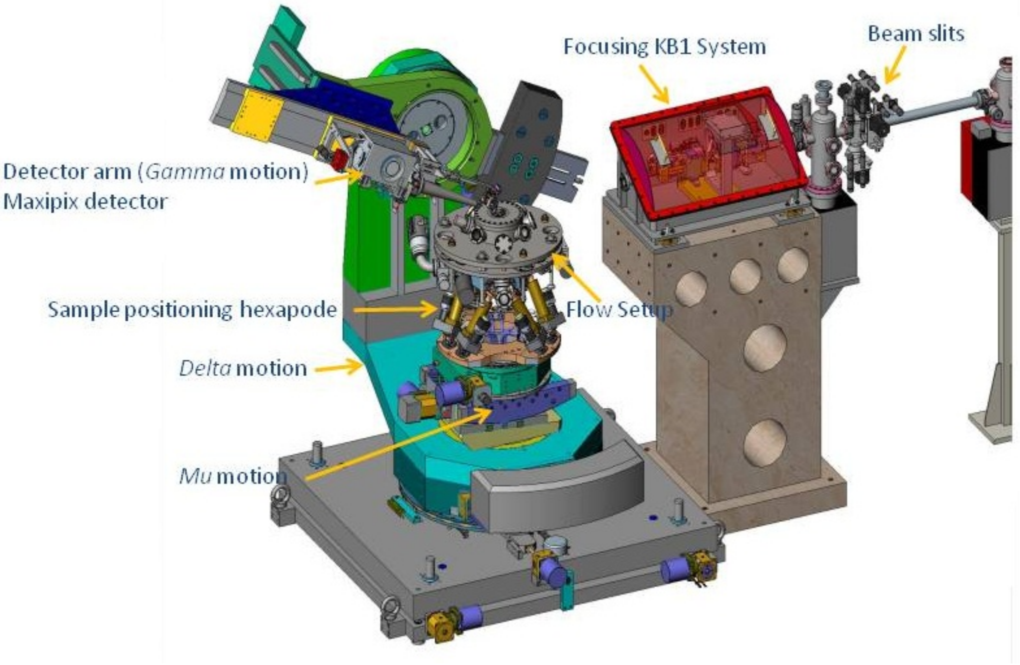
Focusing KB1 System
Beam slits
Detector arm (*Gamma* motion)
Maxipix detector
Sample positioning hexapode
Flow Setup
Delta motion
Mu motion

Figure 2.12: Diffractometer and hexapode scheme in experimental hutch 1.

Chapter 3

Results

3.1 Electrodeposition of chalcogenides on Ag(111)

Electrodeposition of chalcogenide thin films on metallic substrates has been extensively investigated in the past. Several works on ECALE growth of binary compounds on Ag and Au single crystal substrates are available in the literature. Deposition of sulfides is for sure the more widely investigated topic in this sense, nevertheless publications on selenides and tellurides can be found. However, only few structural studies have been performed on such kind of systems: in this direction CdS deposition on Ag single crystal surfaces has been object of a recent study[28]. In this paper the influence of crystallographic orientation of the substrates on the deposition conditions is discussed. Detailed studies about S UPD deposition have been also published by Loglio[25] and Aloisi[11] reporting the electrochemical behavior of Na_2S in ammonia buffer (Figure 3.1). Using in-situ STM experiments it was possible to relate the different electrochemical features visible during cyclic voltammetry (Figure 3.1) with different structure of the S UPD layer on the Ag(111) surface. According to Aloisi (Figure 3.1), the peak at -0.89 V (vs SCE) correspond to a full S coverage of the surface with a structure $(\sqrt{3}\times\sqrt{3})$R30º which then goes to a phase transition at more positive potentials rearranging in a $(\sqrt{7}\times\sqrt{7})$R19º structure. At potentials more negative than -1.23 V (vs SCE) only a partial coverage of the electrode surface with S is obtained. The charge transfer involved in the processes has been quantified as 130 ± 3 µC cm^{-2} for the formation of the incomplete layer and 185 ± 3 µCcm^{-2} for the deposition of the full monolayer.

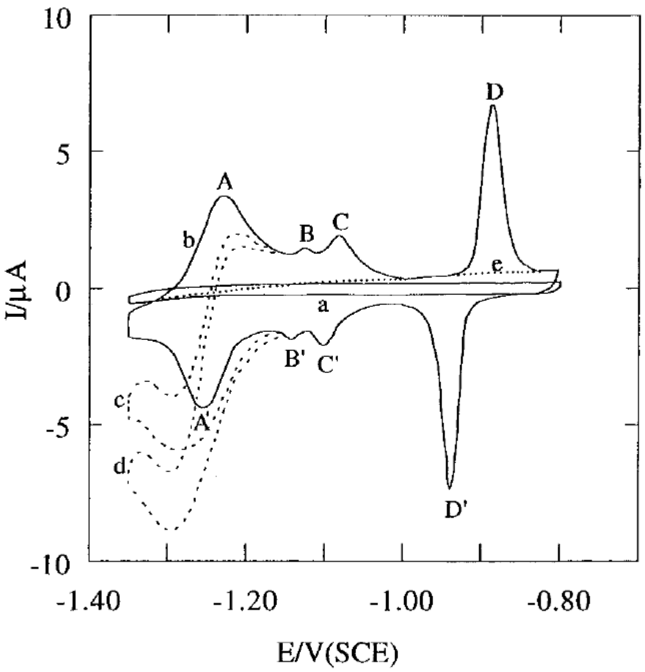

Figure 3.1: Sulfur oxidative underpotential deposition reported by Aloisi[11]. The curve b is a cyclic voltammetry of Ag(111) with 1 mM Na_2S in 0.1 M NaOH.

UPD of Se on Ag(111) has been investigated by Pezzatini[23]. In his work a detailed investigation of the behavior of Na_2SeO_3 in ammonia buffer is reported. As a matter of fact, Se electrochemical behavior is much more complex than S. In Figure 3.2 is shown a voltammetric study where is indicated that Se can be deposited by reduction of Se(IV) to Se(0) at potential of -0.5 V (vs SCE) in ammonia buffer while at potentials more negative than -0.8 V the Se(0) is stripped as Se(-II). The complexity of performing Se electrodeposition lays in the fact that, in presence of Se(-II), the Se(IV) can be also reduced to Se(0). For this reason the cathodic peak relative to the reduction of bulk Se(0) to Se(-II) integrates a bigger charge for voltammetric sweeps following the first one because a chemical reduction reaction is taking place at the same time of the electrochemical reduction. As explained before, this is due to the reduction of the Se(IV) to Se(0) by Se(-II) during the cathodic stripping of the bulk Se. On the other hand a peak relative to the stripping of a Se UPD monolayer is clearly visible at a potential in between the stripping of the bulk Se and the hydrogen discharge. The splitting between the bulk and the UPD stripping peaks makes possible to obtain Se UPD with an alternative method instead of direct reductive deposition. A Se UPD monolayer can be obtained in fact by depositing a bulk Se(0) film and then stripping the excess of Se leaving a Se monolayer on the surface. The process is optimized setting the potential at -1.0 V vs SCE for both deposition and dissolution of Se. In order to avoid chemical reduction of Se(IV) to Se(0) by Se(-II) it is necessary to exchange the Se solution with the buffer. This deposition method has been successfully used by Loglio et al.[24, 25] for the deposition of CdSe on Ag(111) by depositing a Se bulk film and then switching the potential to -0.9 V (vs Ag/AgCl sat KCl) for 60 seconds to remove bulk Se.

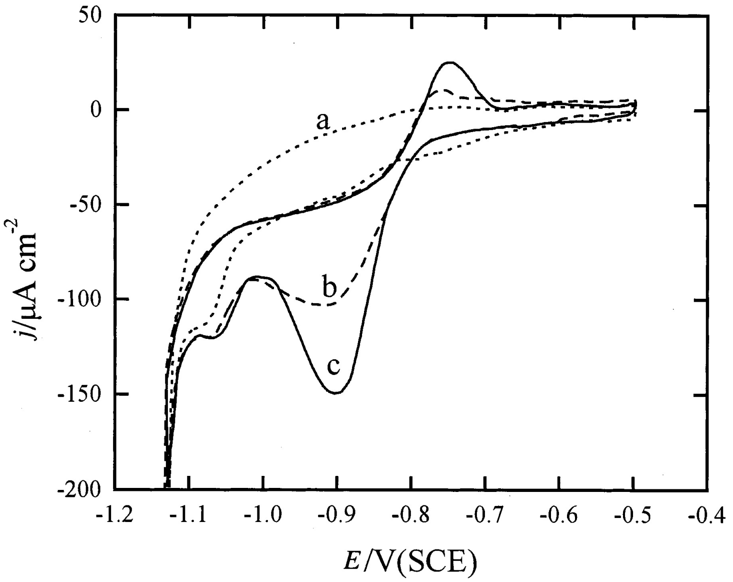

Figure 3.2: Figure 2 in Pezzatini's paper[23] on selenium reductive stripping. The curves a, b, c are consecutive cyclic voltammetries of Ag(111) with 0.5 mM Na_2SeO_3 in ammonia buffer.

Te UPD deposition on Ag(111) was investigated by Forni et al.[26] using a TeO_2 in ammonia buffer. Te on Ag(111) is underpotentially deposited at potential slightly more negative than -0.4 V (vs Ag/AgCl sat KCl), the oxidation of Te(0) to Te(IV) can not be observed as is taking place at potential where the oxidation of the Ag substrate takes place. As in the case of Se, a Te UPD monolayer can be formed by depositing a bulk Te film and then stripping the Te excess by applying a potential of -1.4 V (vs Ag/AgCl sat KCl). The stripping of the bulk Te has to be performed in a Te free solution to avoid the reduction of Te(IV) by Te(-II). The interaction between Te and Ag is so strong that, to remove UPD Te, the potential has to be set at -1.8 V (vs Ag/AgCl sat KCl). For these reasons to achieve the deposition of Te monolayer, it is a good practice to apply a potential of -1.4 V (vs Ag/AgCl sat KCl) after UPD growth to remove possible bulk Te.

3.1.1 Antimony electrodeposition

UPD electrodeposition of Sb based compounds on Au substrates was investigated in the past years by Stickney[4]. Electrodeposition of Sb was performed using a solution of 0.05 mM SbO_2^- at, 0.5 M Na_2SO_4 and 50 mM $Na_2B_2O_4$ buffered at pH 9.4.

In this condition it was possible to identify two UPD features by cyclic voltammetric analysis. The observed UPD peak brought them to choose a range between -0.4 and -0.75 V (vs Ag/AgCl) for the Sb underpotential deposition, leading to its optimization at -0.75 V (vs Ag/AgCl). In fact the deposition at potentials more negative than -0.8 V (vs Ag/AgCl) led to bulk growth. Furthermore, since the stripping peaks of bulk and UPD Sb are overlapping is difficult to use the oxidative bulk stripping method.

Yang et al.[20] reported the deposition of antimony both on platinum substrate and on tellurium film on Pt. It was performed with 0.05 mM Sb_2O_3 in 0.1 M $NaClO_4$ adjusted at pH 1.5 with $HClO_4$. On Pt substrate two reductive UPD peaks are visible: the one at more negative potential is integrating the majority of the charge involved in the process while the anodic stripping results in one single oxidative UPD peak. On Te the same test was repeated obtaining comparable results as the peaks are just few mV shifted.

Fernandez et al.[18] reported the co-deposition of Sb and Se using potassium antimonyl tartrate ($K_2Sb_2(C_4H_2O_6)_2$) in 0.4 M citric acid adjusted at pH 1.8. They set the deposition potential at different values (from -0.8 to -1.2 V vs SCE) performing deposition tests: eventually a thickness-vs-deposition-time analysis was performed for the -0.8 V vs SCE showing a 3-µm growth in 60 minutes.

3.1.2 Zinc electrodeposition

Zn chalcogenides have also been topic of several publications in the past[25] where the possibility of underpotentially deposit Zn both on S and on Se was investigated. ZnS deposition was performed reducing Zn from 0.5 mM $ZnSO_4$ in ammonia buffer, in this conditions is rather easy to identify the position of the UPD peak by cyclic voltammetric analysis. In the case of $ZnSe$ instead the deposition potential for Zn has to be set at more negative values, about -0.9 V (vs Ag/AgCl).

Pezzatini et al.[23] reported a specific analysis on Zn behavior on Se-covered surface. The results lead to the conclusion that the interaction between Zn and Se is very strong and the UPD process is favorite. Cyclic voltammetries, performed with 0.5 mM $ZnSO_4$ in ammonia buffer, showed that the process is surface limited and the deposition potential can be set in a range between -0.85 and -0.95 V vs SCE. Furthermore, they point out that a possible chalcogen deposition on Zn has to be performed at potential negative to -0.7 V (vs SCE), since for potentials more positive than this, Zn stripping takes place.

3.1.3 Multilayer deposition

Deposition of multilayer films with ECALE method is realized by the alternate underpotential deposition of the elements. The parameters to be used during the deposition process (optimal potential, deposition and rinsing time) are normally extracted from the cyclic voltammetric analysis performed on the deposition of the first monolayer of the compound. Growth rate and amount of deposited material after each cycle can be measured by stripping voltammetry. The integrated charge measured in the dissolution processes of the elements forming the film, gives an exact information on the stoichiometry of the compound and the average amount of material deposited during each cycle. This procedure has been normally used in the past to verify the linearity of the growth [23, 24, 25, 26]. Deposition parameters are normally constant during the whole deposition process. Nevertheless some publications report the opportunity to slightly change the deposition parameters to keep a constant growth rate during each cycle [19, 20, 21]. This was the case reported by Yang et al.[19, 20, 21] who observed a decrease in the deposited charge after the deposition of few monolayer of Sb and Te on Pt. This issue was solved by adjusting the deposition potentials for each cycles after the first until it was reached the "stable state" (condition where the deposition potential does not change anymore). This behavior was justified by the presence of a contact resistance at the interface with the electrode: as the film grows and it relaxes to his own structure, also this resistance changes decreasing until the steady state. This potential shift over several deposition cycles was observed also by Mathe et al.[27] in the case of CdSe growth. The explanation reported by the authors involves the presence of a space charge layer even though they admit that usually these features are micrometers-wide while the observed behavior lasts only few nm.

3.2 Deposition of Sb_2S_3

3.2.1 Ammonia buffer

Ammonia buffer solution have been widely used for UPD electrodeposition of sulfides on Ag single crystals[23, 24, 25, 26, 28]. The main advantages of working in this kind of environment are due to the stability of S^{2-} anions and the absence of specific adsorption of NH_4^+ and ClO_4^- ions at the electrode surface.

The quality of Ag(111) surfaces after chemical or physical preparation was checked by electrochemical means. For this purpose the shape of the cyclic voltammogram of Ag(111) in ammonia buffer was taken as reference. This measure is quite sensitive to surface and solution contaminations offering a good overview of the surface quality. Nevertheless surface physical imperfections like facets, step edges and miscuts are more difficult to identify as they do not contribute much to the capacity of the system. In this sense sulfur is a much better probe to verify the presence of physical defects[12, 13]. Hence after recording voltammogram of Ag(111) in ammonia buffer the features of the S UPD on Ag were also investigated. A typical cyclic voltammograms of the electrochemically cleaned Ag surface recorded in 0.1 mM Na_2S solution is shown in Figure 3.3. The anodic and cathodic peaks, respectively A and C in Figure 3.3, can be used as fingerprints for the presence of a well ordered S UPD layer. These features have been extensively investigated in the past and are due to a phase transition from $(\sqrt{3} \times \sqrt{3})$R30° to $(\sqrt{7} \times \sqrt{7})$R19.1° as reported by Aloisi et al.[11]. The small features visible at more negative potentials and only partially covered by the hydrogen discharge (A' and C') can be identified with the formation of a $(\sqrt{3} \times \sqrt{3})$R30° structure[11]. At more positive potential than -0.65 V the bulk deposition of S takes place (peak A2 in 3.4).

Deposition of Sb in ammonia buffer is a challenging task since the solubility of SbO_2^- is extremely low at this pH and local variation of pH might represent a serious problem for the repeatability of these experiment. In fact accumulation of OH^- ions can take place in proximity of the working electrode surface during the hydrogen discharge, despite the buffered environment. Moreover, due to the extremely low solubility of Sb_2O_3[14, 15, 16] even at a concentration of 25 µM solution it forms a white precipitate. For this reason, after the preparation, the solution was left resting until the excess of solute was deposited on the bottom of the reservoir before using in our electrochemical apparatus. The final concentration used in the

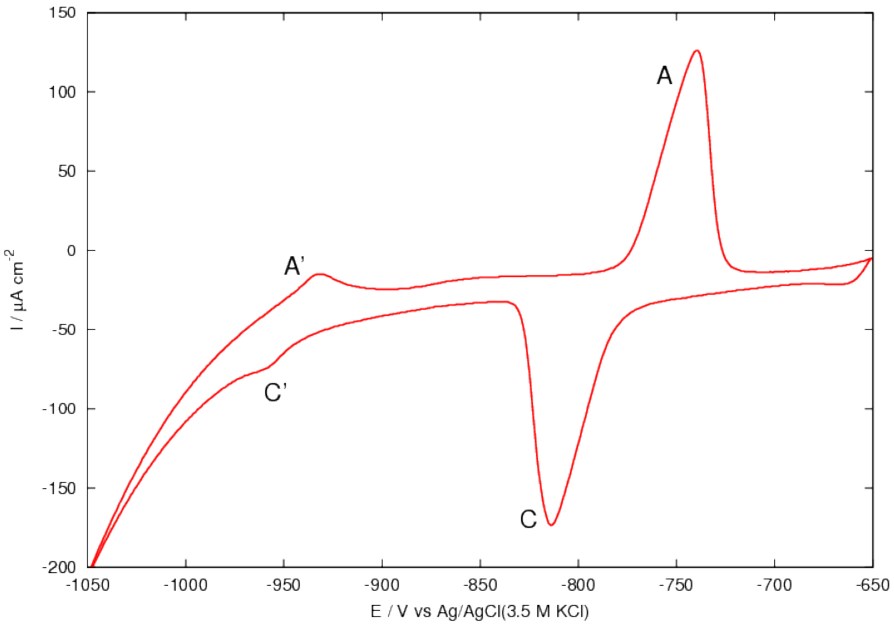

Figure 3.3: Cyclic voltammetry of Ag(111) in 0.5 mM Na_2S buffered with ammonia buffer. Scan rate: 50 mV s^{-1}.

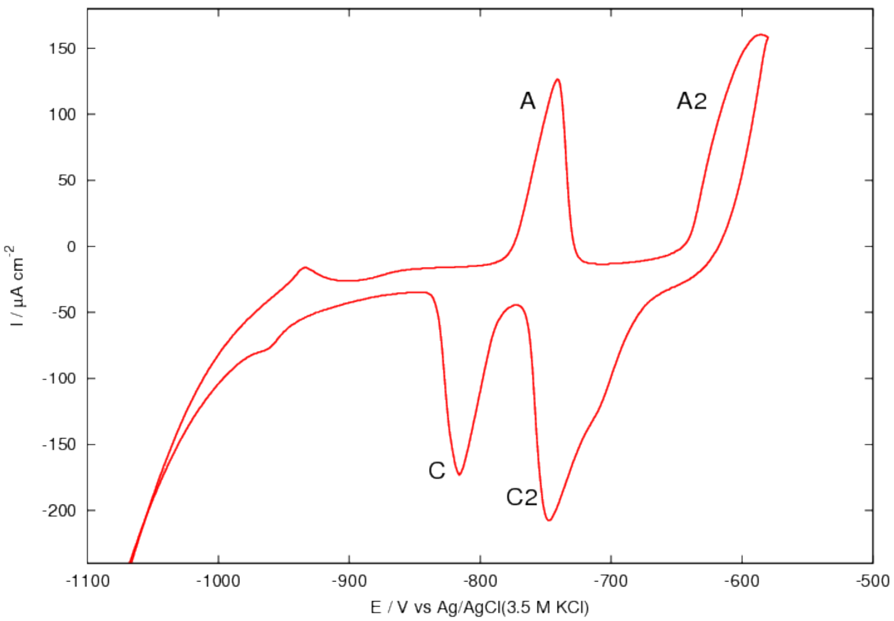

Figure 3.4: Cyclic voltammetry of Ag(111) in 0.5 mM Na_2S buffered with ammonia buffer. Scan rate: 50 mV s^{-1}.

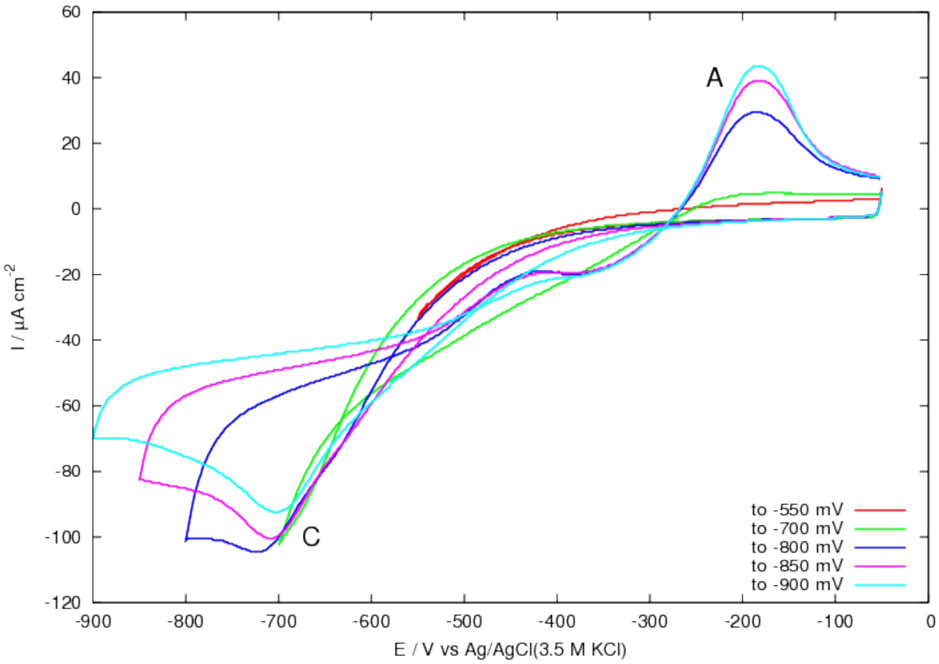

Figure 3.5: Cyclic voltammetry of Ag(111) in 0.05 mM Sb_2O_3 buffered with ammonia buffer. Scan rate: 50 mV s^{-1}.

deposition experiments was extrapolated from the data published by Gayer et al.[14] and quantified in about 3 µM of Sb_2O_3.

Sb behavior on Ag is reported in Figure 3.5: after flushing the solution in cell, cyclic voltammetries to increasingly negative potentials are performed to evaluate when some charge starts to deposit. In the experiments there is no evidence of the presence of an UPD peak or surface limited reactions. The possibility of depositing Sb bulk and then stripping the excess to leave only the UPD on the surface can not be pursued as also oxidative peak A does not show surface limited features.

The presence of the Sb UPD deposition process on the S covered Ag(111) surface was investigated in a series of potential step experiments, each experiment included the following steps:

- deposition of S UPD monolayer at -0.65 V for 60 seconds
- wash with ammonia buffer
- potential step to -0.1 V
- exchange of the buffer solution with the Sb containing solution

- potential step to the deposition potential for a given deposition time
- stripping of the Sb
- repeat potential step deposition and stripping experiments with different potential and deposition time

Results of the test are shown in Figure 3.6 where several attempts to deposit Sb are reported. The deposition process starts to take place at potentials more negative than -0.58 V and not much of a difference in the integrated charge of the anodic peak is measured between the 60 and the 120 seconds deposition attempts. This is due to the fact that the kinetic of the deposition process is extremely slow at this extremely low concentration of Sb. Nevertheless it was verified that deposition at -0.65 V for time much longer than 120 seconds leads to the charge integrated from the stripping curve is not increasing. This means that the deposition process in these conditions leads the maximum coverage of Sb on the electrode surface.

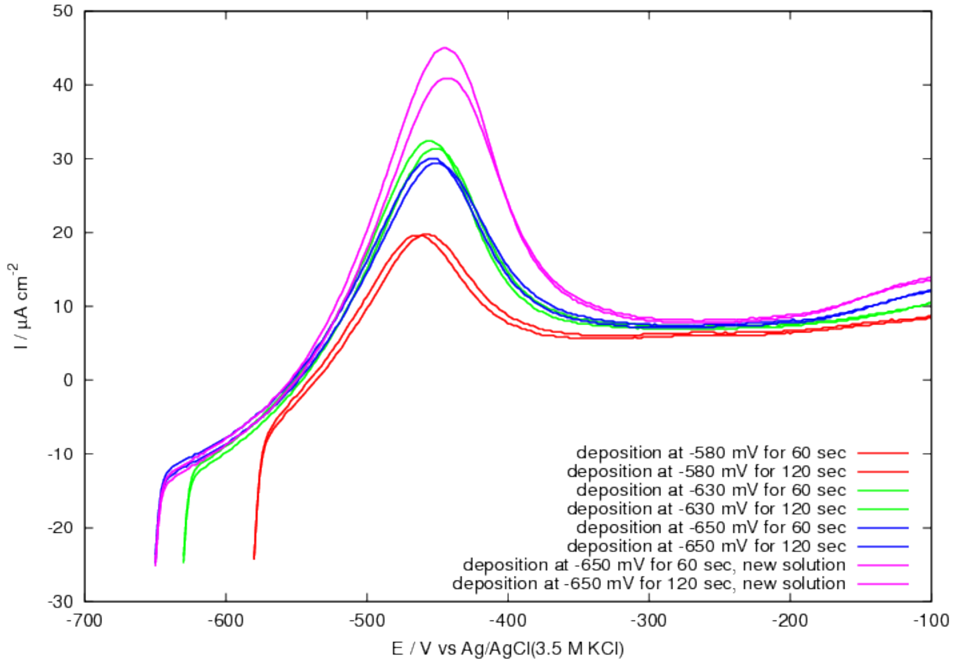

Figure 3.6: Stripping voltammetries of S/Ag(111) in 0.05 mM Sb_2O_3 buffered with ammonia buffer. They were obtained depositing Sb on S/Ag(111) at -0.65, -0.63 and -0.58 V and then scanning the potential. For each test two voltammetries were performed using different deposition times (60 and 120 seconds). For the -0.65 V deposition potential, both voltammetries were performed again after depositing Sb in a fresh solution. Scan rate: 50 mV s^{-1}.

It is worth to notice that, if the deposition test is repeated after exchanging the Sb solution in the cell, the charge involved in the stripping process is significantly higher. The poor reproducibility of the Sb deposition process in ammonia buffer can not ensure good operative conditions for the multilayer deposition process according to the ECALE method, for this reason different buffer solutions have been investigated.

3.2.2 NaOH

Solubility of Sb_2O_3 has a minimum at pH 3 while in extremely basic environment becomes higher [14]. For this reason a pH 13 solution of NaOH was chosen to perform further UPD deposition of Sb. A 34 µM solution of Sb_2O_3 in 0.1 M NaOH was used for the deposition tests. The first sulfur UPD layer was deposited from an ammonia buffer solution as discussed in the previous paragraph. Several stripping voltammetries were recorded to verify the presence and the position of the Sb cathodic UPD peak, which finally was identified at -0.95 V (see Figure 3.7). The formation of the Sb UPD monolayer of the S covered Ag(111) surface was investigated using different deposition time in order to establish the presence of a surface limited deposition process. In the stripping curves reported in Figure 3.7 two peaks indicated as A and A2 are visible (respectively at -0.62 V and -0.41 V). The A2 peak can be associated with a surface limited deposition process as the charge associated with this process is not changing for deposition time longer than 30 seconds. On the other hand the behavior of peak A can not be fully explained as the charge related with this process is decreasing with the increasing of the deposition time. Moreover some reproducibility problems of the deposition process are observed. Due to the very low concentration of Sb, it is necessary to flush the solution before each measure in order to keep constant the Sb concentration and even so this does not seem enough to achieve consistent results in equivalent tests.

A possible reason for the unusual behavior of the system can be ascribed to the use of two different buffers for the deposition of S and Sb. The deposition tests were thus repeated using a 0.1 M NaOH solution for the S deposition. Indeed cyclic voltammetries of S on Ag(111) show slightly different features and deposition potential due to the pH shift. As reported in Figure 3.8 the deposition peak is shifted from -0.73 V (ammonia buffer) to -0.83 V due to the higher basicity of the solution. Additional features of the S UPD deposition process are better visible at negative potentials due to the shift of the hydrogen evolution.

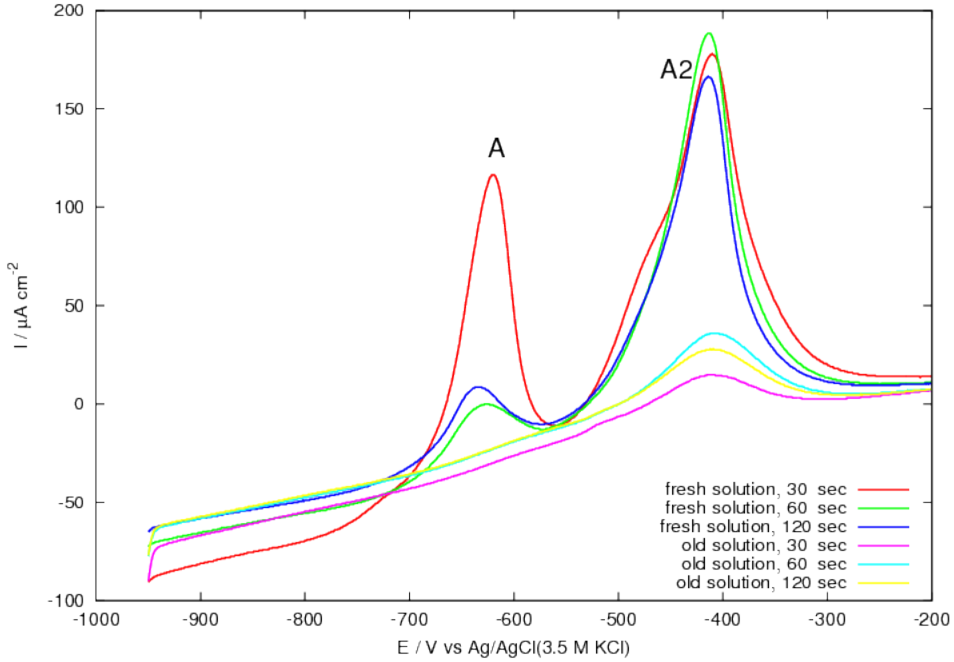

Figure 3.7: Stripping voltammetries of Sb/Ag(111) in NaOH solution after the deposition of Sb at -0.95 V for different periods of time. Scan rate: 50 mV s^{-1}.

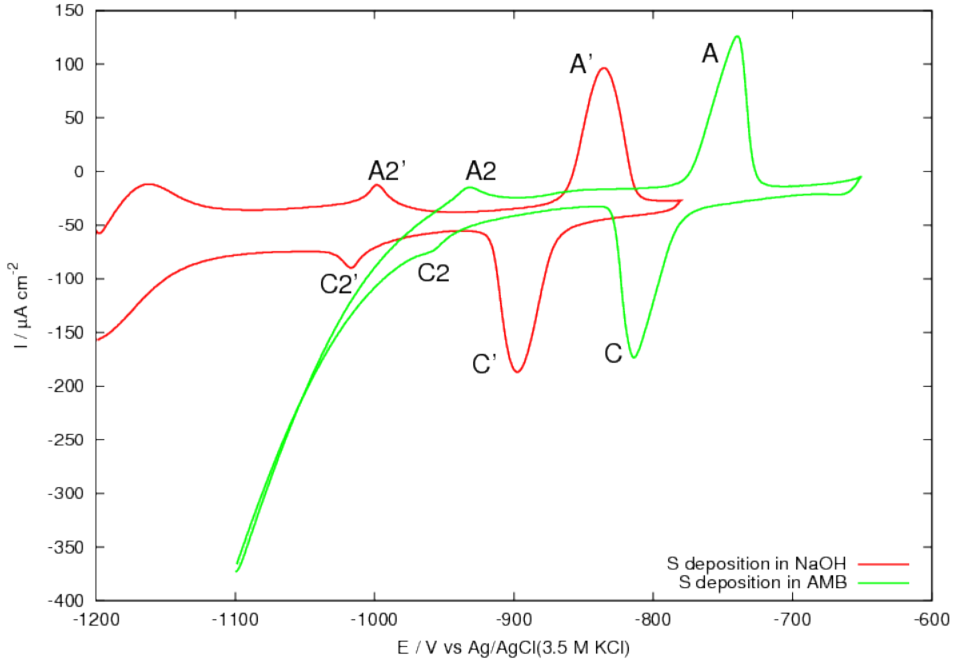

Figure 3.8: Cyclic voltammetries of Ag(111) in 0.5 mM Na_2S buffered with ammonia buffer (green) and in NaOH solution (red). Scan rate: 50 mV s^{-1}.

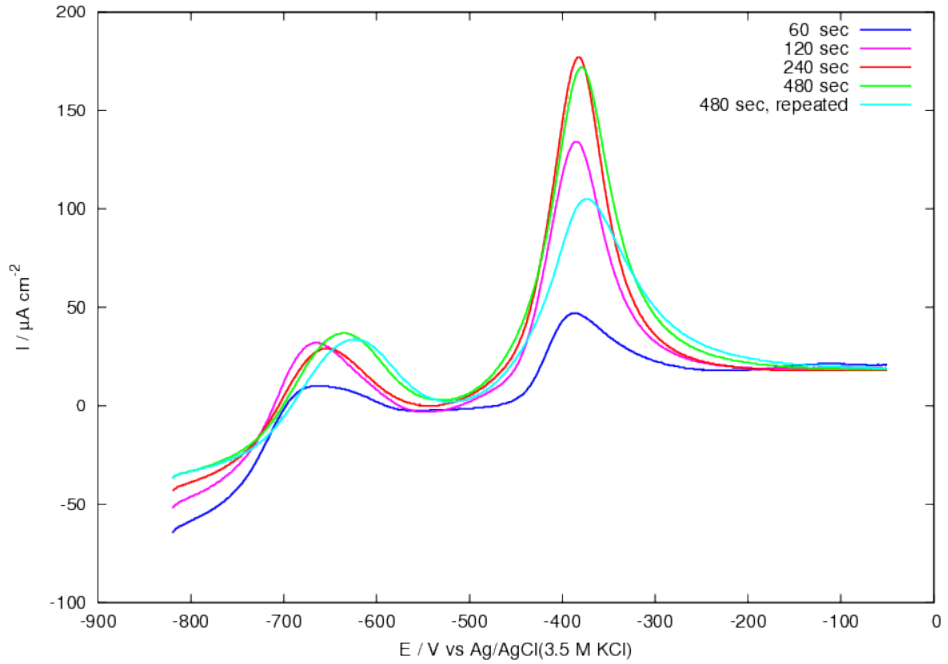

(a) Deposition times examined are 60, 120, 240 and 480 seconds. The last test was repeated in order to see that the system is not stable in time.

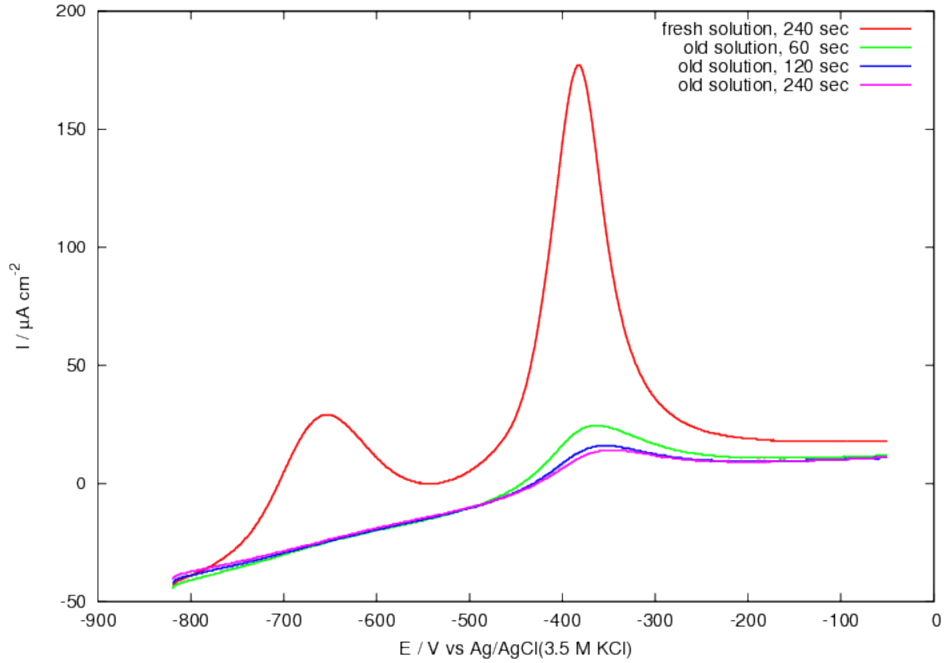

(b) The red stripping voltammetry is taken by Figure 3.9a. The repetitions are made following the same parameters of Figure 3.9a.

Figure 3.9: Stripping voltammetries of Sb/S/Ag(111) in NaOH solution after the deposition of Sb at -0.82 V for different periods of time. Scan rate: 50 mV s^{-1}.

As S was deposited, other tests on Sb were necessary to check the possibility of growing Sb on S/Ag(111). In order to identify the Sb UPD deposition peak and select the right deposition potential, the behavior of Sb was investigated by stripping voltammetry. Then Sb was deposited at -0.82 V for different periods of time and, for each one, a stripping voltammetry was performed: a saturation in the integrated charge can be noticed after 240 seconds. By this test seems that the Sb deposition is a surface limited phenomenon, nevertheless after repeating the measure conflicting results were found as shown in Figure 3.9a. The last stripping voltammetry (light blue) should show the same integrated charge of the previous one: in fact the latter subtended area is lower than his equivalent measurement. To be sure that this behavior was a real decreasing trend of the integrated charge, other tests were performed and it was clear from the Figure 3.9b that after the first solution flush, the conditions change and the results are no comparable anymore.

As a matter of facts the use of Sb_2O_3 seems to present several issues related with the reproducibility of the deposition process.

3.2.3 Acetic buffer

The use of a different salt as source of Sb for the deposition process was considered in order to avoid solubility problems. Unfortunately not too many water-soluble Sb salts are available, for this reason we considered the use of an antimony complex. Our choice was the potassium antimonyl tartrate ($K_2Sb_2(C_4H_2O_6)_2$). This complex is rather stable in acidic environment but tends to go into hydrolysis at pH higher than 7, the result is that in ammonia buffer the insoluble antimony oxide is precipitated in few minutes after the preparation of the solution. Despite it is more convenient using the same buffer for all solutions, sulfur can not be dissolved in buffers with pH lower than 8 in order to avoid the formation of gaseous HS. Nevertheless the use of acetic buffer at pH 4.7 has been successfully used for the ECALE deposition of PbS on Ag(111)[17]. Deposition tests were carried out using a 1 mM Na_2S solution in ammonia buffer and a 0.5 mM $K_2Sb_2(C_4H_2O_6)_2$ solution in acetic buffer.

While two oxidative peaks (A and A2) are visible in Figure 3.10 (possibly bulk and UPD) it was not possible to identify any UPD deposition peak because only one broad cathodic peak is visible (C). Nevertheless the Sb UPD deposition can be achieved by the deposition of bulk Sb followed by an anodic stripping which leaves intact the Sb UPD layer on the electrode.

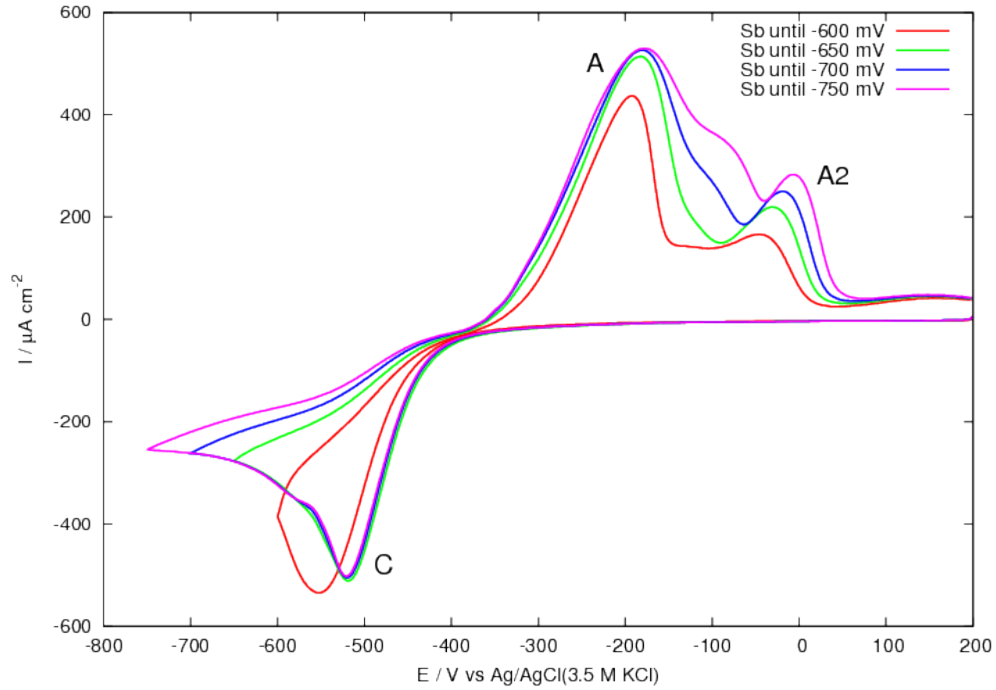

Figure 3.10: Cyclic voltammetries of Ag(111) in 0.5 mM $K_2Sb_2(C_4H_2O_6)_2$ buffered with acetic buffer. Used potential were -0.6, -0.65, -0.7 and -0.75 V. Scan rate: 50 mV s^{-1}.

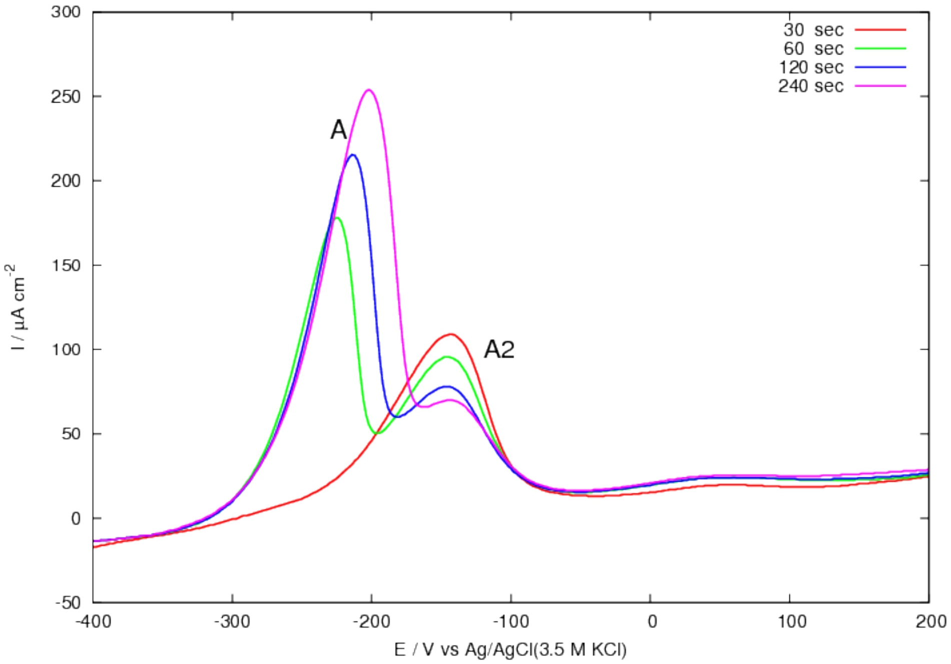

Figure 3.11: Stripping voltammetries of Sb/Ag(111) in acetic buffer. They were obtained depositing Sb from 0.5 mM $K_2Sb_2(C_4H_2O_6)_2$ solution on Ag(111) at -0.4 V for 30, 60, 120 and 240 seconds and then scanning the potential. Scan rate: 50 mV s^{-1}.

To achieve this result it is mandatory to find the exact potential where only the bulk is stripped. In Figure 3.11 four stripping voltammetries are shown: Sb was deposited at -0.4 V using different deposition time in order to identify the conditions to form a complete UPD-plus-bulk layer. It is observed that the amount of deposited bulk Sb increases (peak A) while the supposed UPD peak (A2) remains nearly the same. From this test the stripping potential for the bulk Sb can be identified in a window between -0.3 and -0.35 V.

The next step was therefore the optimization of the bulk-stripping potential. Stripping attempts were made positively increasing the potential from -0.3 to -0.33 V in order to identify correct conditions for stripping the Sb bulk leaving unaltered the UPD layer underneath. The stripping tests were repeated increasing the stripping time from 30 to 240 seconds. It was found that -0.33 V is too negative to adequately strip the bulk and up to 240 seconds are needed to remove nearly all the bulk. On the other hand -0.3 V seems to be too positive and also part of the UPD layer was removed even after 30 seconds. The results of the tests, reported in Figure 3.12, show that best depositions were obtained applying -0.32 V for 60 seconds.

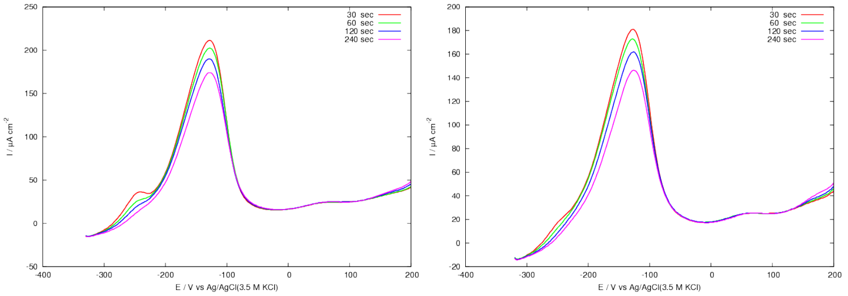

(a) Bulk stripping potential set at -0.33 V.

(b) Bulk stripping potential set at -0.32 V.

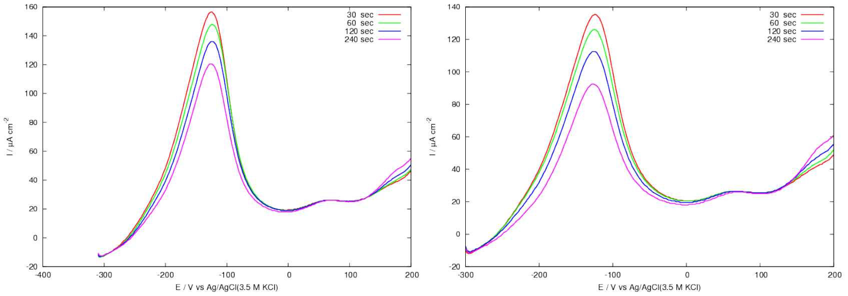

(c) Bulk stripping potential set at -0.31 V.

(d) Bulk stripping potential set at -0.3 V.

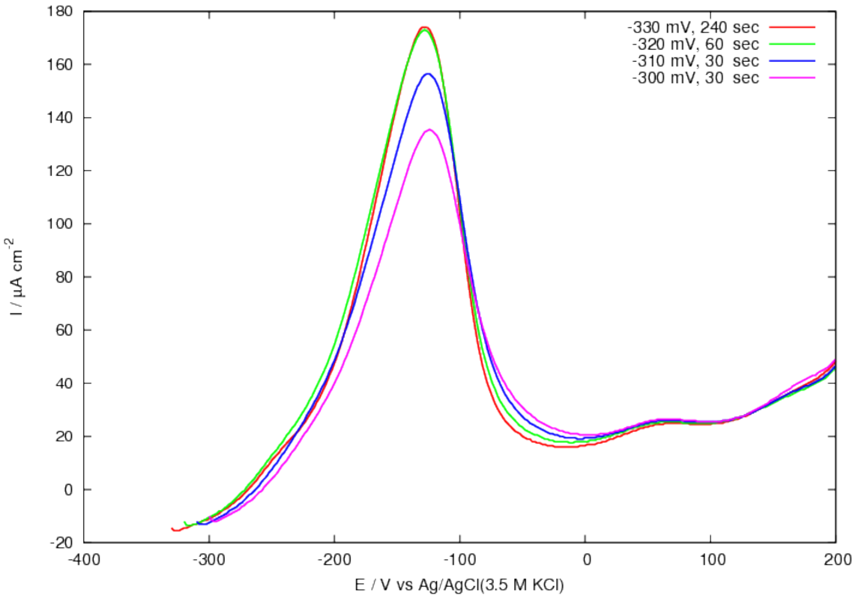

(e) Summary of the best stripping time period for each stripping potential.

Figure 3.12: Stripping voltammetries of Sb/Ag(111) in acetic buffer. They were obtained depositing Sb from 0.5 mM $K_2Sb_2(C_4H_2O_6)_2$ solution on Ag(111) at -0.4 V for 60 seconds, stripping bulk at different potentials for different time periods (30, 60, 120 and 240 seconds) and then scanning potential. Scan rate: 50 mV s^{-1}.

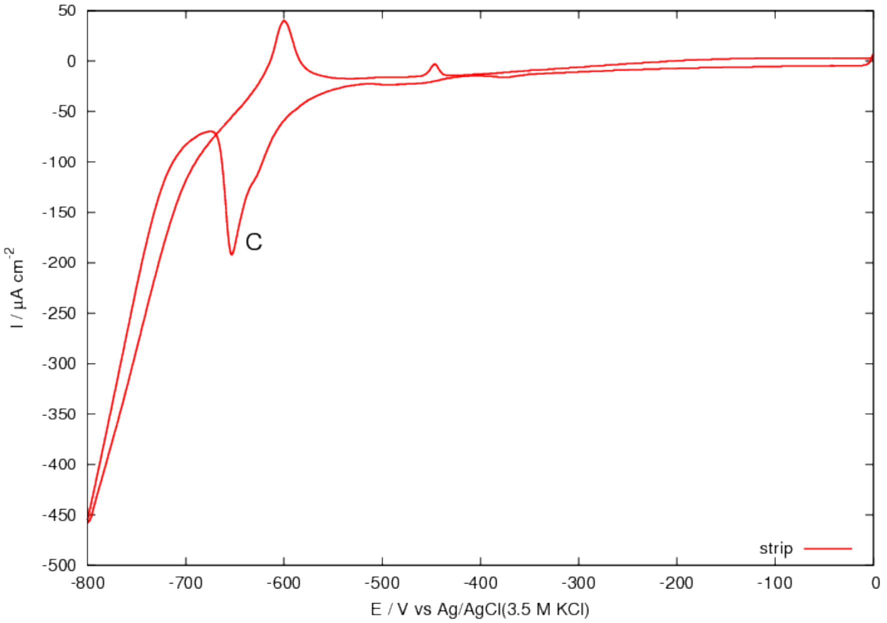

Figure 3.13: Cyclic voltammetry of S/Ag(111) in acetic buffer. It was obtained depositing S from Na_2S solution in ammonia buffer on Ag(111), flushing the acetic buffer and then scanning the potential. Scan rate: 50 mV s^{-1}.

It has to be taken in account that S UPD layer deposited in ammonia buffer can be altered by the presence of the lower pH acetic buffer. In order to find a potential window where the S UPD layer is stable in presence of the acetic buffer, the stability of the S UPD monolayer was tested. In Figure 3.13 is shown the cyclic voltammetry of S/Ag(111) while the acetic buffer is in the cell. The cathodic peak indicated as C is relative to the S stripping, thus the S UPD layer is stable on Ag(111) up to approximately -0.52 V, as reported by Fernandes et al.[17].

During the layer by layer growth it is necessary to exchange the solution from the acetic to the ammonia buffer after the deposition of each UPD monolayer: for this reason the stability of Sb in ammonia buffer might present some issues. This hypothesis turned out to be true since it is clear from Figure 3.14a that Sb is not stable at potential more positive than -0.51 V in ammonia buffer. The optimal potential for keeping the Sb UPD layer intact should be even more negative than -0.51 V but this is not compatible with the presence of S which is stripped at potential more negative than -0.52 V. As shown in Figure 3.14b, after flushing the cell with both buffers (acetic and ammonia) at -0.52 V the integrated charge of the Sb oxidative peak is greater but on the other hand the integrated charge of S reductive peak is significantly decreased compared to the ideal situation of washing the cell at -0.4 V. Following these results the best compromise for the buffer exchange potential is -0.51 V.

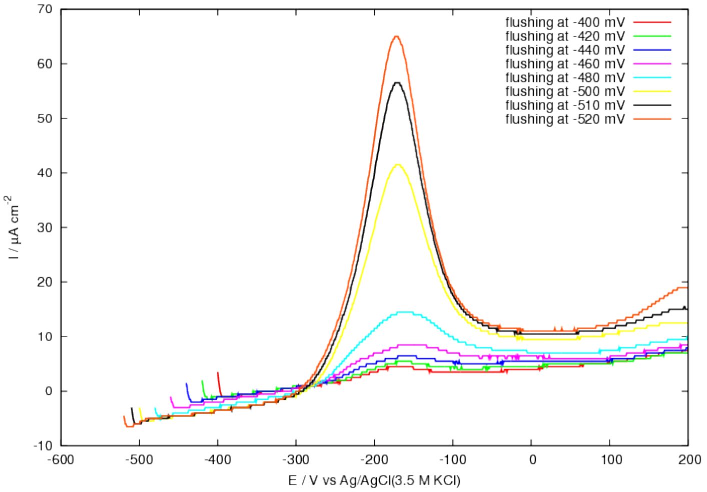

(a) Stripping voltammetries of Sb on S/Ag(111) in acetic buffer. They were obtained depositing Sb from 0.5 mM $K_2Sb_2(C_4H_2O_6)_2$ solution on S/Ag(111), flushing the ammonia buffer at different potentials and then, again in acetic buffer, scanning potential.

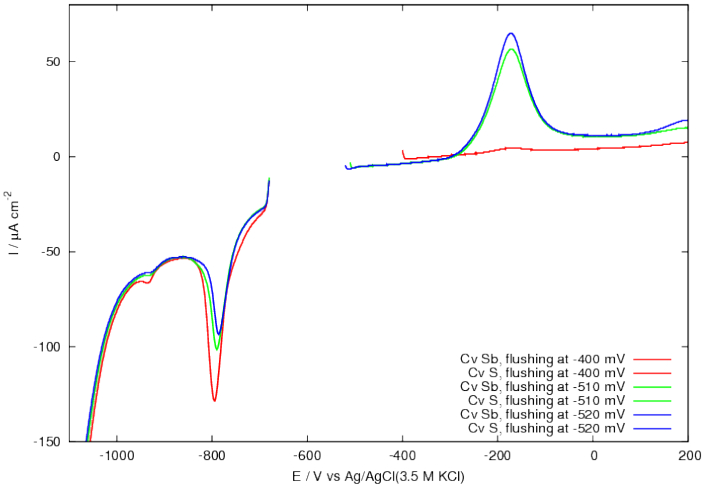

(b) Stripping voltammetries of Sb/S/Ag(111) in acetic buffer and S/Ag(111) in ammonia buffer. Sb voltammetries are the same of Figure 3.14a; S voltammetries were obtained scanning the potential after stripping Sb.

Figure 3.14: Stripping voltammetries' results of the exchange buffer test. Scan rate: 50 mV s^{-1}.

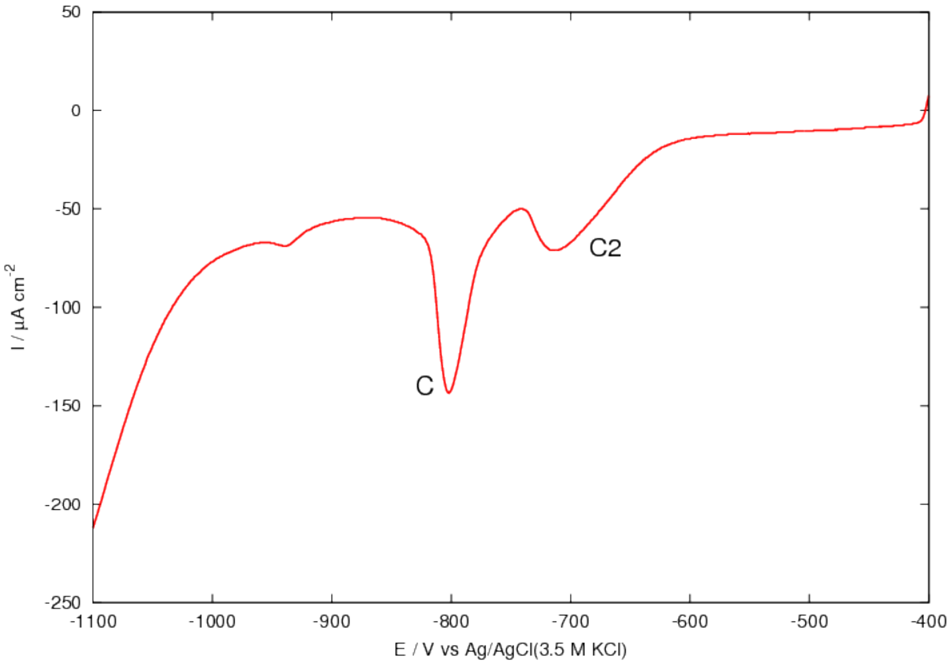

Figure 3.15: Stripping voltammetry of S/Sb/S/Ag(111) in ammonia buffer after the stripping of Sb. It was obtained depositing the second S layer at -0.68 V on Sb/S/Ag(111), oxidatively stripping Sb and then scanning the potential. Scan rate: 50 mV s^{-1}.

In order to identify the correct conditions for the multilayer growth some deposition tests of S on Sb/S/Ag(111) were carried out. The results of an attempt of depositing S on Sb/S/Ag(111) at a potential of -0.68 V are reported in Figure 3.15: according to the integrated charge from peak C2 it looks like only a very little amount of S is deposited on the substrate. This is not completely surprising if we take in account the fact that the S-Sb and S-Ag interactions can be largely different. Moreover, this behavior can be explained considering that a semiconductor material is deposited on the electrode surface and for this reason the system has an additional resistivity which might hinder the charge transfer and shift the deposition potential.

A similar behavior was described by Gao et al.[19], in this paper was used a trial and error process in order to identify the optimal conditions of the applied potential for the S UPD deposition. In our case we verified the deposition conditions at three different deposition potentials: -0.65, -0.64 and -0.63 V. For each of them the deposition was repeated using different times (60, 120 and 240 seconds) to reveal if the deposition of a full S monolayer was achieved. In the first tests (Figures 3.16a and 3.16b) it can be seen that the stripping charge of the bulk peak continues to increase: this is not due to the deposition of a bulk layer but because the applied potential was not positive enough to complete the deposition in that range of time.

The deposition of a full S layer is reached at -0.630 V where after 60 seconds a full monolayer is deposited. Looking at the plot in Figure 3.16c, two cathodic peaks are visible: the C is the classic UPD one and it is related to the very first S layer of our sample while peak indicated as C2 is found at the position of the bulk. This is because after the stripping of Sb a sulfur multilayer is present on the surface.

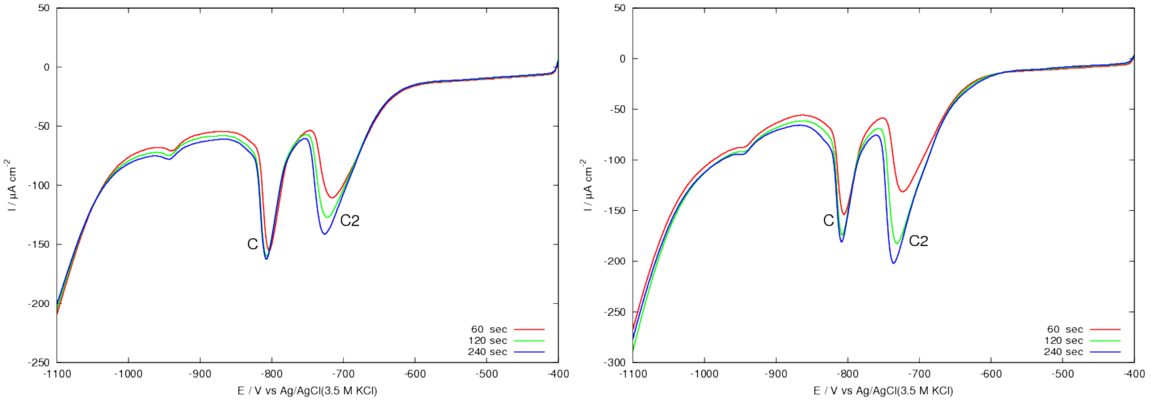

(a) Deposition potential of second S layer: -0.65 V.

(b) Deposition potential of second S layer: -0.64 V.

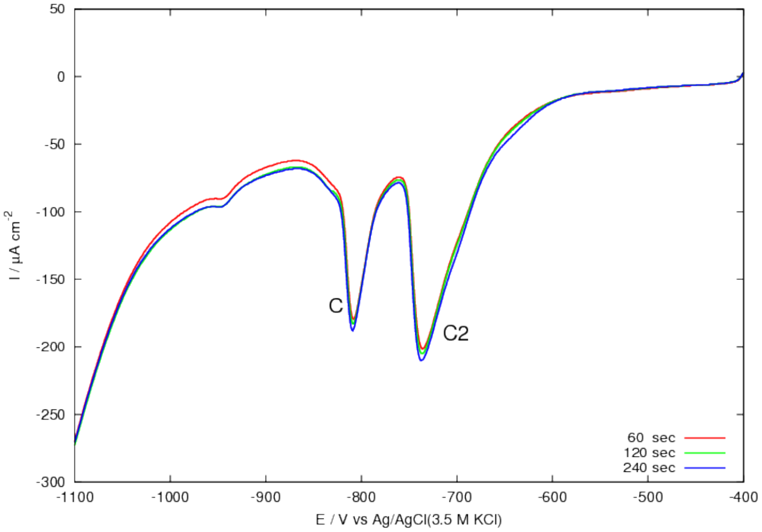

(c) Deposition potential of second S layer: -0.63 V.

Figure 3.16: Stripping voltammetries of S/Sb/S/Ag(111) in ammonia buffer after the stripping of Sb. They were obtained depositing the second S layer at different potentials on Sb/S/Ag(111), oxidatively stripping Sb and then scanning the potential. Scan rate: 50 mV s^{-1}.

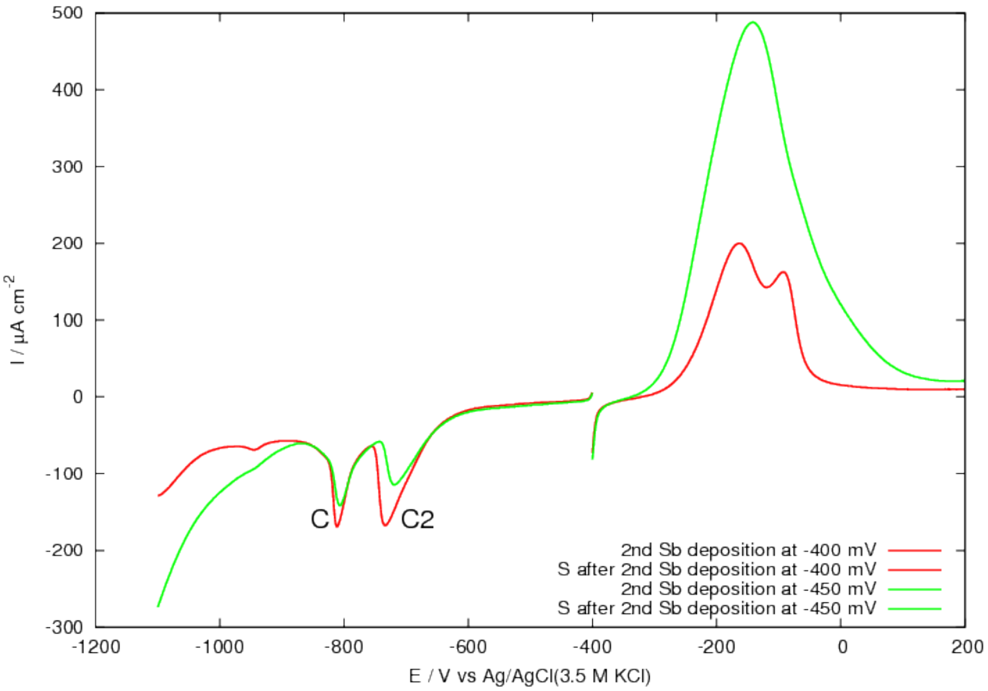

Figure 3.17: Stripping voltammetries of $[Sb/S]_2$/Ag(111) in ammonia buffer (S) and in acetic buffer (Sb). Sb voltammetries were performed first while S voltammetries were performed only after the complete stripping of Sb. Scan rate: 50 mV s^{-1}.

Once fixed the parameters for S deposition another Sb layer was deposited to check if the first layer deposition potential can be used again or if, like with sulfur, a shift has to be applied. In Figure 3.17 are shown the stripping voltammetries after a deposition at -0.4 V (red) and -0.45 V (green) and both bulk-stripped at -0.32 V for 60 seconds. It appears by the value of the integrated charge that the amount of Sb deposited does not correspond to a full monolayer. As a consequence of this, it appears that the potential for the Sb deposition has to be shifted (in this case towards more negative values). It is worth to notice that the integrated charge of the C2 peak in the S stripping voltammetry should be equal in the two cases. In fact the charge involved in the process is smaller when more Sb is deposited on S: the cause is not completely clear but, since the previous tests prove that S is well deposited, it seems likely that the Sb deposition itself somehow damages the layer below. Actually the charge stripped in the peak C2 should be comparable with the one of peak C1 and this happens more in the voltammetry after the -0.45 V deposition (green) rather than in the other one.

A very important test is to check if the peak observed is really an UPD: according

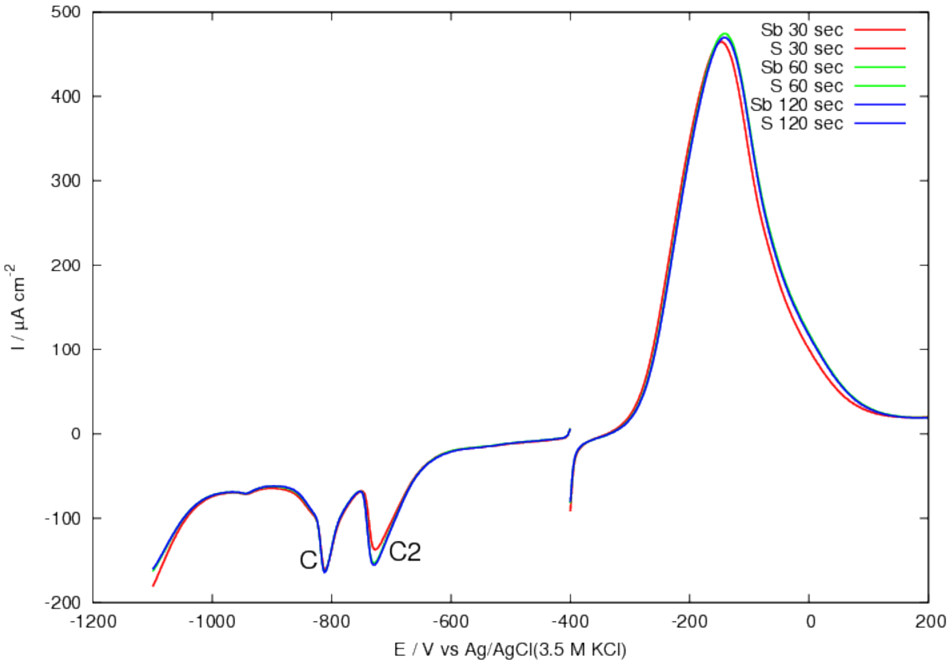

Figure 3.18: Stripping voltammetries of $[Sb/S]_2$/Ag(111) in ammonia buffer (S) and in acetic buffer (Sb). Sb voltammetries were performed first and S voltammetries were performed only after the complete stripping of Sb. The voltammetries were performed after Sb depositions for different times: 30 (red), 60 (green) and 120 seconds (blue). Scan rate: 50 mV s^{-1}.

to the usual strategy it is necessary to perform depositions for different periods of time in order to see possible changes of the peaks. As visible in Figure 3.18, the peak remains the same during this test and it can be concluded that the reaction is surface limited.

The deposition process of Sb on S was also investigated. It was noticed the presence of a little bump in the cathodic peak of Sb so it was set the potential right on that value at -0.32 V and actually, as visible in Figure 3.19, it was confirmed to be an UPD process.

In order to achieve the growth of a multilayer of Sb_2S_3 also the further layers deposition has to be tested. As seen in the previous tests, in general same settings can not be applied for the all layers of the stack. In fact this new layer seemed to follow nearly well the parameters which have already been used.

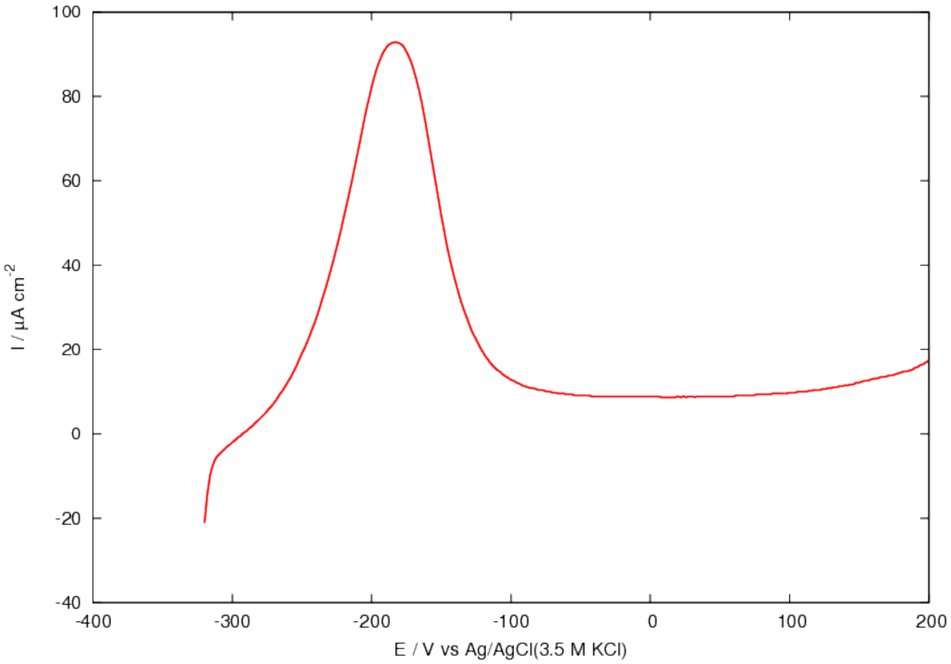

Figure 3.19: Stripping voltammetry of Sb/S/Ag(111) in acetic buffer. It was obtained depositing Sb on S/Ag(111) at -0.32 V and then scanning the potential. Scan rate: 50 mV s^{-1}.

In order to achieve the growth of a multilayer of Sb_2S_3 also the further layers deposition has to be tested. As seen in the previous tests, in general same settings can not be applied for the all layers of the stack. In fact this new layer seemed to follow nearly well the parameters which have already been used.

The green voltammetries in Figure 3.20 show the stripping of S and Sb after the deposition of $S/[Sb/S]_2$ on Ag(111). It can be seen the increase of deposited charge for the sulfur every time a new layer was deposited, but at the same time it is clear that the charge associated with the Sb stripping decreases. This is the same phenomenon observed for the S: when a new layer is deposited, the one below is modified and loses a part of charge. As the third sulfur deposition is confirmed by this test, it can be concluded that this parameters setting produce the growth of a $S/[Sb/S]_2$ sample.

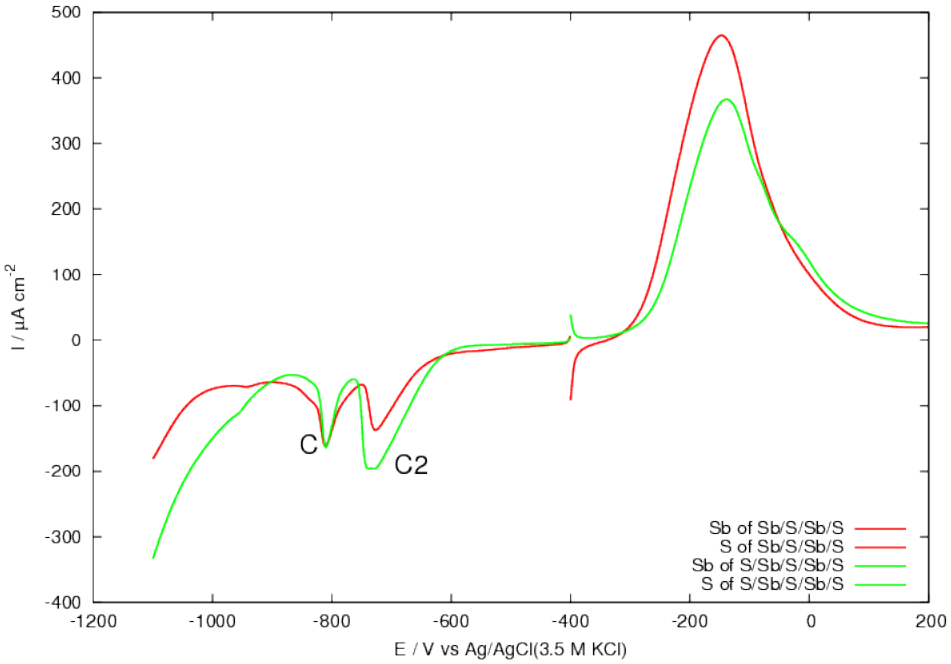

Figure 3.20: Stripping voltammetries of $S/[Sb/S]_2$/Ag(111) in ammonia buffer (S) and in acetic buffer (Sb). Sb voltammetries were performed first and S voltammetries were performed only after the complete stripping of Sb. The red series is the green one in Figure 3.17. Scan rate: 50 mV s^{-1}.

3.2.3.1 Multilayer

From the previous tests it seemed that layers after the first were deposited always with the same potential conditions and an attempt of Sb/S multilayer deposition was done. The results obtained in the stripping curves (Figure 3.21) although were conflicting. On one side it is visible the charge of the C2 peak (S stripping) increasing every new cycle while on the other the Sb peaks remain nearly the same. Actually the charges integrated by the three Sb peaks are increasing but it is not due to the peak at -0.18 V (A): close to it, other broader sub-peaks were growing and this means that what was deposited from the third layer on, was not only UPD Sb.

This behavior was unexpected as no more underpotentially-deposited Sb is deposited after first two cycles while S integrated charge continues to increase. The main theory for this behavior is related to the complex structure of the Sb_2S_3 unit cell (Figure 3.22) that can not be grown just with a layer by layer deposition. After first cycles, deposited S atoms relax under the last Sb layer allowing atoms under-

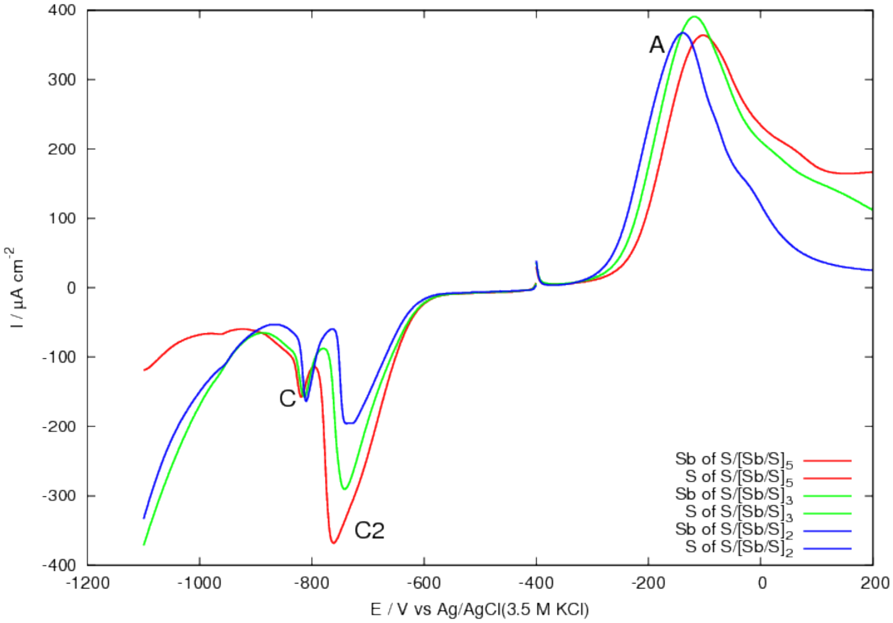

Figure 3.21: Stripping voltammetries of $[Sb/S]$ multilayers on Ag(111) in ammonia buffer (S) and in acetic buffer (Sb). Sb voltammetries were performed first and S voltammetries were performed only after the complete stripping of Sb. The blue series is the green one in Figure 3.20; the green one was performed after the deposition of $S/[Sb/S]_3$; the red one was performed after the deposition of $S/[Sb/S]_5$. Scan rate: 50 mV s^{-1}.

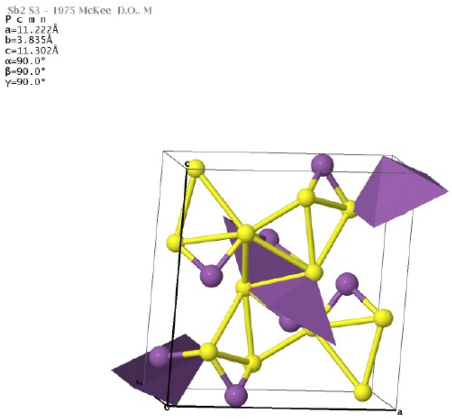
Sb2 S3 - 1975 McKee D.O.. M
P c m n
a=11.222Å
b=3.835Å
c=11.302Å
α=90.0°
β=90.0°
γ=90.0°
c
a
0

Figure 3.22: Primitive cell of Sb_2S_3. © Copyright FIZ Karlsruhe 2015

neath to rearrange into minimum energy structure. Every new cycles atoms face a Sb plane, so only S atoms can be deposited to diffuse again under the surface. On the other hand much simpler structure such as CdS which shown very well defined Cd and S planes can be easily deposited by ECALE[28] in a rather ordered structures. Another reason that could have influenced the growth process might have been the coexistence of two buffers in the deposition process. Although the exchange buffer process was optimized, it was clear that a balance had to be struck between the charge loss of S and Sb and, as a consequence of this, not a full coverage of the surface was obtained after each deposition cycle.

3.3 Deposition of other antimony chalcogenides

3.3.1 Deposition of Sb_2Te_3

The possibility of depositing Sb_2Te_3 was also taken in consideration. The first and main problem was, again, the tellurium solubility. The first attempt was to use the same buffer used for Sb in order to avoid the problems in the exchange of buffers. Nevertheless Te can not be dissolved neither in ammonia buffer nor in acetic buffer. Following the work of Gao et al.[19, 20, 21] and Flowers et al.[22] on the ECALE deposition of CdTe, an attempt of using a pH 2 solution was done. Despite of the fact that both authors are claiming to have used a tellurium oxide in a solution of 0.1 M $NaClO_4$ and 0.5 M Na_2SO_4 adjusted at pH 2 using $HClO_4$ or H_2SO_4, the presence of a white tellurium oxide precipitate was evident in both solutions.

3.3.2 Deposition of Sb_2Se_3

ECALE deposition of CdSe films on Ag(111) has been reported by Pezzatini et al.[23]. In this work Na_2SeO_3 was used in acetic buffer, at the same pH used for antimonyl tartrate during the deposition of SbS.

Se electrochemistry is rather complex as the Se UPD film can not be deposited since the formation of the Se UPD from Se(IV) is overlapping with the bulk deposition. Nevertheless after the deposition of a bulk Se film, the excess of Se can be removed by reduction of Se(0) to Se(-II) leaving a Se UPD layer on the electrode surface. In Figure 3.23 is reported (red curve) the voltammogram for Se(IV) on Ag(111) while in blue is reported another voltammogram relative to the Se stripping

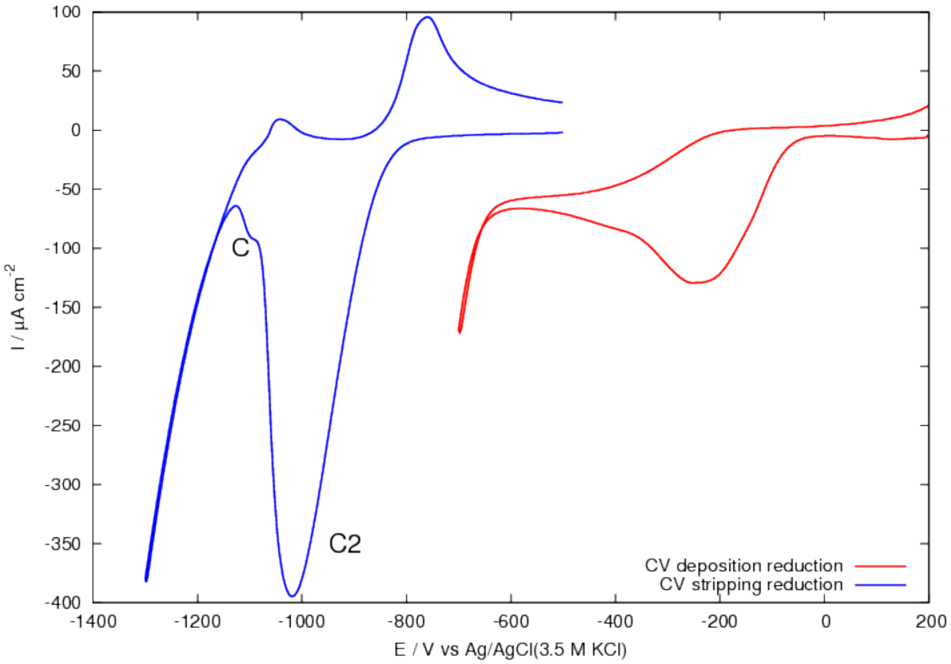

Figure 3.23: Cyclic voltammetries of 1 mM $NaSeO_3$ on Ag(111) in acetic buffer. The depositing voltammetry (red) was performed in presence of Se^{4+}ions; the stripping voltammetry (blue) was performed in the supporting electrolyte alone. Scan rate: 50 mV s^{-1}.

in acetic buffer: at potential more negative of the peak C2 is barely visible a little peak (C) which can be identified with the cathodic stripping of the Se UPD layer. In order to identify the optimal conditions for the stripping of the Se in excess some electrochemical tests were performed.

It was chosen to deposit the Se bulk film by applying -0.4 V for 30 seconds, then the reduction of the Se in excess was tested at different potentials until was possible to make the bulk Se peak disappear leaving unaltered the UPD peak. The tests are shown in Figure 3.24, where two stripping attempts are reported at -0.75 and -0.8 V. Stripping at -0.75 V leads to the removal of the majority of the bulk Se but a little shoulder (C2) on the side of the Se UPD peak is still visible. Stripping at -0.8 V instead leads to the complete disappearance of the bulk peak (green plot) leaving the charge involved with the UPD process unaltered. Other tests were also carried on using -0.775 V as stripping potential, nevertheless some bulk residue remained on the sample and eventually it was chosen to strip the Se excess at -0.8 V for 60 seconds.

In order to identify the presence of Sb UPD, several cyclic voltammetries to

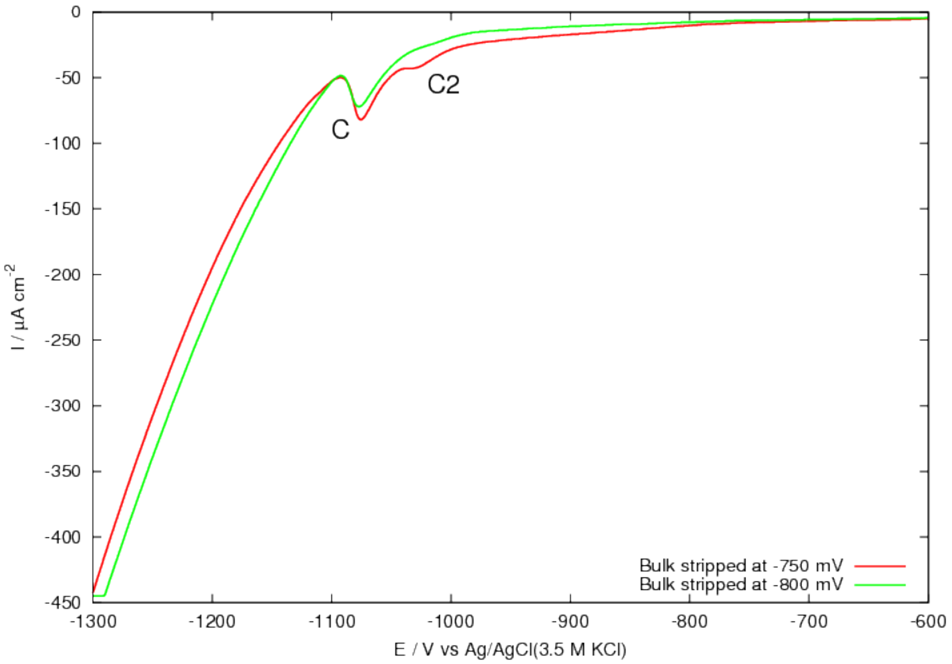

Figure 3.24: Stripping voltammetries of Se/Ag(111) in acetic buffer. The red one was performed after reductively stripping Se bulk at -0.75 V, the green one after reductively stripping Se bulk at -0.8 V. Scan rate: 50 mV s^{-1}.

increasingly negative potentials of 0.5 mM $K_2Sb_2(C_4H_2O_6)_2$ on Se/Ag(111) were performed. From the data reported in Figure 3.25 there is no hint of a anodic stripping of Sb UPD film, although close to the main reductive peak C2, seems to appear a little bump (C). In fact, further stripping tests of Sb deposited on Se/Ag(111) at potentials coherent with the bump C, did not show any anodic peak. It can be concluded that Sb can not be deposited on Se or that this process can not be split from bulk deposition.

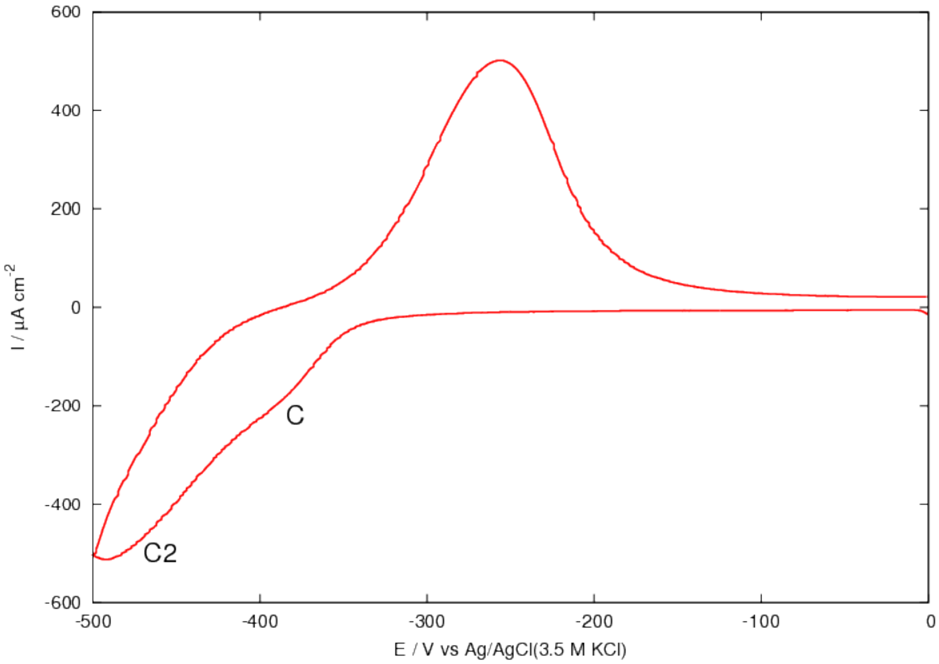

Figure 3.25: Cyclic voltammetries of 0.5 mM $K_2Sb_2(C_4H_2O_6)_2$ on Se/Ag(111) in acetic buffer. Scan rate: 50 mV s^{-1}.

3.4 Deposition of $ZnSe$

3.4.1 Electrochemical characterization

The possibility of depositing $ZnSe$ thin films on Ag(111) was investigated already in the past by Pezzatini et al.[23]. The use of Zn as cation instead of Sb makes possible the use of ammonia buffer solutions at pH 8.5 since SeO_3^{2-} and Zn^{2+} are stable at this pH. In order to avoid Ag/Zn alloy formation during Zn deposition, Se is the first element that will be deposited on the surface during the layer by layer growth. Unfortunately at pH 8.5 the cathodic peak relative to the Se UPD stripping is hidden by the hydrogen discharge. In order to establish the parameters to be used during the growth process (potential and time), the presence and the stability of the Se UPD film was checked using a 0.1 M NaOH solution. In this conditions in fact the hydrogen discharge is shifted to more negative potentials and the stripping of the Se UPD film can be observed. The test was performed depositing bulk Se(0) from a sodium selenite solution and then stripping the bulk by reduction of Se(0) to Se(-II) at -1.0 V. In this way only a monolayer of Se remains on the surface and its

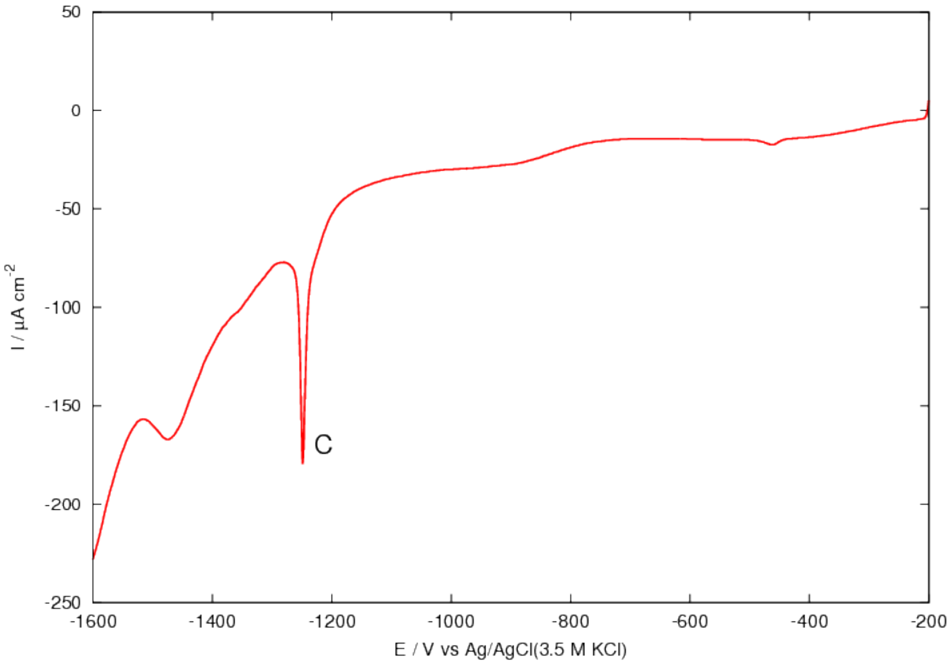

Figure 3.26: Stripping voltammetry of 1 mM $NaSeO_3$ on Ag(111) in 0.1 M NaOH. The peak indicated by C is originated by the stripping of a Se UPD monolayer. Scan rate: 50 mV s^{-1}.

reductive stripping can be measured by stripping voltammetry in 0.1 M NaOH. The results of the test are reported in Figure 3.26, where the presence of an UPD peak (C) is addressing the presence of a Se monolayer on the surface.

The ideal conditions for the deposition of a Se UPD monolayer were identified with several deposition/stripping tests. After this trial and error process it was established that the deposition of the bulk Se and the subsequent stripping processes can be safely performed at a potential of -1.0 V. These findings are in good agreement with a previous study[23] performed in similar conditions. During the deposition at such potential, Se is reduced from Se(IV) to Se(0) and subsequently to Se(-II). The Se(-II) formed during this process reacts with the Se(IV) present in solution producing more Se(0). This does not influence the final result, since the goal of this deposition step is to obtain a Se bulk film. The following step is the stripping of the excess of Se. During this step the $NaSeO_3$ solution has to be replaced with a solution containing the supporting electrolyte alone, in order to avoid the reduction of Se(IV) by Se(-II). This two deposition steps last respectively 120 and 60 seconds.

Zn UPD deposition on Se was investigated by cyclic voltammetry in a Zn^{2+}

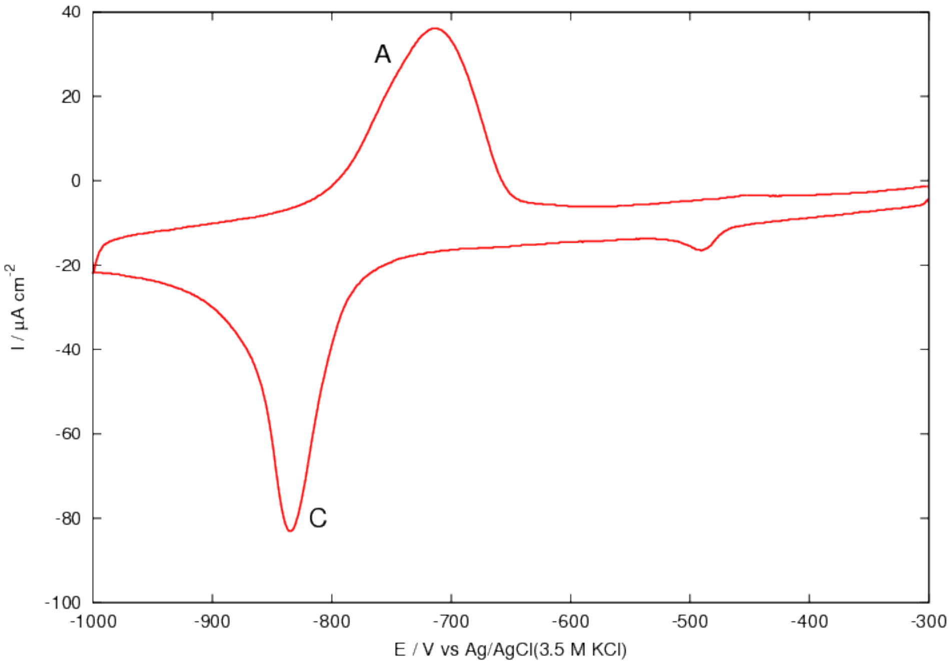

Figure 3.27: Cyclic voltammetries of $ZnSO_4$ on Se/Ag(111) in ammonia buffer. Scan rate: 50 mV s^{-1}.

solution in ammonia buffer at pH 8.5. The cathodic sweep of the scan must not exceed -1.0 V in order to avoid the stripping of the Se. In Figure 3.27 is reported a voltammetric study of Zn deposition on Se. Two UPD peaks are clearly visible (A and C), representing respectively the Zn UPD reduction (C) and oxidation (A). From this data was possible to choose -0.95 V as an optimal potential for the Zn UPD deposition during the ECALE growth.

Several growth tests were performed on multilayer films to verify the deposition conditions. In Figure 3.28 are reported the data obtained from the stripping of Se/Zn/Se and $Se/[Zn/Se]_{10}$ on Ag(111). The first element stripped was Zn, then the stripping of the Se was performed (figure 3.29). It is worth to mention that the stripping of the Se UPD layer is hidden by the hydrogen discharge and only the charge relative to the stripping of bulk Se is visible in the plot.

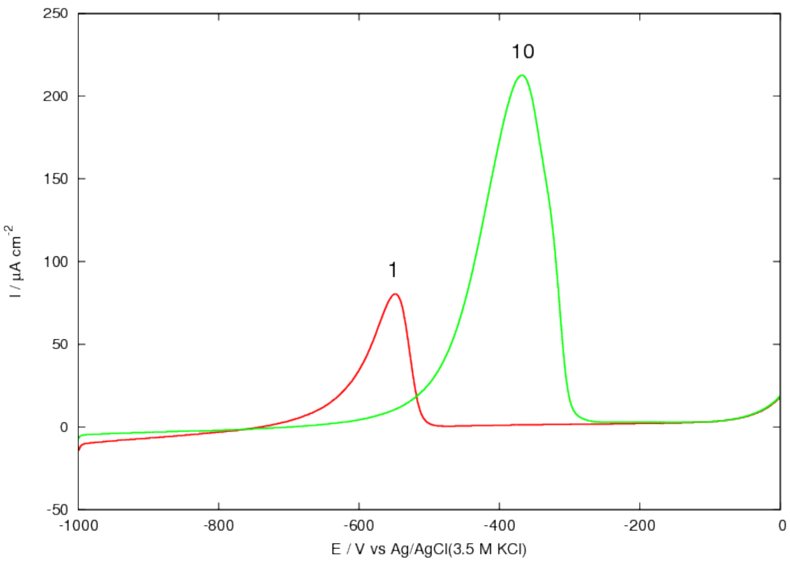

Figure 3.28: Stripping voltammetries of Zn in acetic buffer after multilayer depositions. The red curve is relative to the stripping of a Se/Zn/Se film on Ag(111), was obtained by stripping a $ZnSe$ film grown by 10 ECALE cycles ($Se/[Zn/Se]_{10}$). Scan rate: 50 mV s^{-1}.

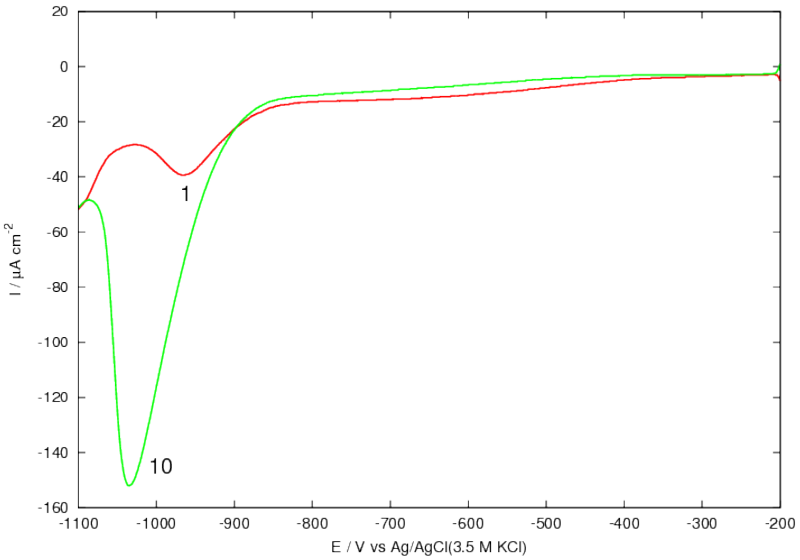

Figure 3.29: Stripping voltammetries of Se in ammonia buffer after multilayer depositions. The red curve is relative to the stripping of a Se/Zn/Se film on Ag(111), the green was obtained by stripping a $ZnSe$ film grown by 10 ECALE cycles ($Se/[Zn/Se]_{10}$). Scan rate: 50 mV s^{-1}.

3.4.2 Reflectivity experiments

X-ray reflectivity and specular reflectivity experiments were performed in order to determine the thickness and the out-of-plane crystallographic parameters of the film. The samples used in such experiments were grown by 50 Zn/Se ECALE cycles, according with the procedure described above, on Ag(111) substrates prepared by sputtering-annealing in UHV.

In Figure 3.30 is reported the extended reflectivity or specular reflectivity. The peak with very high intensity ($q_z = 2.67\text{Å}^{-1}$) correspond to the (111) reflection of the Ag substrate, while the other two at $q_z = 1.89\text{Å}^{-1}$ and $q_z = 3.63\text{Å}^{-1}$ belong to the *ZnSe* film. Two stable structures for ZnSe are reported in literature: Zincblende and Wurtzite. The two theta values for the diffraction peaks originated by the film match with the values reported for the (002) and (004) reflections of the *ZnSe* in the wurtzite structure[33]. Lattice parameters of the ZnSe along the direction perpendicular to the surface can be calculated from the q values:

$$c = \frac{2\pi}{q_{(001),ZnSe}} = 6.65\text{Å}$$

where $q_{(001),ZnSe} = {}^{q_{(002),ZnSe}}/_{2}$. This value is comparable with the one reported in literature (c=6.626Å[33]) for the wurtzite structure of *ZnSe*.
The intensity of these two reflections is much lower than the (111) reflection of the Ag substrates due to smaller scattering volume of the film and they appear to be very broad because of the finite thickness of the film. The presence of fringes around the Bragg position should be observable for such thin film (as reported for similar samples[28]), nevertheless this can be due to high surface and film roughness and structural imperfections in the deposit.

From the periodicity of the oscillation present in the reflectivity (Figure 3.31) it's possible to extract information about the film thickness (see Subsection 2.5.2). The period of the fringes is calculated to be $\triangle q_z = 0.134\text{Å}^{-1}$, therefore the total film thickness (d) is

$$d = \frac{2\pi}{\triangle q_z} = 46.89\text{Å}$$

From this data and the value of the out-of-plane lattice parameter of the film measured from the specular rod it is possible to calculate the number of times the unit cell is repeated along the perpendicular direction to the surface. Being the thickness 46.89Å and c=6.65Å, we can state that the film thickness is equivalent

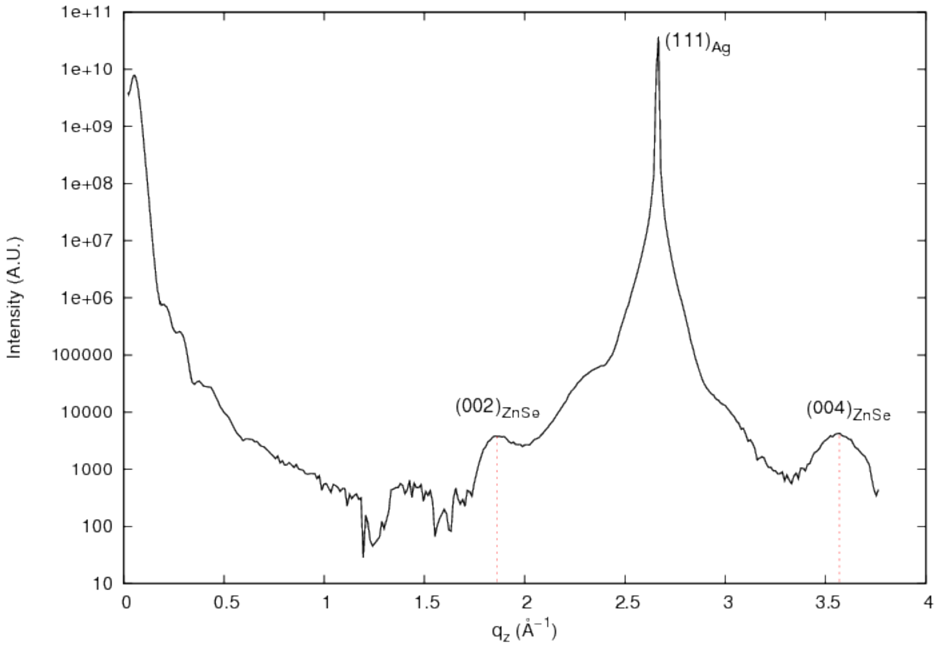

Figure 3.30: X-ray specular reflectivity.

to a stack of 7 unit cells. This number might seem surprisingly small compared to the nominal thickness of a 50 Zn/Se layers or 25 wurtzite unit cells (equivalent to 165.7Å) which have been supposedly deposited during the growth. This difference can be explained with the fact that during an ECALE cycle the deposition of the elements might lead to the formation of incomplete monolayers, as already reported elsewhere[28]. Assuming that the *ZnSe* film is deposited with a Wurtzite structure, the theoretical charge deposited for a single UPD layer is calculated to be

$$Q = \frac{2e}{A_b} = 234\,\mu C\,cm^{-2}$$

where e is the electron charge and $A_b = 13.67\text{Å}^2$ is the basis area of the unit cell. As two electrons are involved both for the reductive stripping of Se(0) to Se(-II) and for oxidative stripping of Zn(0) to Zn(II), the calculated charge is the same for both elements.

Pezzatini et al.[23] reported an average deposited charge during each ECALE cycle of $61\,\mu C\,cm^{-2}$ for Zn and $63\,\mu C\,cm^{-2}$ for Se. From the experimental data it appears clear that, for each ECALE cycle, only 0.26 monolayer of Zn and 0.27 monolayer of Se are deposited, which is consistent with the fact that the measured

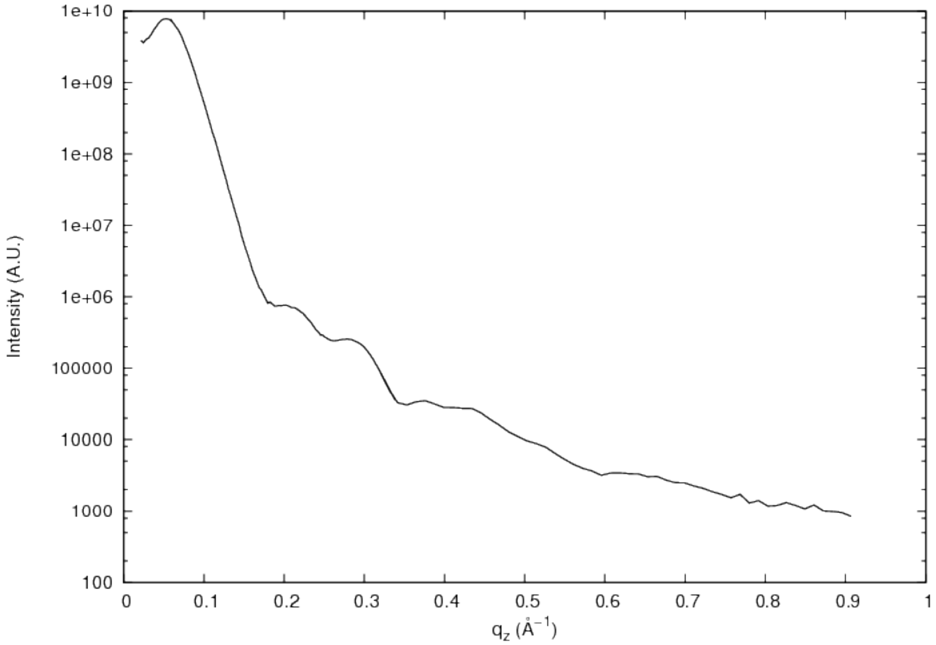

Figure 3.31: X-ray reflectivity.

thickness is 0.28 times the expected one.

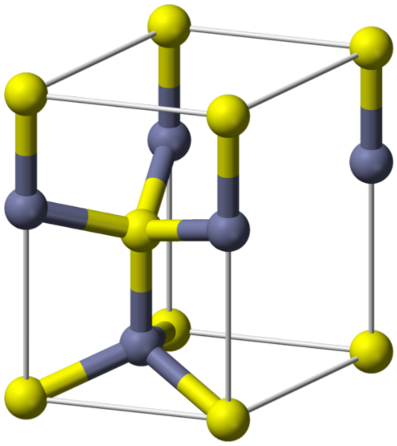

Figure 3.32: Primitive cell of *ZnSe* Wurtzite.

3.4.3 In-plane structure

Intensity maps were measured at constant l to investigate the in-plane ordering of the *ZnSe* film. The values of l were chosen on the basis of the lattice parameter

c measured in the specular reflectivity. The maps were measured at an incidence angle of 0.3 degrees for l=0, 1.16 and 2.32 according to the surface unit cell of the Ag(111), which correspond to l=0, 1 and 2 in the coordinates of the *ZnSe* film. In all the figures shown in this section the surface unit cell of Ag(111) is indicated in red.

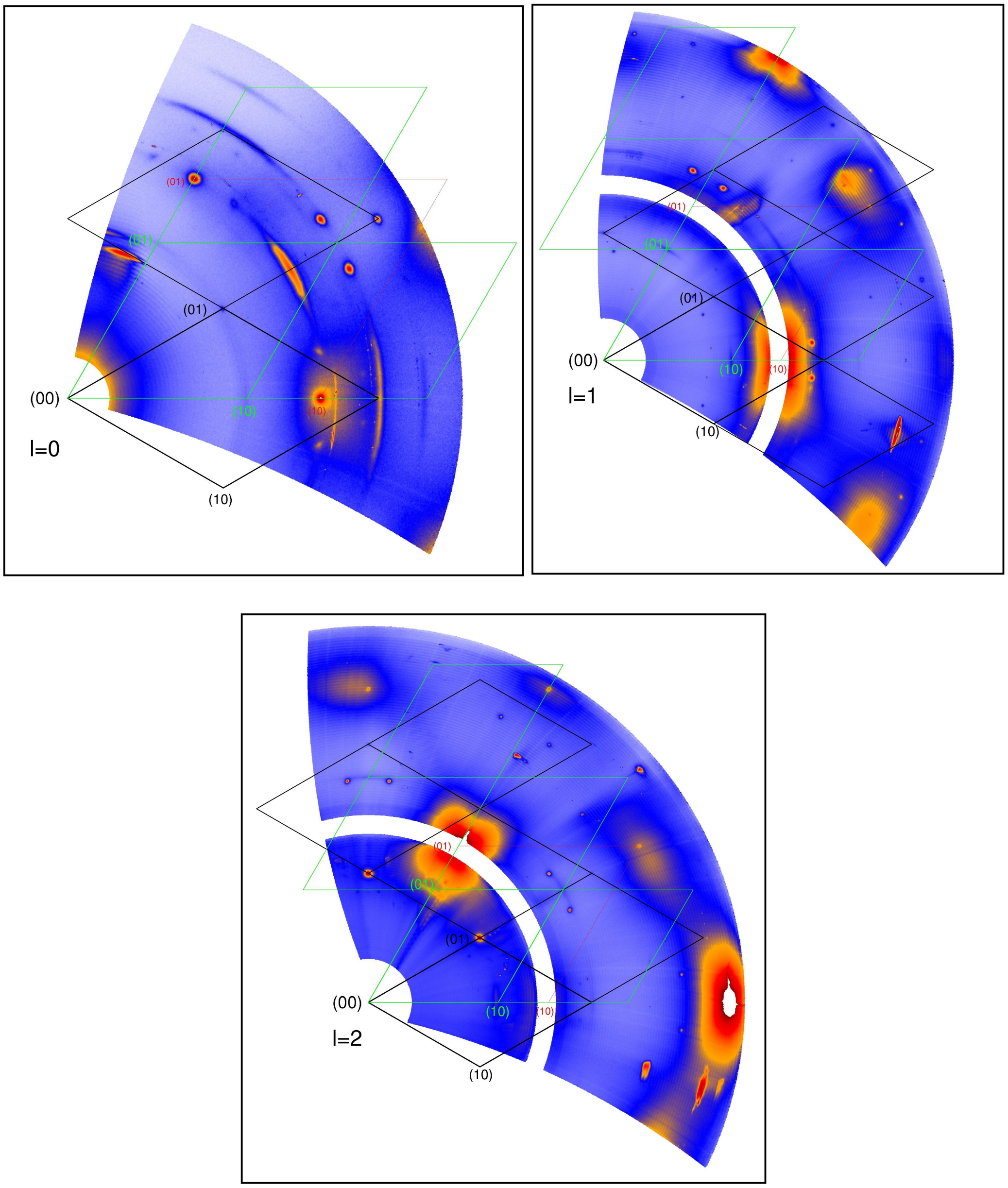

Figure 3.33: Intensity maps at l=0, l=1, l=2 (according to *ZnSe* lattice parameters). Wurtzite unit cells rotated by 30° are indicated in black and green, Ag surface unit cell is indicated in red. h and k axis are referred to the Ag surface unit cell.

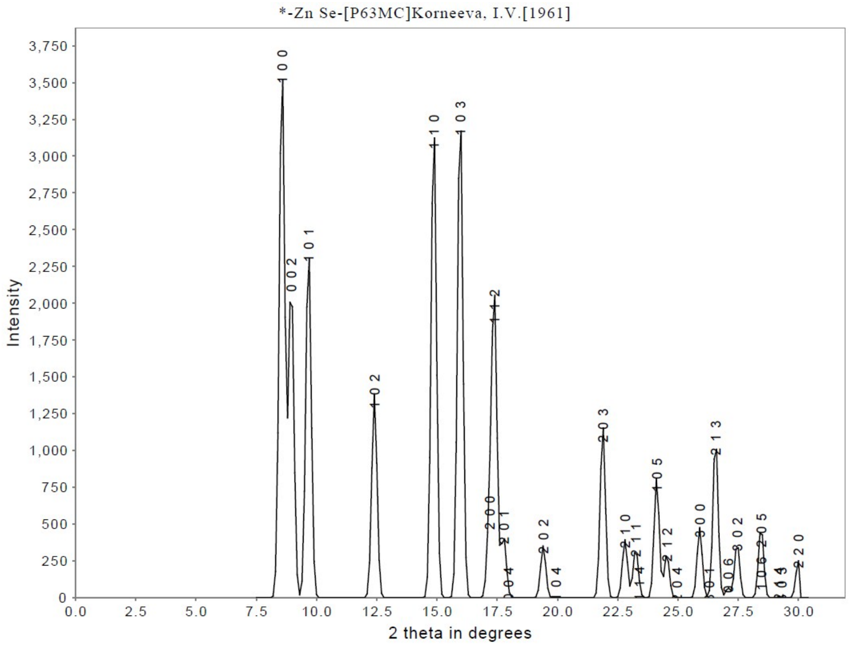

Figure 3.34: ZnSe-wurtzite powder pattern for $\lambda = 0.517$Å.

The in-plane meshes show the contemporary presence of different epitaxial structures ordered in several domains.

The first structure has been identified as *ZnSe* in Wurtzite form. In the maps reported in Figure 3.33 two orientational domains of the Wurtzite structure are indicated in green and black (same domain rotated by 30°). Bragg peaks corresponding to the *ZnSe*-Wurtzite reflections can be addressed. For maps recorded at l=0 the peaks (010), (020) and (110) can be identified referring to the hk coordinates of the black and green cells. Of course also peaks (100), (200) and ($\bar{1}$20) are present due to the lattice symmetry. At l=1 are visible the (011) ZnSe Wurtzite reflection and the less intense (021). In the maps at l=2 (012) peaks of both domains are strongly visible but also peaks (112), (122) and (132) can be identified even if their intensity is much lower. The two-theta values for the reflections listed above match with the ones reported for ZnSe in the Wurtzite form[33] (Figure 3.34). Given the position of the (00l) peaks and the peaks at l=0, it can be concluded that the film is oriented with the basal plane parallel to the Ag(111) surface. Moreover from the magnitude of unit cell vector (1.56Å^{-1}), it can be calculated the real lattice parameter $a = 4.01$Å in agreement with the value reported by Korneeva[33].

The second reported structure does not belong to the *ZnSe* Wurtzite or Zincblende structure. This lattice, reported in Figure 3.35, has a 60° symmetry and appears as two main domains rotated respectively by 25° (green) and 35° (black) relative to the *hk* axis of Ag. Two other equivalent domains with lower intensities respect to the previous ones are indicated with the red and pink lattices in the figure. These two additional domains are rotated by 15° (pink) and 45° (red) respect to the *hk* axis of Ag and can be identified by the presence of the (031) peaks while the (011) peaks are not visible due to the lower relative intensities. The lack of intensity makes also impossible to spot the (010), (012), (030) and (032) reflections while the (020), (022) and (110) are clearly visible. The in-plane lattice parameter for this structure is 4.72Å, which does not seem to match with any structure reported in literature for *ZnSe*.

A third structure, reported in Figure 3.36, was identified on the intensity maps and it does not belong to any reported *ZnSe* structure. The symmetry of the lattice is 60° and the calculated real lattice parameter is 15.02Å, resulting in a rather large unit cell. The structure can be identified by the presence of (24), (34), (43) and (42) peaks at any l value. It's worth to notice that the film lattice seems to match with the substrate lattice at integer *hk* values. For this reason it is likely to believe that these diffraction peaks might be somehow related with the presence of a silver compound at the interface. Nevertheless Ag alloying or Ag surface reconstructions were never observed on similar samples[28]. The presence of bulk Se domains or Ag/Zn alloy formation can be excluded on the basis of the electrochemical characterization of the samples which indicate a well defined stoichiometric relation in the content of Zn and Se of the film.

Unfortunately the origin of this structure is not clear and a further investigation would be needed to fully characterize it.

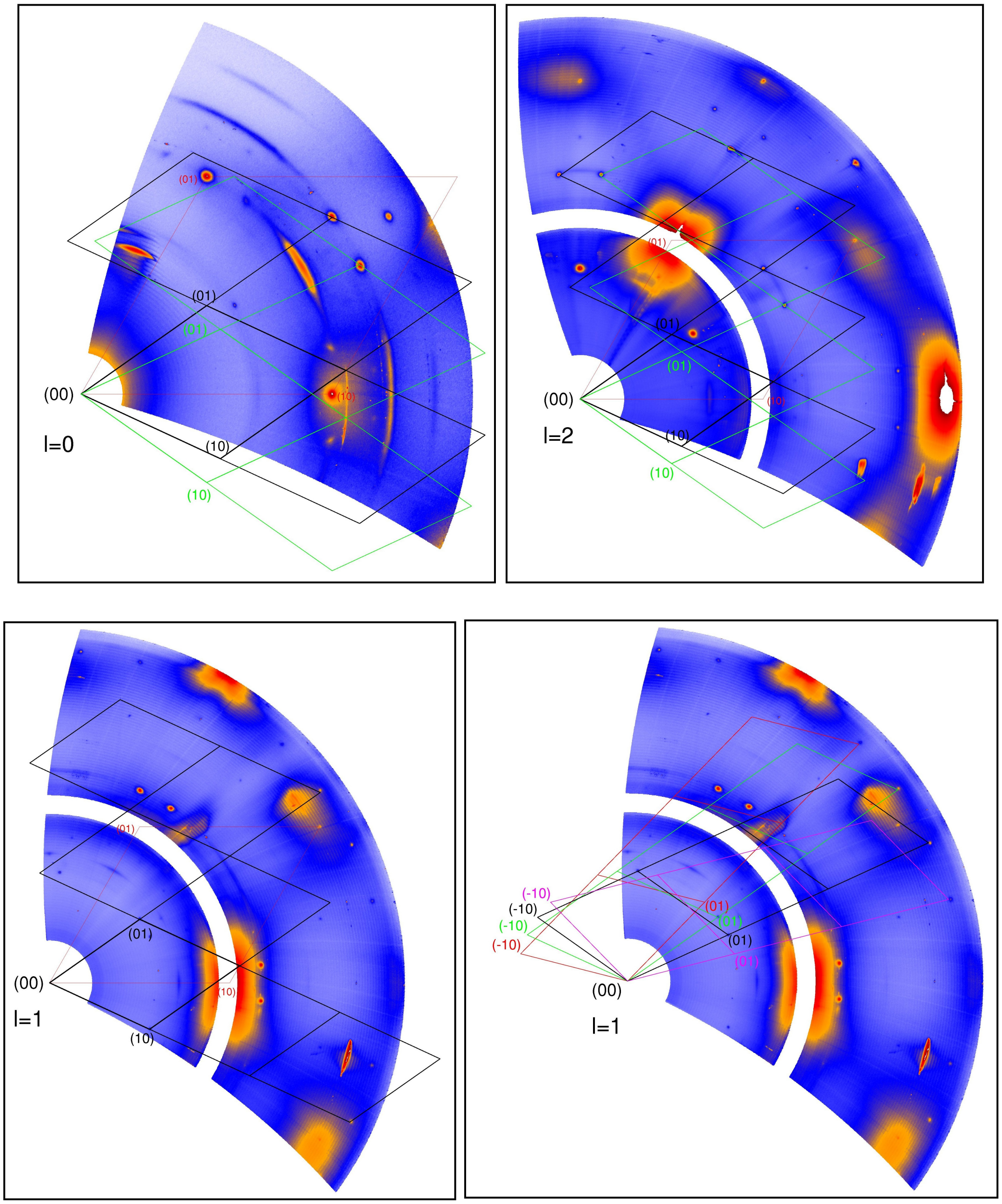

Figure 3.35: Intensity maps at l=0, l=1, l=2 (according to *ZnSe* lattice parameters). Lattice unit cells rotated by 10° are indicated in black and green; other two additional lattices are indicated in red and pink. Ag surface unit cell is indicated in red. h and k axis are referred to the Ag surface unit cell.

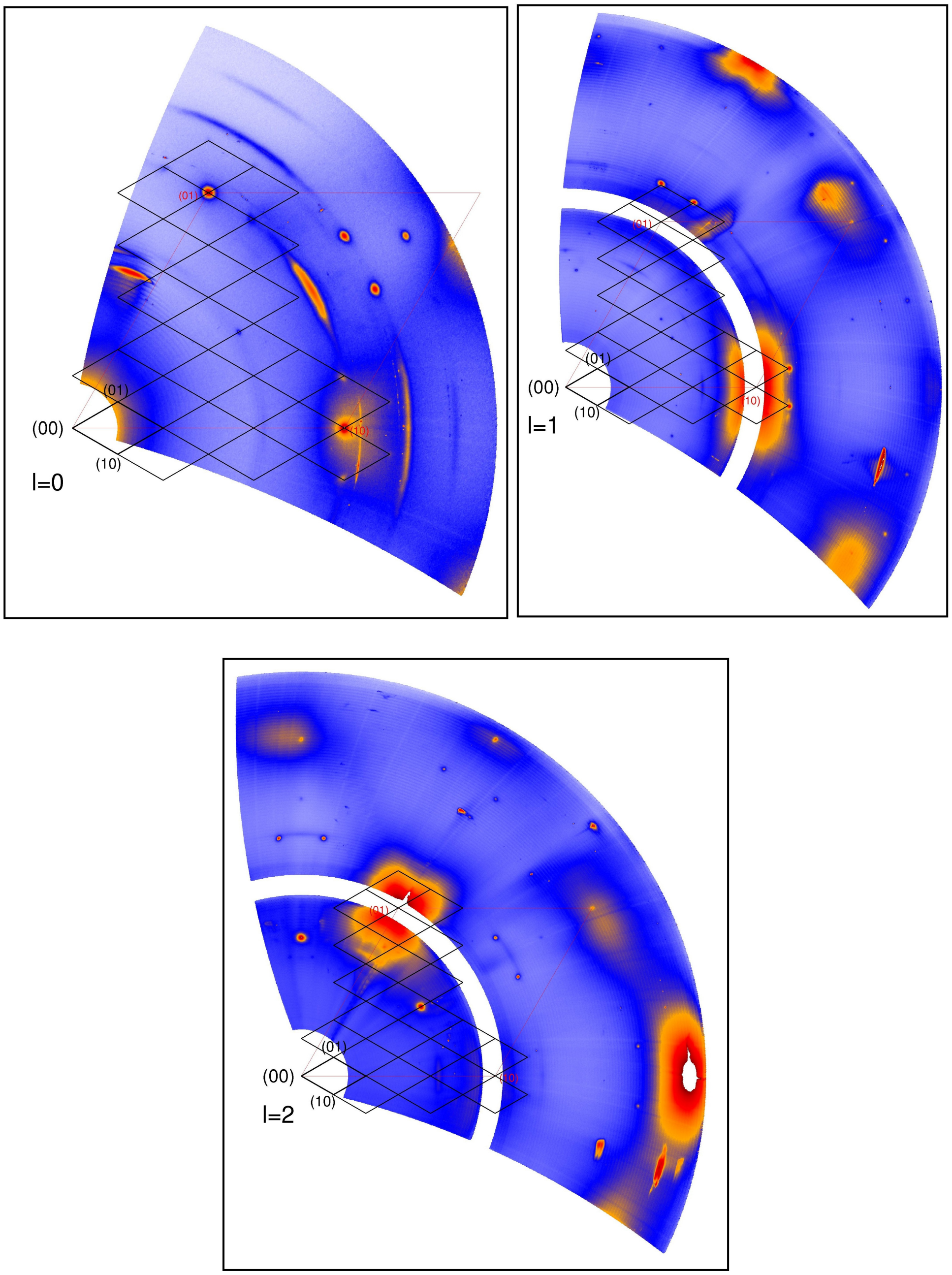

Figure 3.36: Intensity maps at l=0, l=1, l=2 (according to *ZnSe* lattice parameters). Lattice unit cell is indicated in black, Ag surface unit cell is indicated in red. h and k axis are referred to the Ag surface unit cell.

3.4.4 Microscopy Imaging

The surface of the *ZnSe* film samples was investigated by microscopic analysis in order to have a full overview on the growth result. Both Atomic Force Microscope (AFM) and Scanning Electron Microscope (SEM) were used to fully understand the superficial conformation of the deposition.

Several images were taken with both AFM and SEM, randomly observing the whole surface of the sample. It does not seem to be homogenous and flat as it could be expected, although it appears to show quite the same features around the sample.

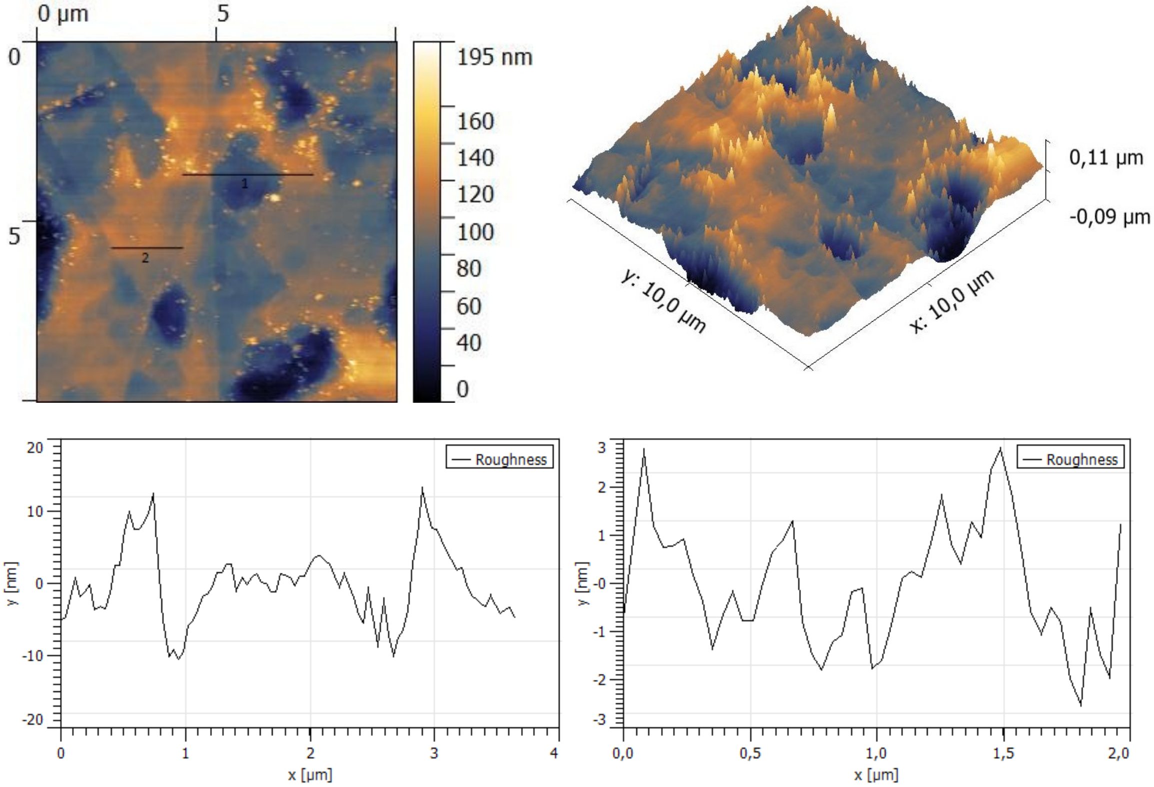

Figure 3.37: AFM image, 3D representation and roughness of the surface along drawn lines.

In Figure 3.37 is reported an AFM image of a 10×10μm region of the sample: a quite rough surface can be seen and several features appear on it. The roughness of the substrate along drawn lines is about 3-5 nanometers: in fact the higher roughness along line 1 is due to the presence of a 40-nm deep hole. This roughness value is extremely high considering that the film is measured to be only 4-nm thick. How-

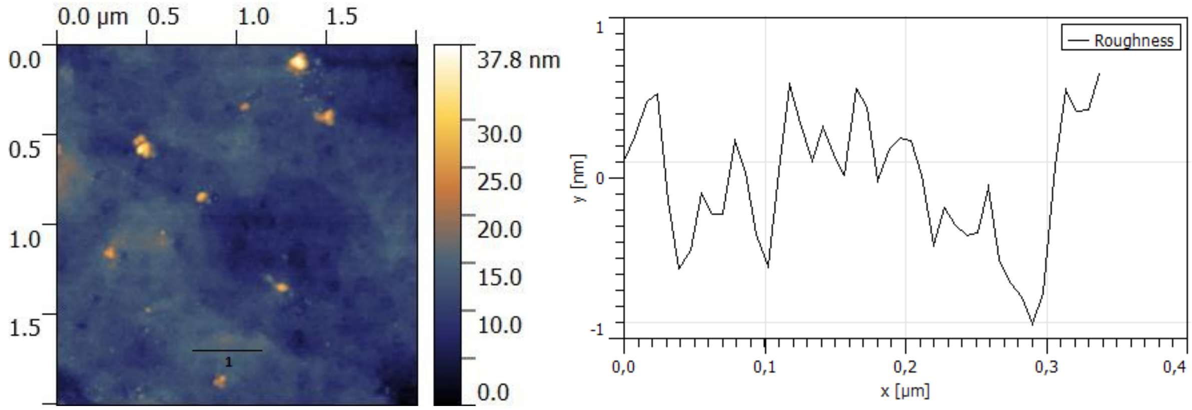
0.0 µm
0.5
1.0
1.5
0.0
0.5
1.0
1.5
1
37.8 nm
30.0
25.0
20.0
15.0
10.0
0.0
Roughness
y [nm]
1
0
-1
0,0
0,1
0,2
0,3
0,4
x [µm]

(a) 2×2µm image.

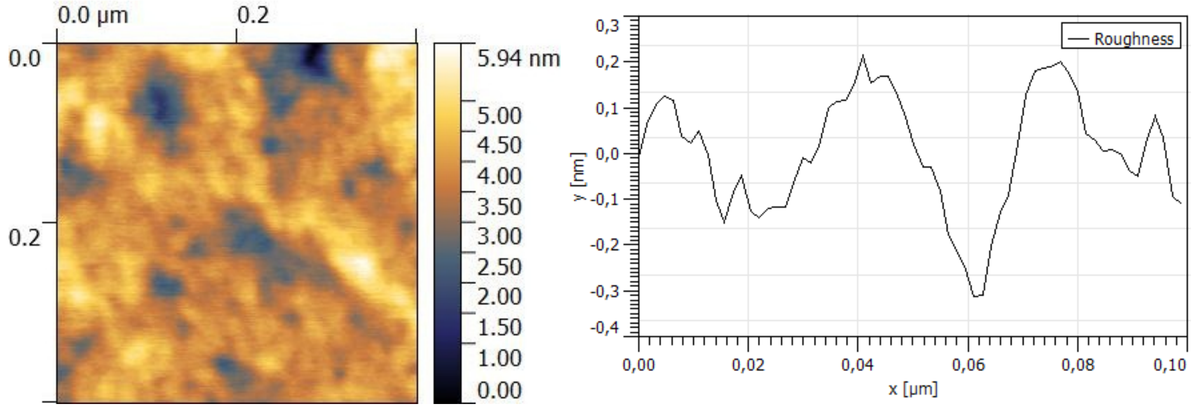
0.0 µm
0.2
0.0
0.2
5.94 nm
5.00
4.50
4.00
3.50
3.00
2.50
2.00
1.50
1.00
0.00
Roughness
y [nm]
0,3
0,2
0,1
0,0
-0,1
-0,2
-0,3
-0,4
0,00
0,02
0,04
0,06
0,08
0,10
x [µm]

(b) 0.4×0.4µm image.

Figure 3.38: AFM images and roughness of the surface along drawn lines.

ever deeper information can be deduced by Figure 3.38 showing two magnifications (2×2µm and 0.4×0.4µm) of the previous area. It can be seen that roughness values are considerably lower reaching some angstrom in the smaller scan. Therefore, the actual roughness of the sample is in the order of angstrom, which agrees with the expected Frank-van der Merwe growth mode, typical of the ECALE method. Nevertheless it can not be forgotten that deep holes and high clusters are present on the surface. Since the film is only 4-nm thick these features has to be addressed to the substrate even though it should be completely flat.

This superficial conformation is recognizable also from SEM images. In Figure 3.39a a roughness comparable to the one from AFM images can be detected and clusters are clearly visible on the surface. On the other hand in Figure 3.39b there is no clump presence but a hills and holes layout seems to appear.

From this microscopic analysis it is clear that the surface is highly heterogeneous and it contrasts with the expected result. Nevertheless it has to be pointed out that this imaging was performed on samples after their x-rays exposure, therefore it is likely that structural measurements damaged the surface of the grown film.

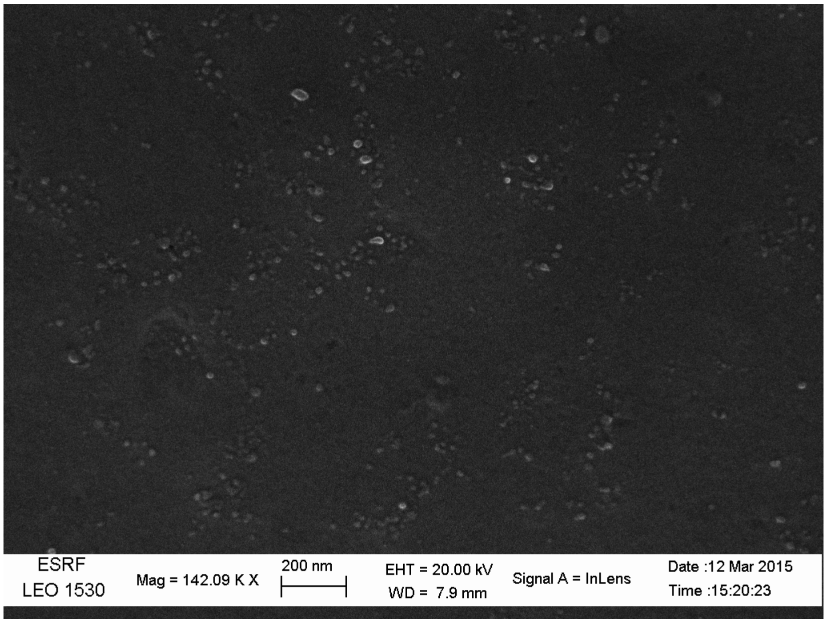
ESRF
LEO 1530
Mag = 142.09 K X
200 nm
EHT = 20.00 kV
WD = 7.9 mm
Signal A = InLens
Date :12 Mar 2015
Time :15:20:23

(a) Magnification 142.09 K ×; voltage level 20 kV.

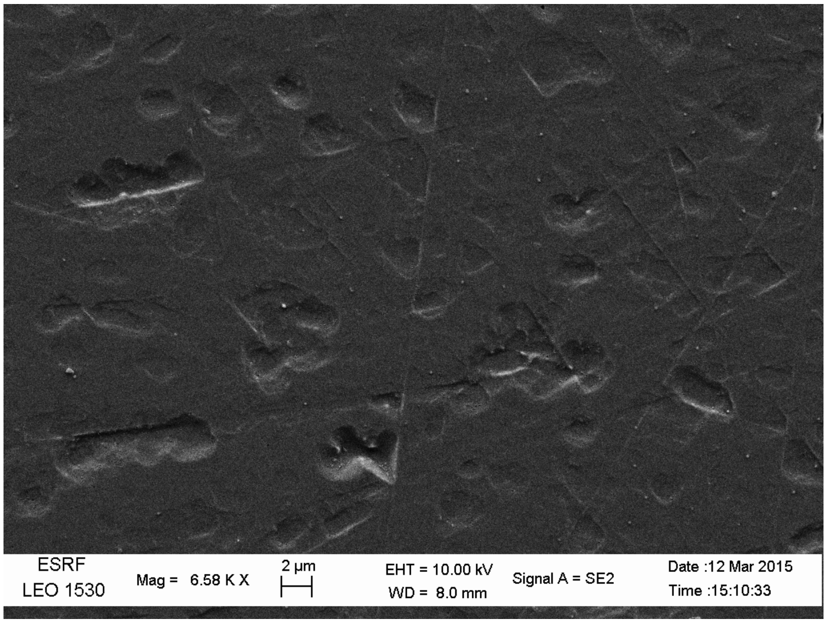
ESRF
LEO 1530
Mag = 6.58 K X
2 µm
EHT = 10.00 kV
WD = 8.0 mm
Signal A = SE2
Date :12 Mar 2015
Time :15:10:33

(b) Magnification 6.58 K ×; voltage level 10 kV.

Figure 3.39: SEM images at different magnifications.

Chapter 4

Conclusions

During this thesis an extensive study of the layer by layer growth process of antimony chalcogenides on silver single crystals has been carried on. Large part of the work was devoted to the investigation of Sb_2S_3 deposition in different buffers. The experimental work leaded to the conclusion that the literature on this topic is either inaccurate or reports misleading results. As a matter of facts the data reported by Stickney et al.[4] seems to be not reproducible or inconsistent with our results. In order to overcome solubility issues, related with the chemistry of Sb in basic media, new strategies for UPD deposition of Sb from potassium antimonyl tartrate solution in acidic media have been developed. Eventually the electrochemical growth of Sb_2S_3 was carried out optimizing deposition potentials for each monolayer so as to assure the correct Sb-S alternance. In order to achieve this result, the overall procedure was refined identifying precise potentials for each deposition step. In fact, confirming a general trend for Sb chalcogenides already observed in the past[19, 27], it can be useful to slightly change potentials of each cycle in order to achieve the same charge deposition for all ECALE layers. Nevertheless it appeared that the growth of Sb_2S_3 is inhibited after the deposition of two monolayers of the elements forming the compound. This result can be addressed to the complex structure of Sb_2S_3 unit cell, not allowing a layer by layer growth. A further analysis on antimony chalcogenide could be carried out in future to fully understand the behavior of Sb and S deposition after the critical second ECALE cycle.

The main part of this project was then dedicated to the characterization of $ZnSe$ thin films. Se and Zn deposition parameters reported by Pezzatini et al.[23] were optimized in order to achieve reliable growth conditions. The Se layer was obtained depositing an excess of Se and then reductively stripping the bulk, Zn underpotential deposition was then performed on Se layer. According to this strategy thin films of *ZnSe* up to 50 cycles were successfully deposited via ECALE on Ag(111).

A structural x-ray investigation was carried out on the *ZnSe* film to identify its crystallographic structure and obtain information on its structural properties. Specular reflectivity experiments clearly show that the film is ordered along direction perpendicular to the surface of the substrate. The two theta values for the out-of-plane reflections of the film were found to be in good agreement with the values reported in literature[33] for the (002) and (004) reflections of the *ZnSe* in the Wurtzite form. In this sense the hexagonal structure of *ZnSe* seems to be oriented with the basal plane parallel to the Ag(111) surface. The thickness of the film calculated from the x-ray reflectivity data is in good agreement with the theoretical thickness calculated on the basis of the structural data and the electrochemical analysis on the charge deposited.

The presence of a Wurtzite structure has been confirmed by further analysis with grazing incidence x-ray diffraction. Two domains of *ZnSe* in the Wurtzite form rotated by 30° have been identified in the intensity maps recorded at constant l. Moreover, the presence of other *ZnSe* structures on Ag(111) was identified. This appears to be an extremely stimulating finding as none of these structures could be reconducted to any known structure of *ZnSe* reported in the literature. Unfortunately in order to identify the exact order and composition of this phases a deeper structural investigation, which is well beyond the purpose of this thesis, should be carried out.

Bibliography

[1] Prikhodchenko P. V.; Gun J.; Sladkevich S.; Mikhaylov A. A.; Lev O.; Tay Y. Y.; Batabyal S. K.; Yu D. Y. W. Chem. Mater. 2012, 24, 4750−4757.

[2] Yu D. Y.W.; Prikhodchenko P. V.; Mason C. W.; Batabyal S. K.; Gun J.; Sladkevich S.; Medvedev A. G.; Lev O.; Nature Communications, 4:2922

[3] Yu D. Y. W.; Hoster H. E.; Batabyal S. K.; Sci Rep. 2014 Apr 2; 4:4562

[4] Liang X.; Jayaraju N.; Thambidurai C.; Zhang Q.; Stickney J. L.; Chem. Mater. 2011, 23, 1742–1752.

[5] Atkins P.; de Paula J.; Physical Chemistry 2006, Eighth Edition, W. H. Freeman and Company.

[6] Ashcroft N. W.; Mermin N. D.; Solid State Physics 1976, Brooks/Cole CENGAGE Learning.

[7] Luth H.; Solid Surfaces, Interfaces and Thin Films 2010, Fifth Edition, Springer.

[8] Schreiber F.; Gerlach A.; X-Ray and Neutron Reflectivity for the Investigation of Thin Films.

[9] Stickney J. L.; The Electrochemical Society, Interface Summer 2011, 28-30.

[10] Gregory B. W.; Stickney J. L.; J. Electroanal. Chem., 300 (1991) 543-561.

[11] Aloisi G. D.; Cavallini M.; Innocenti M.; Foresti M. L.; Pezzatini G.; Guidelli R.; J. Phys. Chem. B 1997, 101, 4774-4780.

[12] Hatchett D. W.; White H. S.; J. Phys. Chem. 1996, 100, 9854−9859.

[13] Hatchett D. W.; Gao X.; Catron S. W.; White H. S.; J. Phys. Chem. 1996, 100, 331−338.

[14] Gayer K. H.; Garrett A. B.; Journal of the American Chemical Society, Vol. 74 1952, 2353-2354.

[15] Schuhmann R.; Journal of the American Chemical Society, Vol. XLVI, No. 1, January 1924, 52-58.

[16] Casas J. M.; Crisostomo G.; Cifuentes L.; The Canadian Journal of Chemical Engineering, Vol.82, No. 1, February 1924, 175-183.

[17] Fernandes V. C.; Salvietti E.; Loglio F.; Lastraioli E.; Innocenti M.; Mascaro L. H.; Foresti M. L.; J Appl Electrochem (2009) 39:2191–2197

[18] Fernandez A.M.; Merino M.G.; Thin Solid Films 366 (2000) 202-206

[19] Gao X.; Yang J.; Zhu W.; Hou J.; Bao S.; Fan X.; Duan X.; Science in China Series E: Technological Sciences 2006, Vol. 49, No. 6, 685-692.

[20] Yang J.; Zhu W.; Gao X.; Bao S.; Fan X.; Duan X.; Hou J.; J. Phys. Chem. B 2006, 110, 4599-4604.

[21] Yang J.; Zhu W.; Gao X.; Fan X.; Bao S.; Duan X. J.; Electrochimica Acta 52 2007, 3035-3039.

[22] Flowers B. H.; Wade T. L.; Garvey J. W.; Lay M.; Happek U.; Stickney J. L.; Journal of Electroanalitical Chemistry 524-525 2002, 273-285.

[23] Pezzatini G.; Caporali S.; Innocenti M.; Foresti M. L.; Journal of Electroanalitical Chemistry 475 1999, 164-170.

[24] Loglio F.; Innocenti M.; D'Acapito F.; Felici R.; Pezzatini G.; Salvietti E.; Foresti M. L.; Journal of Electroanalytical Chemistry 575 (2005) 161–167.

[25] Loglio F.; Innocenti M.; Pezzatini G.; Foresti M. L.; Journal of Electroanalytical Chemistry 562 (2004) 117–125.

[26] Forni F.; Innocenti M.; Pezzatini G.; Foresti M. L.; Electrochimica Acta 45 (2000) 3225–3231.

[27] Mathe M. K.; Cox S. M.; Flowers B. H.; Vaidyanathan R.; Pham L.; Srisook N.; Happek U.; Stickney J. L.; Journal of Crystal Growth 271 (2004) 55–64.

[28] Carlà F.; Loglio L.; Resta A.; Felici R.; Lastraioli E.; Innocenti M.; Foresti M. L.; J. Phys. Chem. C 2014, 118, 6132-6139.

[29] Kolb D. M.; Advances in Electrochemistry and Electrochemical Engineering ed. H. Gerischer and C. W. Tobias, Wiley (NY) 1978, 125-271.

[30] Foresti M. L.; Capolupo F.; Innocenti M.; Loglio F.; Crystal Growth and Design; 2002, 2, 73-77.

[31] Hamelin A.; Advances in Electrochemistry and Electrochemical Engineering, Plenum Press (NY) 1985.

[32] Kurasawa T.; Patent Japan 35:5619, 1960.

[33] Korneeva I. V.; Kristallografiya (1961) 6, p630-p631